Topological insulators and superconductors

Xiao-Liang Qi

Microsoft Research, Station Q, Elings Hall, University of California, Santa Barbara, California 93106, USA and Department of Physics, Stanford University, Stanford, California 94305, USA

Shou-Cheng Zhang

Department of Physics, Stanford University, Stanford, California 94305, USA

(Received 2 August 2010; published 14 October 2011)

Topological insulators are new states of quantum matter which cannot be adiabatically connected to conventional insulators and semiconductors. They are characterized by a full insulating gap in the bulk and gapless edge or surface states which are protected by time-reversal symmetry. These topological materials have been theoretically predicted and experimentally observed in a variety of systems, including HgTe quantum wells, BiSb alloys, and Bi_2Te_3 and Bi_2Se_3 crystals. Theoretical models, materials properties, and experimental results on two-dimensional and three-dimensional topological insulators are reviewed, and both the topological band theory and the topological field theory are discussed. Topological superconductors have a full pairing gap in the bulk and gapless surface states consisting of Majorana fermions. The theory of topological superconductors is reviewed, in close analogy to the theory of topological insulators.

DOI: 10.1103/RevModPhys.83.1057 PACS numbers: 73.20.−r, 73.43.−f, 85.75.−d, 74.90.+n

CONTENTS

I. INTRODUCTION

Ever since the Greeks invented the concept of the atom, fundamental science has focused on finding ever smaller building blocks of matter. In the 19th century, the discovery of elements defined the golden age of chemistry. Throughout most of the 20th century, fundamental science was dominated by the search for elementary particles. In condensed matter physics, there are no new building blocks of matter to be discovered: one is dealing with the same atoms and electrons as those discovered centuries ago. Rather, one is interested in how these basic building blocks are put together to form new states of matter. Electrons and atoms in the quantum world can form many different states of matter: for example, they can form crystalline solids, magnets, and superconductors. The greatest triumph of condensed matter physics in the last century is the classification of these quantum states by the principle of spontaneous symmetry breaking (Anderson, 1997). For example, a crystalline solid breaks translation symmetry, even though the interaction among its atomic building blocks is translationally invariant. A magnet breaks rotation symmetry, even though the fundamental interactions are isotropic. A superconductor breaks the more subtle gauge symmetry, leading to novel phenomena such as flux quantization and Josephson effects. The pattern of symmetry breaking leads to a unique order parameter, which assumes a nonvanishing expectation value only in the ordered state, and a general effective field theory can be formulated based on the order parameter. The effective field theory, generally called Landau-Ginzburg theory (Landau and Lifshitz, 1980), is determined by general properties such as dimensionality and symmetry of the order parameter and gives a universal description of quantum states of matter.

In 1980, a new quantum state was discovered which does not fit into this simple paradigm (von Klitzing *et al.*, 1980). In the quantum Hall (QH) state, the bulk of the two-dimensional (2D) sample is insulating, and the electric current is carried only along the edge of the sample. The flow of this unidirectional current avoids dissipation and gives rise to a quantized Hall effect. The QH state provided the first example of a quantum state which is topologically distinct from all states of matter known before. The precise quantization of the Hall conductance is explained by the fact that it is a topological invariant, which can only take integer values in units of e^2/h, independent of material details (Laughlin, 1981; Thouless *et al.*, 1982). Mathematicians have introduced the concept of topological invariance to classify different geometrical objects into broad classes. For example, 2D surfaces are classified by the number of holes in them, or genus. The surface of a perfect sphere is topologically equivalent to the surface of an ellipsoid, since these two surfaces can be smoothly deformed into each other without creating any holes. Similarly, a coffee cup is topologically equivalent to a donut, since both of them contain a single hole. In mathematics, topological classification discards small details and focuses on the fundamental distinction of shapes. In physics, precisely quantized physical quantities such as the Hall conductance also have a topological origin and remain unchanged by small changes in the sample.

It is obvious that the link between physics and topology should be more general than the specific case of QH states. The key concept is that of a "smooth deformation." In mathematics, one considers smooth deformations of shapes without the violent action of creating a hole in the deformation process. The operation of smooth deformation groups shapes into topological equivalence classes. In physics, one can consider general Hamiltonians of many-particle systems with an energy gap separating the ground state from the excited states. In this case, one can define a smooth deformation as a change in the Hamiltonian which does not close the bulk gap. This topological concept can be applied to both insulators and superconductors with a full energy gap, which are the focus of this review article. It cannot be applied to gapless states such as metals, doped semiconductors, or nodal superconductors. According to this general definition, one gapped state cannot be deformed to another gapped state in a different topological class unless a quantum phase transition occurs where the system becomes gapless. In a large class of topological states including QH states, there are also robust gapless edge states on the spatial boundary with vacuum.

From these simple arguments, we immediately see that the abstract concept of topological classification can be applied to a condensed matter system with an energy gap, where the notion of a smooth deformation can be defined (Zhang, 2008). Further progress can be made through the concepts of topological order parameter and topological field theory (TFT), which are powerful tools describing topological states of quantum matter. Mathematicians have expressed the intuitive concept of genus in terms of an integral, called topological invariant, over the local curvature of the surface (Nakahara, 1990). Whereas the integrand depends on details of the surface geometry, the value of the integral is independent of such details and depends only on the global topology. In physics, topologically quantized physical quantities can be similarly expressed as invariant integrals over the frequency momentum space (Thouless *et al.*, 1982; Thouless, 1998). Such quantities can serve as a topological order parameter which uniquely determines the nature of the quantum state. Furthermore, the long-wavelength and low-energy physics can be completely described by a TFT, leading to powerful predictions of experimentally measurable topological effects (Zhang, 1992). Topological order parameters and TFTs for topological quantum states play the role of conventional symmetry-breaking order parameters and effective field theories for broken-symmetry states.

The QH states belong to a topological class which explicitly breaks time-reversal (TR) symmetry, for example, by the presence of a magnetic field. In recent years, a new topological class of materials has been theoretically predicted and experimentally observed (König *et al.*, 2008; Moore, 2010; Hasan and Kane, 2010; Qi and Zhang, 2010). These new quantum states belong to a class which is invariant under TR, and where spin-orbit coupling (SOC) plays an essential role. Some important concepts were developed in earlier works

(Haldane, 1988; Zhang and Hu, 2001; Murakami *et al.*, 2003; Murakami *et al.*, 2004; Sinova *et al.*, 2004), culminating in the proposal of the 2D topological insulator or the quantum spin Hall (QSH) state by Kane and Mele (2005a) and by Bernevig and Zhang (2006). Theoretical concepts developed in these works were soon generalized to the 3D topological insulators (Fu and Kane, 2007; Fu *et al.*, 2007; Moore and Balents, 2007; Qi, Hughes, and Zhang, 2008b; Roy, 2009b). All TR invariant insulators in nature (without ground-state degeneracy) fall into two distinct classes, classified by a $\mathbb{Z}_2$ topological order parameter. The topologically nontrivial state has a full insulating gap in the bulk, but has gapless edge or surface states consisting of an odd number of Dirac fermions. The topological property manifests itself more dramatically when TR symmetry is preserved in the bulk but broken on the surface, in which case the material is fully insulating both inside the bulk and on the surface. In this case, Maxwell's laws of electrodynamics are dramatically altered by a topological term with a precisely quantized coefficient, similar to the case of the QH effect.

The 2D topological insulator material, synonymously called the QSH insulator, was first theoretically predicted in 2006 (Bernevig, Hughes, and Zhang, 2006) and experimentally observed (König *et al.*, 2007; Roth *et al.*, 2009) in HgTe/CdTe quantum wells (QWs). A topologically trivial insulator state is realized when the thickness of the QW is less than a critical value, and the topologically nontrivial state is obtained when that thickness exceeds the critical value. In the topologically nontrivial state, there is a pair of edge states with opposite spins propagating in opposite directions. The 2D topological insulator is synonymously called the quantum spin Hall (QSH) insulator since its edge states carry unidirectional spin current. Four-terminal measurements (König *et al.*, 2007) showed that the longitudinal conductance in the QSH regime is quantized to $2e^2/h$, independently of the width of the sample. Subsequent nonlocal transport measurements (Roth *et al.*, 2009) confirmed the edge state transport as predicted by theory. The first discovery of the QSH topological insulator in HgTe was ranked by *Science Magazine* as one of the top ten breakthroughs among all sciences in year 2007, and the subject quickly became mainstream in condensed matter physics (Day, 2008). The 3D topological insulator was predicted in the $Bi_{1-x}Sb_x$ alloy within a certain range of compositions x (Fu and Kane, 2007), and angle-resolved photoemission spectroscopy (ARPES) measurements soon observed an odd number of topologically nontrivial surface states (Hsieh *et al.*, 2008). Simpler versions of the 3D topological insulator were theoretically predicted in Bi_2Te_3, Sb_2Te_3 (H. Zhang *et al.*, 2009) and Bi_2Se_3 (Xia *et al.*, 2009; H. Zhang *et al.*, 2009) compounds with a large bulk gap and a gapless surface state consisting of a single Dirac cone. ARPES experiments indeed observed the linear dispersion relation of these surface states (Chen *et al.*, 2009; Xia *et al.*, 2009). These pioneering theoretical and experimental works opened up the exciting field of topological insulators, and the field is now expanding at a rapid pace (König *et al.*, 2008; Kane, 2008; Zhang, 2008; Moore, 2010; Hasan and Kane, 2010; Qi and Zhang, 2010). Beyond the topological materials mentioned, more than 50 new compounds have been predicted to be topological insulators (Chadov *et al.*, 2010; Franz, 2010; Yan *et al.*, 2010; Lin, Wray *et al.*, 2010), and two of them have been experimentally observed recently (Chen *et al.*, 2010b; Sato, Segawa *et al.*, 2010). This collective body of work establishes beyond any reasonable doubt the ubiquitous existence in nature of this new topological state of quantum matter. It is remarkable that such topological effects can be realized in common materials, previously used for infrared detection or thermoelectric applications, without requiring extreme conditions such as high magnetic fields or low temperatures. The discovery of topological insulators has undoubtedly had a dramatic impact on the field of condensed matter physics.

After reviewing the history of the theoretical prediction and the experimental observation of the topological materials in nature, we now turn to the history of the conceptual developments, and retrace the intertwined paths taken by theorists. An important step was taken in 1988 by Haldane (1988), who borrowed the concept of the parity anomaly (Semenoff, 1984; Redlich, 1984a) in quantum electrodynamics to construct a theoretical model of the QH state on the 2D honeycomb lattice. This model does not require an external magnetic field nor the associated orbital quantization and Landau levels (LLs). Around the same time, Volovik (1988a) showed that helium-3A film displayed a topological structure without any orbital Landau levels. However, Haldane's model is in the same topological class as the ordinary QH states and requires both two dimensionality and the breaking of the TR symmetry. There was a misconception at the time that topological quantum states could exist only under these conditions. Another important step was the construction in 1989 of a TFT of the QH effect based on the Chern-Simons (CS) term (Zhang, 1992). This theory captures the most important topological aspects of the QH effect in a single and unified effective field theory. At this point, the path toward generalizing the QH states became clear: Since the CS term can exist in all even spatial dimensions, the topological physics of the QH states can be generalized to such dimensions. However, it was unclear at the time what kind of microscopic interactions could be responsible for these topological states. In 2001 Zhang and Hu (2001) explicitly constructed a microscopic model for the generalization of the QH state in 4D. A crucial ingredient of this model is its invariance under TR symmetry, in sharp contrast to the QH state in 2D which explicitly breaks TR symmetry. This fact can also be seen directly from the CS effective action in $4+1$ spacetime dimensions, which is invariant under TR symmetry. With this generalization of the QH state, two basic obstacles, the breaking of TR symmetry and the restriction to 2D, were removed. Partly because of the mathematical complexity involved in this work, it was not appreciated by the general community at the time, but is clear now, that this state is the root state from which all TR invariant topological insulators in 3D and 2D are derived (Qi, Hughes, and Zhang, 2008b). TR invariant topological insulators can be classified in the form of a family tree, where the 4D state is the ''grandfather'' state and begets exactly two generations of descendants, the 3D and 2D topological insulators, by the procedure of dimensional reduction (Schnyder *et al.*, 2008; Qi, Hughes, and Zhang, 2008b; Kitaev, 2009; Ryu, Schnyder *et al.*, 2010).

Motivated by the construction of a TR invariant topological state, theorists started to look for a physical realization of this new topological class and discovered the intrinsic spin Hall effect (Murakami *et al.*, 2003; 2004; Sinova *et al.*, 2004). Murakami *et al.* (2003) stated their motivation clearly in the Introduction: "Recently, the QH effect has been generalized to four spatial dimensions [...]. The QH response in that system is physically realized through the SOC in a TR symmetric system." It was realized in 2004 that the two key ideas, TR symmetry and SOC, can also be applied to insulators as well, leading to the concept of spin Hall insulator (Murakami *et al.*, 2004). The spin Hall effect in insulators is dissipationless, similar to the QH effect. The concept of spin Hall insulator motivated Kane and Mele (2005a) to investigate the QSH effect in graphene, a material first discovered experimentally that same year. Working independently, Bernevig and Zhang studied the QSH effect in strained semiconductors, where SOC generates LLs without the breaking of TR symmetry (Bernevig and Zhang, 2006). Unfortunately the energy gap in graphene caused by the intrinsic SOC is insignificantly small (Min *et al.*, 2006; Yao *et al.*, 2007). Even though neither models have been experimentally realized, they played important roles for the conceptual developments. Bernevig, Hughes, and Zhang (2006) successfully predicted the first topological insulator to be realized in HgTe/CdTe QWs.

The QSH state in 2D can be roughly understood as two copies of the QH state, where states with opposite spin counterpropagate at the edge as is illustrated in Fig. 1. A natural question arises as to whether the edge states of the QSH state are stable. Kane and Mele (2005b) showed that the stability depends on the number of pairs of edge states. An odd number of pairs is stable, whereas an even number of pairs is not. This observation led Kane and Mele to propose a $\mathbb{Z}_2$ classification of TR invariant 2D insulators. In addition, they devised a precise algorithm for the computation of a $\mathbb{Z}_2$ topological invariant within the topological band theory (TBT). TBT was soon extended to 3D by Fu and Kane (2007), Fu *et al.* (2007), Moore and Balents (2007), and Roy (2009a), where 16 topologically distinct states are possible. Most of these states can be viewed as stacked 2D QSH insulator planes, but one of them, the strong topological insulator, is genuinely 3D. The topological classification according to TBT is valid only for noninteracting systems, and it was not clear at the time whether these states are stable under more general topological deformations including interactions. Qi, Hughes, and Zhang (2008b) introduced the TFT of topological insulators and demonstrated that these states are indeed generally stable in the presence of interactions. Furthermore, a topologically invariant topological order parameter can be defined within the TFT as an experimentally measurable, quantized topological magnetoelectric effect (TME). The standard Maxwell's equations are modified by the topological terms, leading to the axion electrodynamics of the topological insulators. This work also showed that the 2D and 3D topological insulators are descendants of the 4D topological insulator state discovered by Zhang and Hu (2001) who motivated this series of recent developments. At this point, the two different paths based on the TBT and TFT converged, and a unified theoretical framework emerged.

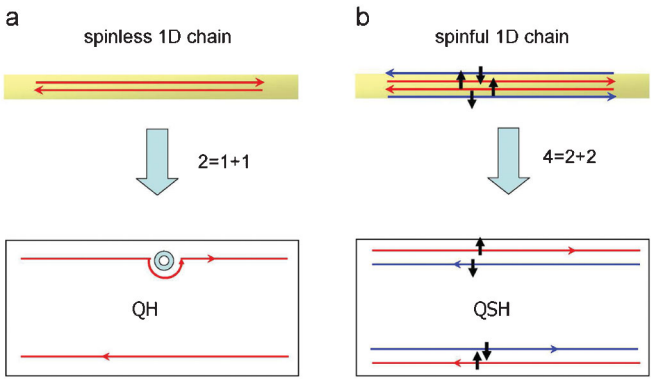

FIG. 1 (color). Analogy between QH and QSH effects: (a) A spinless 1D system has both forward and backward movers. These 2 basic degrees of freedom are spatially separated in a QH bar, as expressed by the symbolic equation $2 = 1 + 1$. The upper edge supports only a forward mover and the lower edge supports only a backward mover. The states are robust and go around an impurity without scattering. (b) A spinful 1D system has 4 basic degrees of freedom, which are spatially separated in a QSH bar. The upper edge supports a forward mover with spin up and a backward mover with spin down and conversely for the lower edge. That spatial separation is expressed by the symbolic equation $4 = 2 + 2$. Adapted from Qi and Zhang, 2010.

There are a number of excellent reviews on this subject (König *et al.*, 2008; Moore, 2010; Hasan and Kane, 2010; Qi and Zhang, 2010). This article attempts to give a simple pedagogical introduction to the subject and reviews the current status of the field. In Secs. II and III, we review the standard models, materials, and experiments for the 2D and the 3D topological insulators. These two sections can be understood without any prior knowledge of topology. In Sec. IV, we review the general theory of topological insulators, presenting both the TFT and the TBT. In Sec. V, we discuss an important generalization of topological insulators–topological superconductors.

II. TWO-DIMENSIONAL TOPOLOGICAL INSULATORS

The QSH state, or 2D topological insulator, was first discovered in HgTe/CdTe quantum wells. Bernevig, Hughes, and Zhang (2006) initiated the search for the QSH state in semiconductors with an "inverted" electronic gap and predicted a quantum phase transition in HgTe/CdTe quantum wells as a function of the thickness d_{QW} of the quantum well. The quantum well system is predicted to be a conventional insulator for $d_{\mathrm{QW}} < d_c$, and a QSH insulator with a single pair of helical edge states for $d_{\mathrm{QW}} > d_c$, where d_c is a critical thickness. The first experimental confirmation of the existence of the QSH state in HgTe/CdTe quantum wells was carried out by König *et al.* (2007). This work reported the observation of a nominally insulating state which conducts only through 1D edge channels and is strongly influenced by a TR symmetry-breaking magnetic field. Further transport measurements (Roth *et al.*, 2009) reported unique nonlocal conduction properties due to the helical edge states.

The QSH insulator state is invariant under TR, has a charge excitation gap in the 2D bulk, but has topologically protected

1D gapless edge states that lie inside the bulk insulating gap. The edge states have a distinct helical property: Two states with opposite spin polarization counterpropagate at a given edge (Kane and Mele, 2005a; Wu *et al.*, 2006; Xu and Moore, 2006). For this reason they are also called helical edge states, i.e., the spin is correlated with the direction of motion (Wu *et al.*, 2006). The edge states come in Kramers doublets, and TR symmetry ensures the crossing of their energy levels at special points in the Brillouin zone (BZ). Because of this level crossing, the spectrum of a QSH insulator cannot be adiabatically deformed into that of a topologically trivial insulator without helical edge states. Therefore, in this sense, the QSH insulator represents a new topologically distinct state of matter. In the special case that SOC preserves a $U(1)_s$ subgroup of the full SU(2) spin rotation group, the topological properties of the QSH state can be characterized by the spin Chern number (Sheng *et al.*, 2006). More generally, the topological properties of the QSH state are mathematically characterized by a $\mathbb{Z}_2$ topological invariant (Kane and Mele, 2005b). States with an even number of Kramers pairs of edge states at a given edge are topologically trivial, while those with an odd number are topologically nontrivial. The $\mathbb{Z}_2$ topological quantum number can also be defined for generally interacting systems and experimentally measured in terms of the fractional charge and quantized current on the edge (Qi, Hughes, and Zhang, 2008a), and spin-charge separation in the bulk (Qi and Zhang, 2008; Ran *et al.*, 2008).

In this section, we focus on the basic theory of the QSH state in the HgTe/CdTe system because of its simplicity and experimental relevance and provide an explicit and pedagogical discussion of the helical edge states and their transport properties. There are several other theoretical proposals for the QSH state, including bilayer bismuth (Murakami, 2006), and the ''broken-gap'' type-II AlSb/InAs/GaSb quantum wells (Liu, Hughes *et al.*, 2008). Initial experiments in the AlSb/InAs/GaSb system already show encouraging signatures (Knez *et al.*, 2010). The QSH system has also been proposed for the transition metal oxide Na_2IrO_3 (Shitade *et al.*, 2009). The concept of the fractional QSH state was proposed at the same time as the QSH state (Bernevig and Zhang, 2006) and has been recently investigated theoretically in more detail (Young *et al.*, 2008; Levin and Stern, 2009).

A. Effective model of the two-dimensional time-reversal-invariant topological insulator in HgTe/CdTe quantum wells

In this section we review the basic electronic structure of bulk HgTe and CdTe and presented a simple model first introduced by Bernevig, Hughes, and Zhang (2006) (BHZ) to describe the physics of those subbands of HgTe/CdTe quantum wells which are relevant for the QSH effect. HgTe and CdTe crystallize in the zinc blende lattice structure. This structure has the same geometry as the diamond lattice, i.e., two interpenetrating face-centered-cubic lattices shifted along the body diagonal, but with a different atom on each sublattice. The presence of two different atoms per lattice site breaks inversion symmetry and thus reduces the point group symmetry from O_h (cubic) to T_d (tetrahedral). However, even though inversion symmetry is explicitly broken, this has only a small effect on the physics of the QSH effect. To simplify the discussion, we first ignore this bulk inversion asymmetry (BIA).

For both HgTe and CdTe, the important bands near the Fermi level are close to the Γ point in the Brillouin zone [Fig. 2(a)]. They are a s-type band (Γ_6), and a p-type band split by SOC into a $J = 3/2$ band (Γ_8) and a $J = 1/2$ band (Γ_7). CdTe has a band ordering similar to GaAs with a s-type (Γ_6) conduction band, and p-type valence bands (Γ_8, Γ_7) which are separated from the conduction band by a large energy gap (~ 1.6 eV). Because of the large SOC present in the heavy element Hg, the usual band ordering is *inverted*: The negative energy gap of -300 meV indicates that the Γ_8 band, which usually forms the valence band, is above the Γ_6 band. The light-hole Γ_8 band becomes the conduction band, the heavy-hole band becomes the first valence band, and the s-type band (Γ_6) is pushed below the Fermi level to lie between the heavy-hole band and the spin-orbit split-off band (Γ_7) [Fig. 2(a)]. Because of the degeneracy between heavy-hole and light-hole bands at the Γ point, HgTe is a zero-gap semiconductor.

When HgTe-based quantum well structures are grown, the peculiar properties of the well material can be utilized to tune the electronic structure. For wide QW layers, quantum confinement is weak and the band structure remains inverted. However, the confinement energy increases when the well width is reduced. Thus, the energy levels will be shifted and, eventually, the energy bands will be aligned in a ''normal'' way, if the QW thickness d_{QW} falls below a critical thickness d_c. We can understand this heuristically as follows: for thin QWs the heterostructure should behave similarly to CdTe and have a normal band ordering, i.e., the bands with primarily Γ_6 symmetry are the conduction subbands and

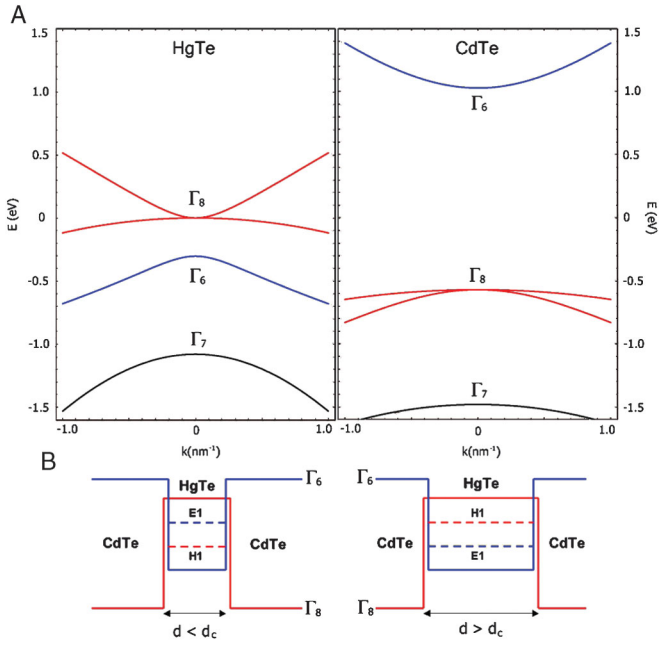

FIG. 2 (color). (a) Bulk band structure of HgTe and CdTe; (b) schematic picture of quantum well geometry and lowest subbands for two different thicknesses. From Bernevig *et al.*, 2006.

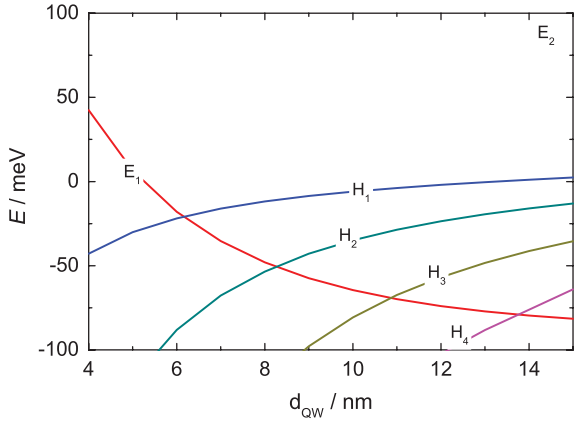

FIG. 3 (color). Energy levels of the QW as a function of QW width. From König *et al.*, 2008.

the Γ_8 bands contribute to the valence subbands. On the other hand, as d_{QW} is increased, we expect the material to behave more like HgTe which has inverted bands. As d_{QW} increases, we expect to reach a critical thickness where the Γ_8 and Γ_6 subbands cross and become inverted, with the Γ_8 bands becoming conduction subbands and the Γ_6 bands becoming valence subbands [Fig. 2(b)] (Novik *et al.*, 2005; Bernevig, Hughes, and Zhang, 2006). The shift of energy levels with d_{QW} is depicted in Fig. 3. The QW states derived from the heavy-hole Γ_8 band are denoted by H_n, where the subscript $n = 1, 2, 3, \ldots$ describes well states with an increasing number of nodes in the z direction. Similarly, the QW states derived from the electron Γ_6 band are denoted by E_n. The inversion between E_1 and H_1 bands occurs at a critical thickness $d_{\mathrm{QW}} = d_c \sim 6.3$ nm (Fig. 3). In the following, we develop a simple model and discuss why we expect QWs with $d_{\mathrm{QW}} > d_c$ to form TR invariant 2D topological insulators with protected edge states.

Under our assumption of inversion symmetry, the relevant subbands, E_1 and H_1, must be doubly degenerate since TR symmetry is present. We express states in the basis $\{|E_1+\rangle, |H_1+\rangle, |E_1-\rangle, |H_1-\rangle\}$, where $|E_1\pm\rangle$ and $|H_1\pm\rangle$ are two sets of Kramers partners. The states $|E_1\pm\rangle$ and $|H_1\pm\rangle$ have opposite parity; hence a Hamiltonian matrix element that connects them must be odd under parity. Thus, to lowest order in k, $(|E_1+\rangle, |H_1+\rangle)$ and $(|E_1-\rangle, |H_1-\rangle)$ will each be coupled generically via a term linear in k. The $|H_1+\rangle$ heavy-hole state is formed from the spin-orbit coupled p orbitals $|p_x + ip_y, \uparrow\rangle$, while the $|H_1-\rangle$ heavy-hole state is formed from the spin-orbit coupled p orbitals $|-(p_x - ip_y), \downarrow\rangle$. Therefore, to preserve rotation symmetry around the growth axis z, the matrix elements must by proportional to $k_\pm = k_x \pm ik_y$. The only terms allowed in the diagonal elements are terms that have even powers of k including k-independent terms. The subbands must come in degenerate pairs at each $\mathbf{k}$, so there can be no matrix elements between the $+$ state and the $-$ state of the same band. Finally, if there were nonzero matrix elements between $|E_1+\rangle, |H_1-\rangle$ and $|E_1-\rangle, |H_1+\rangle$, this would induce a higher-order process coupling the $\pm$ states of the same band and splitting the degeneracy. Therefore, these matrix elements are forbidden as well. These simple arguments lead to the following model:

$$\mathcal{H} = \begin{pmatrix} h(\mathbf{k}) & 0 \\ 0 & h^*(-\mathbf{k}) \end{pmatrix}, \tag{1}$$

$$h(\mathbf{k}) = \epsilon(\mathbf{k})\mathbb{I}_{2\times 2} + d_a(\mathbf{k})\sigma^a, \tag{2}$$

where $\mathbb{I}_{2\times 2}$ is the 2×2 identity matrix, and

$$\epsilon(\mathbf{k}) = C - D(k_x^2 + k_y^2), \qquad d_a(\mathbf{k}) = [Ak_x, -Ak_y, M(\mathbf{k})],$$
$$M(\mathbf{k}) = M - B(k_x^2 + k_y^2), \tag{3}$$

where A, B, C, D, and M are material parameters that depend on the QW geometry, and we choose the zero of energy to be the valence band edge of HgTe at $\mathbf{k} = 0$ (Fig. 2).

The bulk energy spectrum of the BHZ model is given by

$$E_\pm = \epsilon(k) \pm \sqrt{d_a d_a} \tag{4}$$

$$= \epsilon(k) \pm \sqrt{A^2(k_x^2 + k_y^2) + M^2(k)}. \tag{5}$$

For $B = 0$, the model reduces to two copies of the massive Dirac Hamiltonian in $(2 + 1)$D. The mass M corresponds to the energy difference between the E_1 and H_1 levels at the Γ point. The mass M changes sign at the critical thickness d_c, where E_1 and H_1 become degenerate. At the critical point, the system is described by two copies of the massless Dirac Hamiltonian, one for each spin, and at a single valley $\mathbf{k} = 0$. This situation is similar to graphene (Castro Neto *et al.*, 2009), which is also described by the massless Dirac Hamiltonian in $(2 + 1)$D. However, the crucial difference lies in the fact that graphene has four Dirac cones, consisting of two valleys and two spins, whereas we have two Dirac cones, one for each spin, and at a single valley. For $d_{\mathrm{QW}} > d_c$, the E_1 level falls below the H_1 level at the Γ point, and the mass M becomes negative. A pure massive Dirac model does not differentiate between a positive and negative mass M. Since we are dealing with a nonrelativistic system, the B term is generally allowed. In order to make the distinction clear, we call M the Dirac mass, and B the Newtonian mass, because it describes the usual nonrelativistic mass term with quadratic dispersion relation. We show later that the relative sign between the Dirac mass M and the Newtonian mass B is crucial to determine whether the model describes a topological insulator state with protected edge states or not.

HgTe has a crystal structure of the zinc blende type which lacks inversion symmetry, leading to a BIA term in the Hamiltonian, given to leading order by (König *et al.*, 2008)

$$H_{\mathrm{BIA}} = \begin{pmatrix} 0 & 0 & 0 & -\Delta_z \\ 0 & 0 & \Delta_z & 0 \\ 0 & \Delta_z & 0 & 0 \\ -\Delta_z & 0 & 0 & 0 \end{pmatrix}. \tag{6}$$

This term plays an important role in determining the spin orientation of the helical edge state. The topological phase transition in the presence of BIA has been investigated recently (Murakami *et al.*, 2007; König *et al.*, 2008). In addition, in an asymmetric QW structural inversion symmetry can be broken by a built-in electric field, leading to a SOC term of Rashba type in the effective Hamiltonian (Rothe *et al.*, 2010; Ström *et al.*, 2010). For simplicity, we focus

TABLE I. Material parameters for HgTe/CdTe quantum wells with different well thicknesses d.

d (Å)	A (eV Å)	B (eV · Å^2)	D (eV · Å^2)	M (eV)	Δ_z (eV)
55	3.87	−48.0	−30.6	0.009	0.0018
61	3.78	−55.3	−37.8	−0.000 15	0.0017
70	3.65	−68.6	−51.2	−0.010	0.0016

on symmetric QW witout SIA. In Table I, we give the parameters of the BHZ model for various values of d_{QW}.

For the purpose of studying the topological properties of this system, as well as the edge states, it is sometimes convenient to work with a lattice regularization of the continuum model (1) which gives the energy spectrum over the entire Brillouin zone, i.e., a tight-binding representation. Since all the interesting physics at low energy occurs near the Γ point, the behavior of the dispersion at energies much larger than the bulk gap at the Γ point is not important. Thus, we can choose a regularization to simplify our calculations. This simplified lattice model consists of replacing Eq. (3) by

$$\begin{aligned} \epsilon(\mathbf{k}) &= C - 2Da^{-2}(2 - \cos k_x a - \cos k_y a), \\ d_a(\mathbf{k}) &= [Aa^{-1}\sin k_x a, -Aa^{-1}\sin k_y a, M(\mathbf{k})], \\ M(\mathbf{k}) &= M - 2Ba^{-2}(2 - \cos k_x a - \cos k_y a). \end{aligned} \tag{7}$$

It is clear that near the Γ point, the lattice Hamiltonian reduces to the continuum BHZ model in Eq. (1). For simplicity, below we work in units where the lattice constant $a = 1$.

B. Explicit solution of the helical edge states

The existence of topologically protected edge states is an important property of the QSH insulator. The edge states can be obtained by solving the BHZ model (2) with an open boundary condition. Consider the model Hamiltonian (2) defined on the half-space $x > 0$ in the x–y plane. We can divide the model Hamiltonian into two parts,

$$\hat{H} = \tilde{H}_0 + \tilde{H}_1, \tag{8}$$

$$\begin{aligned} \tilde{H}_0 &= \tilde{\epsilon}(k_x) + \begin{pmatrix} \tilde{M}(k_x) & Ak_x & 0 & 0 \\ Ak_x & -\tilde{M}(k_x) & 0 & 0 \\ 0 & 0 & \tilde{M}(k_x) & -Ak_x \\ 0 & 0 & -Ak_x & -\tilde{M}(k_x) \end{pmatrix}, \\ \tilde{H}_1 &= -Dk_y^2 + \begin{pmatrix} -Bk_y^2 & iAk_y & 0 & 0 \\ -iAk_y & Bk_y^2 & 0 & 0 \\ 0 & 0 & -Bk_y^2 & iAk_y \\ 0 & 0 & -iAk_y & Bk_y^2 \end{pmatrix}, \end{aligned} \tag{9}$$

with $\tilde{\epsilon}(k_x) = C - Dk_x^2$ and $\tilde{M}(k_x) = M - Bk_x^2$. All k_x-dependent terms are included in $\tilde{H}_0$. For such a semi-infinite system, k_x needs to be replaced by the operator $-i\partial_x$. On the other hand, translation symmetry along the y direction is preserved, so that k_y is a good quantum number. For $k_y = 0$, we have $\tilde{H}_1 = 0$ and the wave equation is given by

$$\tilde{H}_0(k_x \to -i\partial_x)\Psi(x) = E\Psi(x). \tag{10}$$

Since $\tilde{H}_0$ is block diagonal, the eigenstates have the form

$$\Psi_\uparrow(x) = \begin{pmatrix} \psi_0 \\ \mathbf{0} \end{pmatrix}, \qquad \Psi_\downarrow(x) = \begin{pmatrix} \mathbf{0} \\ \psi_0 \end{pmatrix}, \tag{11}$$

where $\mathbf{0}$ is a two-component zero vector, and $\Psi_\uparrow(x)$ is related to $\Psi_\downarrow(x)$ by TR. For the edge states, the wave function $\psi_0(x)$ is localized at the edge and satisfies the wave equation

$$\begin{aligned} &\left[\tilde{\epsilon}(-i\partial_x) + \begin{pmatrix} \tilde{M}(-i\partial_x) & -iA_1\partial_x \\ -iA_1\partial_x & -\tilde{M}(-i\partial_x) \end{pmatrix}\right]\psi_0(x) \\ &\quad = E\psi_0(x), \end{aligned} \tag{12}$$

which has been solved analytically for open boundary conditions using different methods (König *et al.*, 2008; Zhou *et al.*, 2008; Linder *et al.*, 2009; Lu *et al.*, 2010). In order to show the existence of the edge states and to find the region where the edge states exist, we briefly review the derivation of the explicit form of the edge states by neglecting $\tilde{\epsilon}$ for simplicity (König *et al.*, 2008).

Neglecting $\tilde{\epsilon}$, the wave equation (12) has particle-hole symmetry. Therefore, we expect that a special edge state with $E = 0$ can exist. With the wave function ansatz $\psi_0 = \phi e^{\lambda x}$, Eq. (12) can be simplified to

$$(M + B\lambda^2)\tau_y\phi = -A\lambda\phi, \tag{13}$$

therefore the two-component wave function ϕ should be an eigenstate of the Pauli matrix τ_y. Defining a two-component spinor $\phi_\pm$ by $\tau_y\phi_\pm = \pm\phi_\pm$, Eq. (13) is simplified to a quadratic equation for λ. If λ is a solution for ϕ_+, then $-\lambda$ is a solution for ϕ_-. Consequently, the general solution is given by

$$\psi_0(x) = (ae^{\lambda_1 x} + be^{\lambda_2 x})\phi_- + (ce^{-\lambda_1 x} + de^{-\lambda_2 x})\phi_+, \tag{14}$$

where $\lambda_{1,2}$ satisfy

$$\lambda_{1,2} = \frac{1}{2B}\left(A \pm \sqrt{A^2 - 4MB}\right). \tag{15}$$

The coefficients a, b, c, and d can be determined by imposing the open boundary condition $\psi(0) = 0$. Together with the normalizability of the wave function in the region $x > 0$, the open boundary condition leads to an existence condition for the edge states: $\mathrm{Re}\lambda_{1,2} < 0$ ($c = d = 0$) or $\mathrm{Re}\lambda_{1,2} > 0$ ($a = b = 0$), where Re stands for the real part. As seen from Eq. (15), these conditions can be satisfied only in the inverted regime when $M/B > 0$. Furthermore, one can show that when $A/B < 0$, we have $\mathrm{Re}\lambda_{1,2} < 0$, while when $A/B > 0$, we have $\mathrm{Re}\lambda_{1,2} > 0$. Therefore, the wave function for the edge states at the Γ point is given by

$$\psi_0(x) = \begin{cases} a(e^{\lambda_1 x} - e^{\lambda_2 x})\phi_-, & A/B < 0, \\ c(e^{-\lambda_1 x} - e^{-\lambda_2 x})\phi_+, & A/B > 0. \end{cases} \quad (16)$$

The sign of A/B determines the spin polarization of the edge states, which is key in determining the helicity of the Dirac Hamiltonian for the topological edge states. Another important quantity characterizing the edge states is their decay length, which is defined as $l_c = \max\{|\mathrm{Re}\lambda_{1,2}|^{-1}\}$.

The effective edge model can be obtained by projecting the bulk Hamiltonian onto the edge states $\Psi_\uparrow$ and $\Psi_\downarrow$ defined in Eq. (11). This procedure leads to a 2×2 effective Hamiltonian defined by $H^{\alpha\beta}_{\mathrm{edge}}(k_y) = \langle \Psi_\alpha | (\tilde{H}_0 + \tilde{H}_1) | \Psi_\beta \rangle$. To leading order in k_y, we arrive at the effective Hamiltonian for the helical edge states:

$$H_{\mathrm{edge}} = A k_y \sigma^z. \quad (17)$$

For HgTe QWs, we have $A \simeq 3.6$ eV Å (König *et al.*, 2008), and the Dirac velocity of the edge states is given by $v = A/\hbar \simeq 5.5 \times 10^5$ m/s.

The analytical calculation above can be confirmed by exact numerical diagonalization of the Hamiltonian (2) on a strip of finite width, which can also include the contribution of the $\epsilon(\mathbf{k})$ term (Fig. 4). The finite decay length of the helical edge states into the bulk determines the amplitude for interedge tunneling (Zhou *et al.*, 2008; Hou *et al.*, 2009; Ström and Johannesson, 2009; Tanaka and Nagaosa, 2009; Teo and Kane, 2009; Zyuzin and Fiete, 2010).

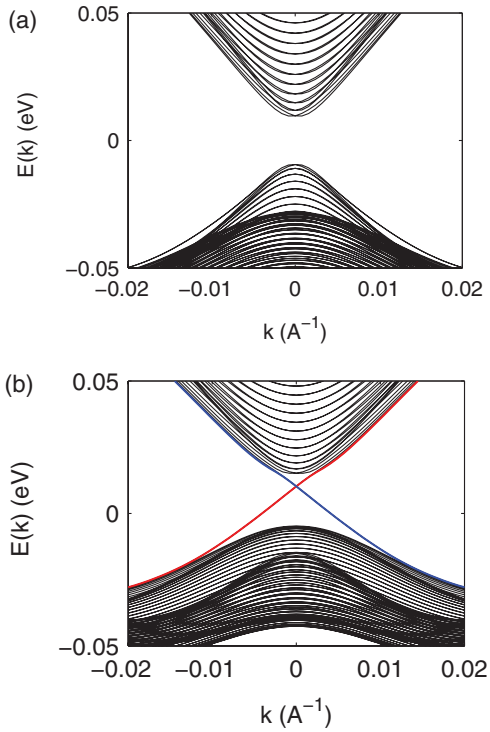

FIG. 4 (color). Energy spectrum of the effective Hamiltonian (2) in a cylinder geometry. In a thin QW, (a) there is a gap between conduction band and valence band. In a thick QW, (b) there are gapless edge states on the left and right edge (red and blue lines, respectively). Adapted from Qi and Zhang, 2010.

C. Physical properties of the helical edge states

1. Topological protection of the helical edge states

From the explicit analytical solution of the BHZ model, there is a pair of helical edge states exponentially localized at the edge, and described by the effective helical edge theory (17). In this context, the concept of "helical" edge state (Wu *et al.*, 2006) refers to the fact that states with opposite spin counterpropagate at a given edge, as we see from the edge state dispersion relation shown in Fig. 4(b), or the real-space picture shown in Fig. 1(b). This is in sharp contrast to the "chiral" edge states in the QH state, where the edge states propagate in one direction only, as shown in Fig. 1(a).

In the QH effect, the chiral edge states cannot be backscattered for sample widths larger than the decay length of the edge states. In the QSH effect, one may naturally ask whether backscattering of the helical edge states is possible. It turns out that TR symmetry prevents the helical edge states from backscattering. The absence of backscattering relies on the destructive interference between all possible backscattering paths taken by the edge electrons.

Before giving a semiclassical argument why this is so, we first consider an analogy from daily experience. Most eyeglasses and camera lenses have an antireflective coating [Fig. 5(a)], where light reflected from the top and bottom surfaces interferes destructively, leading to no net reflection and thus perfect transmission. However, this effect is not robust, as it depends on a precise matching between the wavelength of light and the thickness of the coating. Now we turn to the helical edge states. If a nonmagnetic impurity is present near the edge, it can in principle cause backscattering of the helical edge states due to SOC. However, just as for the reflection of photons by a surface, an electron can be reflected by a nonmagnetic impurity, and different reflection paths interfere quantum mechanically. A forward-moving electron with spin up on the QSH edge can make either a clockwise or

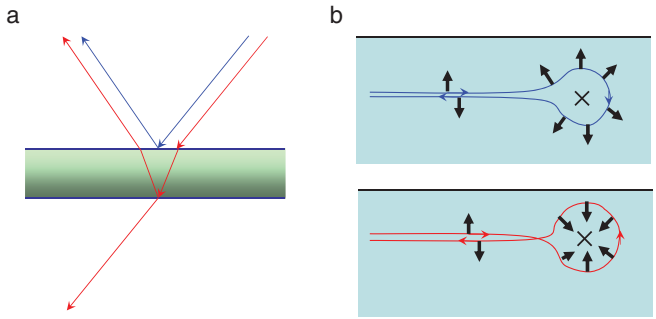

FIG. 5 (color). (a) On a lens with antireflective coating, light reflected by top (blue line) and bottom (red line) surfaces interferes destructively, leading to suppressed reflection. (b) Two possible paths taken by an electron on a QSH edge when scattered by a nonmagnetic impurity. The electron spin rotates by 180° clockwise along the blue curve and counterclockwise along the red curve. A geometrical phase factor associated with this rotation of the spin leads to destructive interference between the two paths. In other words, electron backscattering on the QSH edge is suppressed in a way similar to the way in which the reflection of photons is suppressed by an antireflective coating. Adapted from Qi and Zhang, 2010.

a counterclockwise turn around the impurity [Fig. 5(b)]. Since only spin-down electrons can propagate backward, the electron spin has to rotate adiabatically, either by an angle of π or $-\pi$, i.e., into the opposite direction. Consequently, the two paths differ by a full $\pi-(-\pi)=2\pi$ rotation of the electron spin. However, the wave function of a spin-1/2 particle picks up a negative sign under a full 2π rotation. Therefore, two backscattering paths related by TR always interfere destructively, leading to perfect transmission. If the impurity carries a magnetic moment, TR symmetry is explicitly broken, and the two reflected waves no longer interfere destructively. In this way, the robustness of the QSH edge state is protected by TR symmetry.

The physical picture described above applies only to the case of a single pair of QSH edge states (Kane and Mele, 2005a; Wu *et al.*, 2006; Xu and Moore, 2006). If there are two forward movers and two backward movers on a given edge, an electron can be scattered from a forward-moving to a backward-moving channel without reversing its spin. This spoils the perfect destructive interference described above and leads to dissipation. Consequently, for the QSH state to be robust, edge states must consist of an odd number of forward (backward) movers. This even-odd effect is the key reason why the QSH insulator is characterized by a $\mathbb{Z}_2$ topological quantum number (Kane and Mele, 2005a; Wu *et al.*, 2006; Xu and Moore, 2006).

The general properties of TR symmetry are important for understanding the properties of the edge theory. The antiunitary TR operator T takes different forms depending on whether the degrees of freedom have integer or half-odd-integer spin. For half-odd-integer spin, we have $T^2=-1$ which implies, by Kramers' theorem, that any single-particle eigenstate of the Hamiltonian must have a degenerate partner. From Fig. 4(b), we see that the two dispersion branches at one given edge cross each other at the TR invariant $k=0$ point. At this point, these two degenerate states exactly satisfy Kramers' theorem. If we add TR invariant perturbations to the Hamiltonian, we can move the degenerate point up and down in energy, but we cannot remove the degeneracy. In this precise sense, the helical edge states are topologically protected by TR symmetry.

If TR symmetry is not present, a simple "mass" term can be added to the Hamiltonian so that the spectrum becomes gapped:

$$H_{\text{mass}}=m\int\frac{dk}{2\pi}(\psi_{k+}^{\dagger}\psi_{k-}+\text{H.c.}),$$

where H.c. denotes Hermitian conjugation, and $\psi_{k\pm}^{\dagger}$, $\psi_{k\pm}$ are creation and annihilation operators for an edge electron of momentum k, with $\pm$ denoting the electron spin. The action of TR symmetry on the electron operators is given by

$$T\psi_{k+}T^{-1}=\psi_{-k,-},\qquad T\psi_{k-}T^{-1}=-\psi_{-k,+},\tag{18}$$

which implies

$$TH_{\text{mass}}T^{-1}=-H_{\text{mass}}.$$

Consequently, H_{mass} is a TR symmetry-breaking perturbation. More generally, if we define the "chirality" operator

$$C=N_{+}-N_{-}=\int\frac{dk}{2\pi}(\psi_{k+}^{\dagger}\psi_{k+}-\psi_{k-}^{\dagger}\psi_{k-}),$$

any operator that changes C by $2(2n-1)$, $n\in\mathbb{Z}$ is odd under TR. In other words, TR symmetry allows only $2n$-particle backscattering, described by operators such as $\psi_{k+}^{\dagger}\psi_{k'+}^{\dagger}\psi_{p-}\psi_{p'-}$ (for $n=1$). Therefore, the most relevant perturbation $\psi_{k+}^{\dagger}\psi_{k'-}$ is forbidden by TR symmetry, which is essential for the topological stability of the edge states. This edge state effective theory is nonchiral and is qualitatively different from the usual spinless or spinful Luttinger liquid theories. It can be considered as a new class of 1D critical theories, called a "helical liquid" (Wu *et al.*, 2006). Specifically, in the noninteracting case no TR invariant perturbation is available to induce backscattering, so that the edge state is robust.

Consider now the case of two flavors of helical edge states on the boundary, i.e., a 1D system consisting of two left movers and two right movers with Hamiltonian

$$H=\int\frac{dk}{2\pi}\sum_{s=1,2}(\psi_{ks+}^{\dagger}vk\psi_{ks+}-\psi_{ks-}^{\dagger}vk\psi_{ks-}).$$

A mass term such as $\tilde{m}\int(dk/2\pi)(\psi_{k1+}^{\dagger}\psi_{k2-}-\psi_{k1-}^{\dagger}\psi_{k2+}+\text{H.c.})$ (with $\tilde{m}$ real) can open a gap in the system while preserving time-reversal symmetry. In other words, two copies of the helical liquid form a topologically trivial theory. More generally, an edge system with TR symmetry is a nontrivial helical liquid when there is an odd number of left (right) movers and trivial when there is an even number of them. Thus the topology of QSH systems are characterized by a $\mathbb{Z}_2$ topological quantum number.

2. Interactions and quenched disorder

We now review the effect of interactions and quenched disorder on the QSH edge liquid (Wu *et al.*, 2006; Xu and Moore, 2006). Only two TR invariant nonchiral interactions can be added to Eq. (17), the forward and umklapp scatterings

$$H_f=g\int dx\psi_{+}^{\dagger}\psi_{+}\psi_{-}^{\dagger}\psi_{-},\tag{19}$$

$$H_u=g_u\int dx e^{-i4k_Fx}\psi_{+}^{\dagger}(x)\psi_{+}^{\dagger}(x+a)\times\psi_{-}(x+a)\psi_{-}(x)+\text{H.c.},\tag{20}$$

where the two-particle operators $\psi^{\dagger}\psi^{\dagger}$ and $\psi\psi$ are point split with the lattice constant a which plays the role of a short-distance cutoff. The chiral interaction terms renormalize only the Fermi velocity v and are thus ignored. It is well known that the forward scattering term gives a nontrivial Luttinger parameter $K=\sqrt{(v-g)/(v+g)}$, but keeps the system gapless. Only the umklapp term has the potential to open up a gap at the commensurate filling $k_F=\pi/2$. The bosonized form of the Hamiltonian reads

$$H=\int dx\frac{\bar{v}}{2}\left\{\frac{1}{K}(\partial_x\phi)^2+K(\partial_x\theta)^2\right\}+\frac{g_u\cos\sqrt{16\pi}\phi}{2(\pi a)^2},\tag{21}$$

where $\bar{v} = \sqrt{v^2 - g^2}$ is the renormalized velocity, and we define nonchiral bosons $\phi = \phi_R + \phi_L$ and $\theta = \phi_R - \phi_L$, where ϕ_R and ϕ_L are chiral bosons describing the spin-up (-down) right mover and the spin-down (-up) left mover, respectively. ϕ contains both spin and charge degrees of freedom and is equivalent to the combination $\phi_c - \theta_s$ in the spinful Luttinger liquid, with ϕ_c and θ_s the charge and spin bosons, respectively (Giamarchi, 2003). It is also a compact variable with period $\sqrt{\pi}$. A renormalization group analysis shows that the umklapp term is relevant for $K < 1/2$ with a pinned value of ϕ. Consequently, a gap $\Delta \sim a^{-1}(g_u)^{1/(2-4K)}$ opens and spin transport is blocked. The mass order parameters $N_{x,y}$, the bosonized form of which is $N_x = (i\eta_R\eta_L/2\pi a)\sin\sqrt{4\pi}\phi$ and $N_y = (i\eta_R\eta_L/2\pi a)\cos\sqrt{4\pi}\phi$, are odd under TR. For $g_u < 0$, ϕ is pinned at either 0 or $\sqrt{\pi}/2$, and the N_y order is Ising like. At $T = 0$, the system is in an Ising ordered phase, and TR symmetry is spontaneously broken. On the other hand, when $0 < T \ll \Delta$, N_y is disordered, the gap remains, and TR symmetry is restored by thermal fluctuations. A similar reasoning applies to the case $g_u > 0$, where N_x is the order parameter.

There is also the possibility of two-particle backscattering due to quenched disorder, described by the term

$$H_{\text{dis}} = \int dx \frac{g_u(x)}{2(\pi a)^2} \cos\sqrt{16\pi}[\phi(x,\tau) + \alpha(x)], \qquad (22)$$

where the scattering strength $g_u(x)$ and phase $\alpha(x)$ are Gaussian random variables. The standard replica analysis shows that disorder becomes relevant at $K < 3/8$ (Giamarchi and Schulz, 1988; Wu *et al.*, 2006; Xu and Moore, 2006). At $T = 0$, $N_{x,y}(x)$ exhibits glassy behavior, i.e., disordered in the spatial direction but static in the time direction. Spin transport is thus blocked and TR symmetry is again spontaneously broken at $T = 0$. At low but finite T, the system remains gapped with TR symmetry restored.

In the above, we have seen that the helical liquid can in principle be destroyed. However, for a reasonably weakly interacting system, i.e., $K \approx 1$, the one-component helical liquid remains gapless. In an Ising ordered phase, the low-energy excitations on the edge are Ising domain walls which carry fractional $e/2$ charge (Qi, Hughes, and Zhang, 2008). The properties of multicomponent helical liquids in the presence of disorder have also been studied (Xu and Moore, 2006).

A magnetic impurity on the edge of a QSH insulator is expected to act as a local mass term for the edge theory and thus is expected to lead to a suppression of the edge conductance. While this is certainly true for a static magnetic impurity, a *quantum* magnetic impurity, i.e., a Kondo impurity, leads to subtler behavior (Wu *et al.*, 2006; Maciejko *et al.*, 2009). In the presence of a quantum magnetic impurity, due to the combined effects of interactions and SOC one must also generally consider local two-particle backscattering processes (Meidan and Oreg, 2005) similar to Eq. (20), but occurring only at the position of the impurity. At high temperatures, both weak Kondo and weak two-particle backscattering are expected to give rise to a logarithmic temperature dependence as in the usual Kondo effect (Maciejko *et al.*, 2009), and their effect is not easily distinguishable. However, at low temperatures the physics depends drastically on the strength of Coulomb interactions on the edge, parametrized by the Luttinger parameter K. For weak Coulomb interactions $K > 1/4$, the edge conductance is restored to the unitarity limit $2e^2/h$ with unusual power laws characteristic of a "local helical liquid" (Wu *et al.*, 2006; Maciejko *et al.*, 2009). For strong Coulomb interactions $K < 1/4$, the conductance vanishes at $T = 0$, but is restored at low T by a fractionalized tunneling current of charge $e/2$ quasiparticles (Maciejko *et al.*, 2009). The tunneling of a charge $e/2$ quasiparticle is described by an instanton process which is the time counterpart to the static $e/2$ charge on a spatial magnetic domain wall along the edge (Qi, Hughes, and Zhang, 2008). In addition to the single-channel Kondo effect just described, the possibility of an even more exotic two-channel Kondo effect on the edge of the QSH insulator has also been recently studied (Law *et al.*, 2010).

3. Helical edge states and the holographic principle

There is an alternative way to understand the qualitative difference between an even or odd number of edge states in terms of a "fermion doubling" theorem (Wu *et al.*, 2006). This theorem states that there is always an even number of Kramers pairs at the Fermi energy for a TR invariant, but otherwise arbitrary 1D band structure. A single pair of helical states can occur only "holograhically," i.e., when the 1D system is the boundary of a 2D system. This fermion doubling theorem is a TR invariant generalization of the Nielsen-Ninomiya no-go theorem for chiral fermions on a lattice (Nielsen and Ninomiya, 1981). For spinless fermions, there is always an equal number of left movers and right movers at the Fermi level, which leads to the fermion doubling problem in odd spatial dimensions. A geometrical way to understand this result is that for periodic functions (i.e., energy spectra of a lattice model), "what goes up must eventually come down." Similarly, for a TR symmetric system with half-odd-integer spins, Kramers' theorem requires that each eigenstate of the Hamiltonian is accompanied by its TR conjugate or Kramers partner, so that the number of low-energy channels is doubled. A Kramers pair of states at $k = 0$ must recombine into pairs when k goes from 0 to π and 2π, which requires the bands to cross the Fermi level $4n$ times [Fig. 6(a)]. However, there is an exception to this theorem, which is analogous to the reason why a chiral liquid can exist in the QH effect. A helical liquid with an odd number of fermion branches can occur if it is holographic, i.e., if it appears at the boundary (edge) of a 2D system. In this case, the edge states are Kramers partners at $k = 0$, but merge into the bulk at some finite k_c, such that they do not have to be combined at $k = \pi$. More accurately, the edge states on both left and right boundaries become bulk states for $k > k_c$ and form a Kramers pair [Fig. 6(b)]. This is exactly the behavior discussed in Sec. II.B in the context of the analytical solution of the edge state wave functions.

The fermion doubling theorem also provides a physical understanding of the topological stability of the helical liquid. Any local perturbation on the boundary of a 2D QSH system is equivalent to the action of coupling a "dirty surface layer" to the unperturbed helical edge states. Whatever perturbation is considered, the dirty surface layer is always 1D, such that

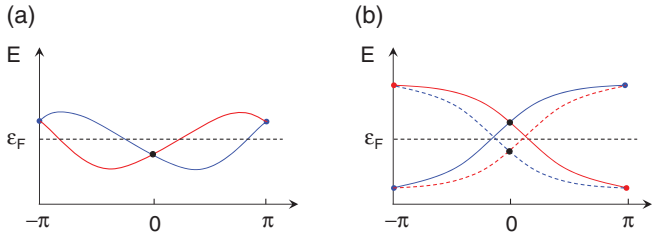

FIG. 6 (color). (a) Energy dispersion of a 1D TR invariant system. The Kramers degeneracy is required at $k = 0$ and $k = \pi$, so that the energy spectrum always crosses $4n$ times the Fermi level ϵ_F. (b) Energy dispersion of the helical edge states on one boundary of the QSH system (solid lines). At $k = 0$ the edge states are Kramers partners, while at $k = \pi$ they merge into the bulk and pair with the edge states of the other boundary (dashed lines). In both (a) and (b), red and blue lines represent the two partners of a Kramers pair. From König *et al.*, 2008.

there is always an even number of Kramers pairs of low-energy channels. Since the helical liquid has only an odd number of Kramers pairs, the coupling between them can only annihilate an *even* number of Kramers pairs if TR is preserved. As a result, at least one pair of gapless edge states can survive.

This fermion doubling theorem can be generalized to 3D in a straightforward way. In the 2D QSH state, the simplest helical edge state consists of a single massless Dirac fermion in (1 + 1)D. The simplest 3D topological insulator contains a surface state consisting of a single massless Dirac fermion in (2 + 1)D. A single massless Dirac fermion would also violate the fermion doubling theorem and cannot exist in a purely 2D system with TR symmetry. However, it can exist holographically, as the boundary of a 3D topological insulator. More generically, there is a one-to-one correspondence between topological insulators and robust gapless theories in one lower dimension (Schnyder *et al.*, 2008; Kitaev, 2009; Teo and Kane, 2010; Freedman *et al.*, 2011).

4. Transport theory of the helical edge states

In conventional diffusive electronics, bulk transport satisfies Ohm's law. Resistance is proportional to the length and inversely proportional to the cross-sectional area, implying the existence of a local resistivity or conductivity tensor. However, in systems such as the QH and QSH states, the existence of edge states necessarily leads to nonlocal transport which invalidates the concept of local resistivity. Such nonlocal transport has been experimentally observed in the QH regime in the presence of a large magnetic field (Beenakker and van Houten, 1991), and the nonlocal transport is well described by a quantum transport theory based on the Landauer-Büttiker formalism (Büttiker, 1988). A similar transport theory has been developed for the helical edge states of the QSH state, and the nonlocal transport experiments are in excellent agreement with theory (Roth *et al.*, 2009). These measurements are now widely acknowledged as constituting definitive experimental evidence for the existence of edge states in the QSH regime (Büttiker, 2009).

Within the general Landauer-Büttiker formalism (Büttiker, 1986), the current-voltage relationship is expressed as

$$I_i = \frac{e^2}{h}\sum_j (T_{ji}V_i - T_{ij}V_j), \tag{23}$$

where I_i is the current flowing out of the ith electrode into the sample region, V_i is the voltage on the ith electrode, and T_{ji} is the transmission probability from the ith to the jth electrode. The total current is conserved in the sense that $\sum_i I_i = 0$. A voltage lead j is defined by the condition that it draws no net current, i.e., $I_j = 0$. The physical currents remain unchanged if the voltages on all electrodes are shifted by a constant amount μ, implying that $\sum_i T_{ij} = \sum_i T_{ji}$. In a TR invariant system, the transmission coefficients satisfy the condition $T_{ij} = T_{ji}$.

For a general 2D sample, the number of transmission channels scales with the width of the sample, so that the transmission matrix T_{ij} is complicated and nonuniversal. However, a tremendous simplification arises if the quantum transport is entirely dominated by the edge states. In the QH regime, chiral edge states are responsible for the transport. For a standard Hall bar with N current and voltage leads attached, the transmission matrix elements for the $\nu = 1$ QH state are given by $T(\mathrm{QH})_{i+1,i} = 1$, for $i = 1, \ldots, N$, and all other matrix elements vanish identically. Here we periodically identify the $i = N + 1$ electrode with $i = 1$. Chiral edge states are protected from backscattering; therefore, the ith electrode transmits perfectly to the neighboring $(i + 1)$th electrode on one side only. In the example of current leads on electrodes 1 and 4, and voltage leads on electrodes 2, 3, 5, and 6 (see the inset of Fig. 12 for the labeling), one finds that $I_1 = -I_4 \equiv I_{14}$, $V_2 - V_3 = 0$, and $V_1 - V_4 = h/e^2 I_{14}$, giving a four-terminal resistance of $R_{14,23} = 0$ and a two-terminal resistance of $R_{14,14} = h/e^2$.

The helical edge states can be viewed as two copies of chiral edge states related by TR symmetry. Therefore, the transmission matrix is given by $T(\mathrm{QSH}) = T(\mathrm{QH}) + T^{\dagger}(\mathrm{QH})$, implying that the only nonvanishing matrix elements are given by

$$T(\mathrm{QSH})_{i+1,i} = T(\mathrm{QSH})_{i,i+1} = 1. \tag{24}$$

Considering again the example of current leads on electrodes 1 and 4, and voltage leads on electrodes 2, 3, 5, and 6, one finds that $I_1 = -I_4 \equiv I_{14}$, $V_2 - V_3 = (h/2e^2)I_{14}$, and $V_1 - V_4 = (3h/e^2)I_{14}$, giving a four-terminal resistance of $R_{14,23} = h/2e^2$ and a two-terminal resistance of $R_{14,14} = 3h/2e^2$. The four-terminal resistance with different configurations of voltage and current probes can be predicted in the same way, which are all rational fractions of h/e^2. The experimental data (see Fig. 16) neatly confirms all these highly nontrivial theoretical predictions (Roth *et al.*, 2009). For two micro Hall bar structures that differ only in the dimensions of the area between voltage contacts 3 and 4, the expected resistance values $R_{14,23} = \frac{h}{2e^2}$ and $R_{14,14} = \frac{3h}{2e^2}$ are indeed observed for gate voltages in which the samples are in the QSH regime.

As mentioned, one might sense a paradox between the dissipationless nature of the QSH edge states and the finite four-terminal longitudinal resistance $R_{14,23}$, which vanishes in the QH state. We can generally assume that the microscopic Hamiltonian governing the voltage leads is invariant under

TR symmetry. Therefore, one would naturally ask how such leads could cause the dissipation of the helical edge states that are protected from backscattering by TR symmetry? In nature, TR symmetry can be broken in two ways, either at the level of the microscopic Hamiltonian or at the level of the macroscopic irreversibility in systems whose microscopic Hamiltonian respects TR symmetry. When the helical edge states propagate without dissipation inside the QSH insulator between the electrodes, neither forms of TR symmetry breaking are present. As a result, the two counterpropagating channels can be maintained at two different quasichemical potentials, leading to a net current flow. However, once they enter the voltage leads, they interact with a reservoir containing a large number of low-energy degrees of freedom, and TR symmetry is effectively broken by the macroscopic irreversibility. As a result, the two counterpropagating channels equilibrate at the same chemical potential, determined by the voltage of the lead. Dissipation occurs with the equilibration process. The transport equation (23) breaks the macroscopic TR symmetry, even though the microscopic TR symmetry is ensured by the relationship $T_{ij} = T_{ji}$. In contrast to the case of the QH state, the absence of dissipation in the QSH helical edge states is protected by Kramers' theorem, which relies on the quantum phase coherence of wave functions. Thus, dissipation can occur once phase coherence is destroyed in the metallic leads. On the contrary, the robustness of QH chiral edge states does not require phase coherence. A more rigorous and microscopic analysis of the different role played by a metallic lead in QH and QSH states has been performed (Roth *et al.*, 2009), the result of which agrees with the simple transport equations (23) and (24). These two equations correctly describe the dissipationless quantum transport inside the QSH insulator and the dissipation inside the electrodes. As shown in Sec. II.F.4, these equations can be put to more stringent experimental tests.

The unique helical edge states of the QSH state can be used to construct devices with interesting transport properties (Yokoyama *et al.*, 2009; Akhmerov, Groth *et al.*, 2009; Kharitonov, 2010; L. B. Zhang *et al.*, 2010). Besides the edge state transport, the QSH state also leads to interesting bulk transport properties (Novik *et al.*, 2010).

D. Topological excitations

In the previous sections, we discussed the transport properties of the helical edge states in the QSH state. Unlike the case of the QH state, these transport properties are not expected to be precisely quantized, since they are not directly related to the $\mathbb{Z}_2$ topological invariant which characterizes the topological state. In this section, we show that it is possible to measure the $\mathbb{Z}_2$ topological quantum number directly in experiments. We discuss two examples. The first is the fractional charge and quantized current experiments at the edge of a QSH system (Qi, Hughes, and Zhang, 2008a). Second, we discuss the spin-charge separation effect occurring in the bulk of the sample (Qi and Zhang, 2008; Ran *et al.*, 2008).

1. Fractional charge on the edge

The first theoretical proposal we discuss is that of a localized fractional charge at the edge of a QSH sample when a magnetic domain wall is present on the edge, but the bulk remains TR invariant. The concept of fractional charge in a condensed matter system induced at a mass domain wall goes back to the Su-Schrieffer-Heeger (SSH) model (Su, Schrieffer, and Heeger, 1979). For spinless fermions, a mass domain wall induces a localized state with one-half of the electron charge. However, for a real material such as polyacetylene, two spin orientations are present for each electron, and because of this doubling, a domain wall in polyacetylene carries only integer charge. The proposal of SSH, and its counterpart in field theory, the Jackiw-Rebbi model (Jackiw and Rebbi, 1976), have never been experimentally realized. As mentioned, conventional 1D electronic systems have four basic degrees of freedom, i.e., forward and backward movers with two spins. However, a helical liquid at a given edge of the QSH insulator has only two: a spin-up (-down) forward mover and a spin-down (-up) backward mover. Therefore, the helical liquid has *one-half* the degrees of freedom of a conventional 1D system and thus avoids the doubling problem. Because of this fundamental topological property of the helical liquid, a domain wall carries charge $e/2$. In addition, if the magnetization is rotated periodically, a quantized charge current will flow. This provides a direct realization of the Thouless topological pump (Thouless, 1983).

We begin with the edge Hamiltonian given in Eq. (17). These helical fermion states have only 2 degrees of freedom; the spin polarization is correlated with the direction of motion. A mass term, being proportional to the Pauli matrices $\sigma^{1,2,3}$, can be introduced only in the Hamiltonian by coupling to a TR symmetry-breaking external field such as a magnetic field, aligned magnetic impurities (Gao *et al.*, 2009), or interaction-driven ferromagnetic order on the edge (Kharitonov, 2010). To leading order in perturbation theory, a magnetic field generates the mass terms

$$H_M = \int dx \Psi^\dagger \sum_{a=1,2,3} m_a(x,t)\sigma^a \Psi = \int dx \Psi^\dagger \sum_{a,i} t_{ai} B_i(x,t)\sigma^a \Psi, \tag{25}$$

where $\Psi = (\psi_+, \psi_-)^T$ and the model-dependent coefficient matrix t_{ai} is determined by the coupling of the edge states to the magnetic field. According to the work of Goldstone and Wilczek (1981), at zero temperature the ground-state charge density $j_0 \equiv \rho$ and current $j_1 \equiv j$ in a background field $m_a(x,t)$ are given by

$$j_\mu = \frac{1}{2\pi}\frac{1}{\sqrt{m_\alpha m^\alpha}} \epsilon^{\mu\nu}\epsilon^{\alpha\beta} m_\alpha \partial_\nu m_\beta, \qquad \alpha, \beta = 1, 2,$$

with $\mu, \nu = 0, 1$ corresponding to the time and space components, respectively, and m_3 does not enter the long-wavelength charge-response equation. If we parametrize the mass terms in terms of an angular variable θ, i.e., $m_1 = m\cos\theta$, $m_2 = m\sin\theta$, the response equation is simplified to

$$\rho = \frac{1}{2\pi}\partial_x \theta(x,t), \qquad j = -\frac{1}{2\pi}\partial_t \theta(x,t). \tag{26}$$

Such a response is topological in the sense that the net charge Q in a region $[x_1, x_2]$ at time t depends only on the boundary

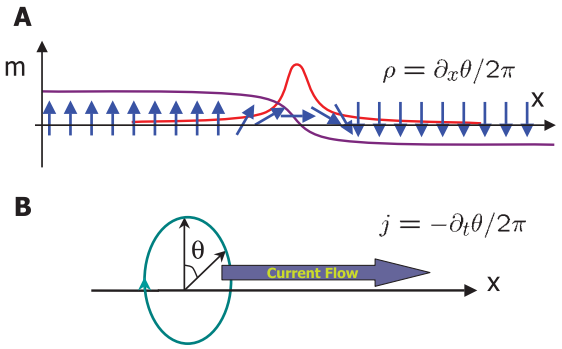

FIG. 7 (color). (a) Schematic of the half-charge on a domain wall. The blue arrows show a magnetic domain wall configuration and the purple line shows the mass kink. The red curve shows the charge density distribution. (b) Schematic of the pumping induced by the rotation of magnetic field. The blue circle with arrow shows the rotation of the magnetic field vector. Adapted from Qi, Hughes, and Zhang, 2008a.

values of $\theta(x, t)$, i.e., $Q = [\theta(x_2, t) - \theta(x_1, t)]/2\pi$. In particular, a half-charge $\pm e/2$ is carried by an antiphase domain wall of θ [Fig. 7(a)] (Jackiw and Rebbi, 1976). Similarly, the charge pumped by a purely time-dependent $\theta(t)$ field in a time interval $[t_1, t_2]$ is $\Delta Q_{\text{pump}}|_{t_1}^{t_2} = [\theta(t_2) - \theta(t_1)]/2\pi$. When θ is rotated from 0 to 2π adiabatically, a quantized charge e is pumped through the 1D system [Fig. 7(b)].

From the linear relation $m_a = t_{ai}B_i$, the angle θ can be determined for a given magnetic field $\mathbf{B}$. Independent from the details of t_{ai}, opposite magnetic fields $\mathbf{B}$ and $-\mathbf{B}$ always correspond to opposite mass, so that $\theta(\mathbf{B}) = \theta(-\mathbf{B}) + \pi$. Thus the charge localized on an antiphase magnetic domain wall of magnetization field is always $e/2$ mod e, which is a direct manifestation of the $\mathbb{Z}_2$ topological quantum number of the QSH state. Such a half-charge is detectable in a specially designed single-electron transistor device (Qi, Hughes, and Zhang, 2008).

2. Spin-charge separation in the bulk

In addition to the fractional charge on the edge, there have been theoretical proposals for a bulk spin-charge separation effect induced by a magnetic flux of $hc/2e$ (Qi and Zhang, 2008; Ran *et al.*, 2008). These ideas are similar to the $\mathbb{Z}_2$ spin pump proposed by Fu and Kane (2006). We first present an argument which is physically intuitive, but valid only when there is at least a $\mathrm{U}(1)_s$ spin rotation symmetry, e.g., when S_z is conserved. In this case, the QSH effect is simply defined as two copies of the QH effect, with opposite Hall conductances of $\pm e^2/h$ for opposite spin orientations. Without loss of generality, we first consider a disk geometry with an electromagnetic gauge flux of $\phi_\uparrow = \phi_\downarrow = hc/2e$, or simply π in units of $\hbar = c = e = 1$, through a hole at the center (Fig. 8). The gauge flux acts on both spin orientations, and the π flux preserves TR symmetry. We consider adiabatic processes $\phi_\uparrow(t)$ and $\phi_\downarrow(t)$, where $\phi_\uparrow(t) = \phi_\downarrow(t) = 0$ at $t = 0$, and $\phi_\uparrow(t) = \phi_\downarrow(t) = \pm\pi$ at $t = 1$. Since the flux of π is equivalent to the flux of $-\pi$, there are four different adiabatic processes all reaching the same final flux configuration. In process (a), $\phi_\uparrow(t) = -\phi_\downarrow(t)$ and $\phi_\uparrow(t = 1) = \pi$. In process (b), $\phi_\uparrow(t) = -\phi_\downarrow(t)$ and $\phi_\uparrow(t = 1) = -\pi$. In

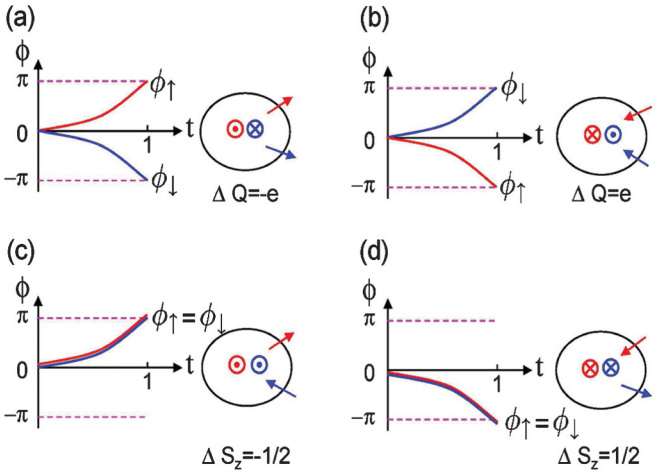

FIG. 8 (color). Four different adiabatic processes from $\phi_\uparrow = \phi_\downarrow = 0$ to $\phi_\uparrow = \phi_\downarrow = \pm\pi$. The red (blue) curve stands for the flux $\phi_{\uparrow(\downarrow)}(t)$, respectively. The symbol ⊙ (⊗) represents increasing (decreasing) fluxes, and the arrows show the current into and out of the Gaussian loop, induced by the changing flux. Charge is pumped in the processes with $\phi_\uparrow(t) = -\phi_\downarrow(t)$, while spin is pumped in those with $\phi_\uparrow(t) = \phi_\downarrow(t)$. From Qi and Zhang, 2008.

process (c), $\phi_\uparrow(t) = \phi_\downarrow(t)$ and $\phi_\uparrow(t = 1) = \pi$. In process (d), $\phi_\uparrow(t) = \phi_\downarrow(t)$ and $\phi_\uparrow(t = 1) = -\pi$. These four processes are illustrated in Fig. 8. Processes (a) and (b) preserve TR symmetry at all intermediate stages, while processes (c) and (d) preserve TR symmetry only at the final stage.

We consider a Gaussian loop surrounding the flux. As the flux $\phi_\uparrow(t)$ is turned on adiabatically, Faraday's law of induction states that a tangential electric field $\mathbf{E}_\uparrow$ is induced along the Gaussian loop. The quantized Hall conductance implies a radial current $\mathbf{j}_\uparrow = *(e^2/h)\hat{\mathbf{z}} \times \mathbf{E}_\uparrow$, resulting in a net charge flow $\Delta Q_\uparrow$ through the Gaussian loop:

$$\Delta Q_\uparrow = -\int_0^1 dt \int d\mathbf{n} \cdot \mathbf{j}_\uparrow = -\frac{e^2}{h}\int_0^1 dt \int d\boldsymbol{l} \cdot \mathbf{E}_\uparrow$$
$$= -\frac{e^2}{hc}\int_0^1 dt \frac{\partial\phi}{\partial t} = -\frac{e^2}{hc}\frac{hc}{2e} = -\frac{e}{2}. \quad (27)$$

An identical argument applied to the spin-down component shows that $\Delta Q_\downarrow = -e/2$. Therefore, this adiabatic process creates the holon state with $\Delta Q = \Delta Q_\uparrow + \Delta Q_\downarrow = -e$ and $\Delta S_z = \Delta Q_\uparrow - \Delta Q_\downarrow = 0$.

Applying similar arguments to process (b) gives $\Delta Q_\uparrow = \Delta Q_\downarrow = e/2$, which leads to a chargeon state with $\Delta Q = e$ and $\Delta S_z = 0$. Processes (c) and (d) give $\Delta Q_\uparrow = -\Delta Q_\downarrow = e/2$ and $\Delta Q_\uparrow = -\Delta Q_\downarrow = -e/2$, respectively, which yield the spinon states with $\Delta Q = 0$ and $\Delta S_z = \pm 1/2$. The Hamiltonians $H(t)$ in the presence of the gauge flux are the same at $t = 0$ and $t = 1$, but differ in the intermediate stages of the four adiabatic processes. Assuming that the ground state is unique at $t = 0$, we obtain four final states at $t = 1$, which are the holon, chargeon, and the two spinon states. Both the spin and the charge quantum numbers are sharply defined quantum numbers (Kivelson and Schrieffer, 1982). The insulating state has a bulk gap Δ, and an associated coherence length $\xi \sim A/\Delta$, where A is the Dirac parameter

in Eq. (1). As long as the radius of the Gaussian loop r_G far exceeds the coherence length, i.e., $r_G \gg \xi$, the spin and the charge quantum numbers are sharply defined with exponential accuracy.

When the spin rotation symmetry is broken but TR symmetry is still present, the concept of spin-charge separation is still well defined (Qi and Zhang, 2008). A spinon state can be defined as a Kramers doublet without any charge, and a holon or a chargeon is a Kramers singlet carrying charge $\pm e$. By combining the spin and charge flux threading (Essin and Moore, 2007), it can be shown generally that these spin-charge separated quantum numbers are localized near a $\phi = \pi$ flux (Qi and Zhang, 2008; Ran *et al.*, 2008). We clarify that the spin-charge separation effect discussed in topological insulators refers to the fractionalized quantum number, i.e., spin 1/2 charge 0 and spin 0 charge $\pm e$, induced by an external $hc/2e$ flux. This is a 2D analog of the spin-charge separation in the Su-Schrieffer-Heeger model of polyacetylene (Su *et al.*, 1979), where the spin-charge separated quantum number is carried by a charge density wave (CDW) domain wall, and the dynamics of such objects is determined by the dynamics of the domain wall. A 2D model system with spin-charge separated fundamental excitations can be obtained by coupling a topological insulator to a dynamical Z_2 gauge field (Ran *et al.*, 2008).

E. Quantum anomalous Hall insulator

Although TR invariance is essential in the QSH insulator, there is a TR symmetry-breaking state of matter which is closely related to the QSH insulator: the quantum anomalous Hall (QAH) insulator. The QAH insulator is a band insulator with quantized Hall conductance but without orbital magnetic field. Nearly two decades ago, Haldane (1988) proposed a model on a honeycomb lattice where the QH is realized without any external magnetic field, or the breaking of translational symmetry. However, the microscopic mechanism of circulating current loops within one unit cell has not been realized in any materials. Qi, Wu, and Zhang (2006) proposed a simple model based on the concept of the QAH insulator with ferromagnetic moments interacting with band electrons via the SOC. This simple model can be realized in real materials. Two recent proposals (Liu, Qi *et al.*, 2008; Yu *et al.*, 2010) made use of the properties of TR invariant topological insulators to realize the QAH state by magnetic doping. This is not accidental, but shows the deep relationship between these two states of matter. Thus we give a brief review of the QAH state in this section.

As a starting point, consider the upper 2×2 block of the QSH Hamiltonian (2):

$$h(\mathbf{k}) = \epsilon(\mathbf{k})\mathbb{I}_{2\times 2} + d_a(\mathbf{k})\sigma^a. \tag{28}$$

If we consider only these two bands, this model describes a TR symmetry-breaking system (Qi *et al.*, 2006). As long as there is a gap between the two bands, the Hall conductance of the system is quantized (Thouless *et al.*, 1982). The quantized Hall conductance is determined by the first Chern number of the Berry phase gauge field in the Brillouin zone, which, for the generic two-band model (28), reduces to

$$\sigma_H = \frac{e^2}{h}\frac{1}{4\pi}\int dk_x \int dk_y \hat{\mathbf{d}} \cdot \left(\frac{\partial \hat{\mathbf{d}}}{\partial k_x} \times \frac{\partial \hat{\mathbf{d}}}{\partial k_y}\right), \tag{29}$$

which is e^2/h times the winding number of the unit vector $\hat{\mathbf{d}}(\mathbf{k}) = \mathbf{d}(\mathbf{k})/|\mathbf{d}(\mathbf{k})|$ around the unit sphere. The $\mathbf{d}(\mathbf{k})$ vector defined in Eq. (3) has a skyrmion structure for $M/B > 0$ with winding number 1, while the winding number is 0 for $M/B < 0$. Just as in an ordinary QH insulator, the system with nontrivial Hall conductance e^2/h has one chiral edge state propagating on the edge. For the QSH system described by Eq. (2), the lower 2×2 block has the opposite Hall conductance, so that the total Hall conductance is zero, as guaranteed by TR symmetry. The chiral edge state of the QAH and its TR partner form the helical edge states of the QSH insulator.

When TR symmetry is broken, the two spin blocks are no longer related, and their charge Hall conductances no longer cancel exactly. For example, we can consider a different mass M for the two blocks, which breaks TR symmetry. If one block is in the trivial insulator phase ($M/B < 0$) and the other block is in the QAH phase ($M/B > 0$), the whole system becomes a QAH state with Hall conductance $\pm e^2/h$. Physically, this can be realized by exchange coupling with magnetic impurities. In a system doped with magnetic impurities, the spin splitting term induced by the magnetization is generically written as

$$H_s = \begin{pmatrix} G_E & 0 & 0 & 0 \\ 0 & G_H & 0 & 0 \\ 0 & 0 & -G_E & 0 \\ 0 & 0 & 0 & -G_H \end{pmatrix}, \tag{30}$$

where G_E and G_H describe the splitting of $E1$ and $H1$ bands, respectively, which are generically different. Adding H_s to the Hamiltonian (2), we see that the mass term M for the upper block is replaced by $M + (G_E - G_H)/2$, while that for the lower block is replaced by $M - (G_E - G_H)/2$. Therefore, the two blocks do acquire a different mass, which makes it possible to reach the QAH phase. After considering the effect of the identity term $(G_E + G_H)/2$, the condition for the QAH phase is given by $G_E G_H < 0$. When $G_E G_H > 0$ and $G_E \neq G_H$, the two blocks still acquire a different mass, but the system becomes metallic before the two blocks develop an opposite Hall conductance. Physically, we can also understand the physics from the edge state picture [Fig. 9(b)]. On the boundary of a QSH insulator there are counterpropagating edge states carrying opposite spin. When the spin splitting term increases, one of the two blocks, say the spin-down block, experiences a topological phase transition at $M = (G_E - G_H)/2$. The spin-down edge states penetrate deeper into the bulk due to the decreasing gap and eventually disappear, leaving only the spin-up state bound more strongly to the edge. Thus, the system has only spin-up edge states and evolves from the QSH state to the QAH state [Fig. 9(b)]. Although the discussion above is based on the specific model (2), the mechanism to generate a QAH insulator from a QSH insulator is generic. A QSH insulator can always evolve into a QAH insulator once a TR symmetry-breaking perturbation is introduced.

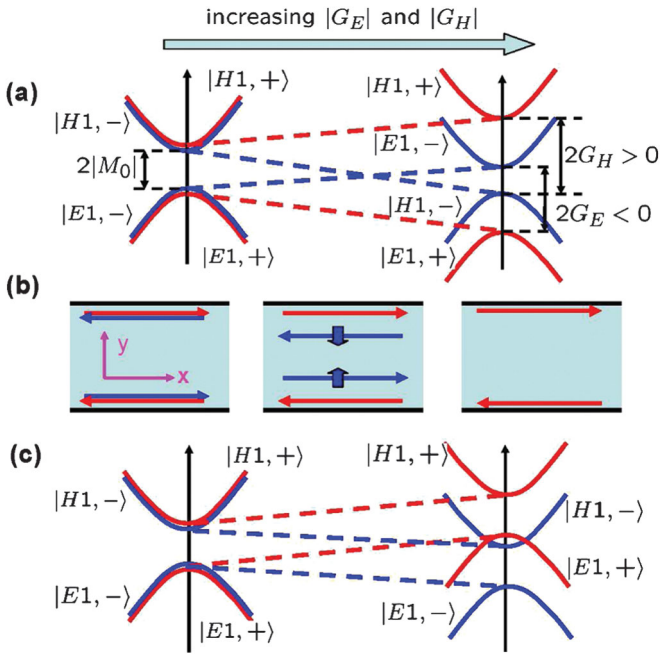

FIG. 9 (color). Evolution of band structure and edge states upon increasing the spin splitting. For (a) $G_E < 0$ and $G_H > 0$, the spin-down states $|E1,-\rangle$ and $|H1,-\rangle$ in the same block of the Hamiltonian (2) first touch each other, and then enter the normal regime. (b) Behavior of the edge states during the level crossing. For (c) $G_E > 0$ and $G_H > 0$, gap closing occurs between $|E1,+\rangle$ and $|H1,-\rangle$, which belong to different blocks of the Hamiltonian, and thus will cross each other without opening a gap. From Liu, Qi *et al.*, 2008.

Fortunately, in Mn-doped HgTe QWs the condition $G_E G_H < 0$ is indeed satisfied, so that the QAH phase exists in this system as long as the Mn spins are polarized. The microscopic reason for the opposite sign of G_E and G_H is the opposite sign of the *s-d* and *p-d* exchange couplings in this system (Liu, Qi *et al.*, 2008). Interestingly, in another family of QSH insulators, Bi_2Se_3 and Bi_2Te_3 thin films (Liu, Zhang *et al.*, 2010), the condition $G_E G_H < 0$ is also satisfied when magnetic impurities such as Cr or Fe are introduced into the system, but for a different physical reason. In HgTe QWs, the two bands in the upper block of the Hamiltonian (2) have the same direction of spin, but couple with the impurity spin with an opposite sign of exchange coupling because one band originates from *s* orbitals while the other originates from *p* orbitals. In Bi_2Se_3 and Bi_2Te_3, both bands originate from *p* orbitals, which have the same sign of exchange coupling with the impurity spin, but the sign of spin in the upper block is opposite (Yu *et al.*, 2010). Consequently, the condition $G_E G_H < 0$ is still satisfied. More details on the properties of the Bi_2Se_3 and Bi_2Te_3 family of materials can be found in the next section, since as bulk materials they are both 3D topological insulators.

F. Experimental results

1. Quantum well growth and the band inversion transition

As shown above, the transition from a normal to an inverted band structure coincides with the phase transition from a trivial insulator to the QSH insulator. In order to cover both the normal and the inverted band structure regimes, HgTe QW samples with a QW width in the range from 4.5 to 12.0 nm were grown (König, 2007; König *et al.*, 2007, 2008) by molecular beam epitaxy (MBE). Samples with mobilities of several 10^5 cm^2/(V s), even for low densities $n < 5 \times 10^{11}$ cm^{-2}, were available for transport measurements. In such samples, the mean free path is of the order of several microns. For the investigation of the QSH effect, devices in a Hall bar geometry (see Fig. 12, inset) of various dimensions were fabricated from QW structures with well widths of 4.5, 5.5, 6.4, 6.5, 7.2, 7.3, 8.0, and 12.0 nm.

For the investigation of the QSH effect, samples with a low intrinsic density $n(V_g = 0) < 5 \times 10^{11}$ cm^{-2} were studied. When a negative gate voltage V_g is applied to the top gate electrode of the device, the usual decrease in electron density is observed. In Fig. 10(a), measurements of the Hall resistance R_{xy} are presented for a Hall bar with length $L = 600$ and width $W = 200$ μm. The decrease of the carrier density is reflected in an increase of the Hall coefficient when the gate voltage is lowered from 0 to -1 V. In this voltage range, the density decreases linearly from 3.5×10^{11} to 0.5×10^{11} cm^{-2} [see Fig. 10(b)]. For even lower gate voltages, the sample becomes insulating, because the Fermi energy E_F is shifted into the bulk gap. When a large negative voltage $V_g \leq -2$ V is applied, the sample becomes conducting again. It can be inferred from the change in sign of the Hall coefficient that the device is *p* conducting. Thus, E_F has been shifted into the valence band, passing through the entire bulk gap.

The peculiar band structure of HgTe QWs gives rise to a unique LL dispersion. For a normal band structure, i.e., $d_{\mathrm{QW}} < d_c$, all LLs are shifted to higher energies for increasing magnetic fields [Fig. 11(a)]. This is the usual behavior and can be commonly observed in most materials. When the band structure of the HgTe QW is inverted for $d_{\mathrm{QW}} > d_c$, however, a significant change is observed for the LL dispersion [Fig. 11(b)]. Because of the inversion of electronlike and holelike bands, states near the bottom of the conduction band have predominantly *p* character. Consequently, the

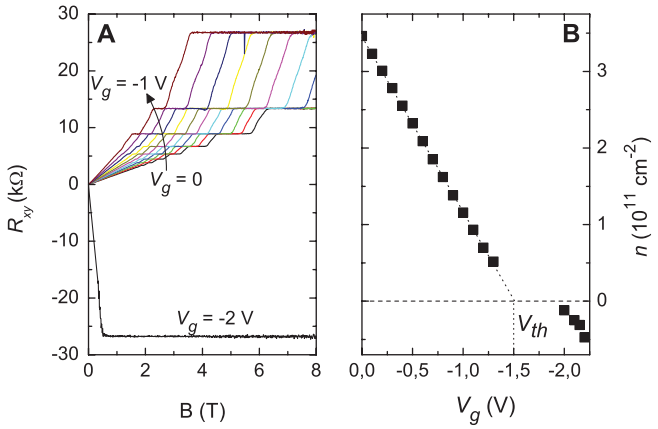

FIG. 10 (color). (a) Hall resistance R_{xy} for various gate voltages, indicating the transition from *n* to *p* conductance. (b) Gate-voltage-dependent carrier density deduced from Hall measurements. From König *et al.*, 2008.

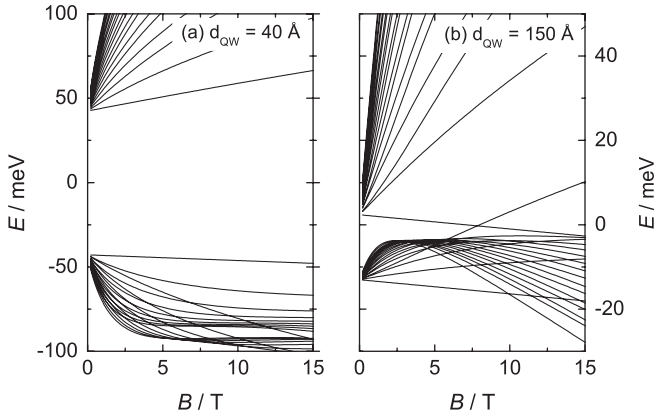

FIG. 11. Landau level dispersion for quantum well thicknesses of (a) 4.0 nm and (b) 15.0 nm. The qualitative behavior is indicative for samples with (a) normal and (b) inverted band structure. From König *et al.*, 2008.

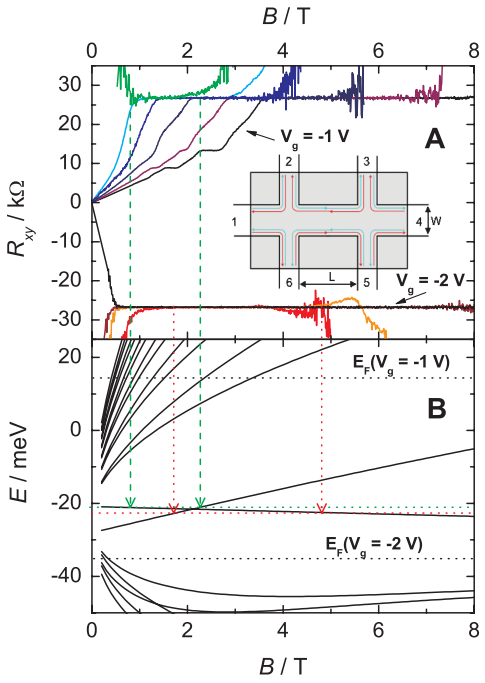

FIG. 12 (color). (a) Hall resistance R_{xy} of a $(L \times W) = (600 \times 200)$ μm^2 QW structure with 6.5 nm well width for different carrier concentrations obtained for different gate voltages V_g in the range from -1 to -2 V. For decreasing V_g, the n-type carrier concentration decreases and a transition to p-type conduction is observed, passing through an insulating regime between -1.4 and -1.9 V at zero field. (b) Landau level fan chart of a 6.5 nm quantum well obtained from an eight-band $\mathbf{k} \cdot \mathbf{p}$ calculation. Black dashed lines indicate the position of the Fermi energy E_F for gate voltages -1.0 and -2.0 V. Red and green dashed lines indicate the position of E_F for the red and green Hall resistance traces in (a). The crossing points of E_F with the respective Landau levels are marked by arrows of the same color. From König *et al.*, 2007.

energy of the lowest LL decreases with increasing magnetic field. On the other hand, states near the top of the valence band have predominantly s character, and the highest LL shifts to higher energies with increasing magnetic field. This leads to a crossing of these two peculiar LLs for a special value of the magnetic field. This behavior has been observed earlier by the Würzburg group and can now be demonstrated analytically within the BHZ model (König *et al.*, 2008). The exact magnetic field $\mathcal{B}_{\text{cross}}$ at which the crossing occurs depends on d_{QW}. The existence of the LL crossing is a clear signature of an inverted band structure, which corresponds to a negative energy gap with $M/B < 0$ in the BHZ model. The crossing of the LLs from the conduction and valence bands can be observed in experiments [Fig. 12(a)]. For gate voltages $V_g \geq -1.0$ and $V_g \leq -2.0$ V, E_F is clearly in the conduction band and valence band, respectively. When E_F is shifted toward the bottom of the conduction band, i.e., $V_g < -1.0$ V, a transition from a QH state with filling factor $\nu = 1$, i.e., $R_{xy} = h/e^2 = 25.8$ kΩ, to an insulating state is observed. Such behavior is expected independently of the details of the band structure, when the lowest LL of the conduction band crosses E_F for a finite magnetic field. When E_F is located within the gap, a nontrivial behavior can be observed for devices with an inverted band structure. Since the lowest LL of the conduction band lowers its energy with increasing magnetic field, it will cross E_F for a certain magnetic field. Subsequently, one occupied LL is below E_F, giving rise to the usual transport signatures of the quantum Hall regime, i.e., R_{xy} is quantized at h/e^2 and R_{xx} vanishes. When the magnetic field is increased, the LLs from the valence and conduction bands cross. Upon crossing, their "character" is exchanged, i.e., the level from the valence band turns into a conduction band LL and vice versa. The lowest LL of the conduction band now rises in energy for larger magnetic fields. Consequently, it will cross E_F for a certain magnetic field. Since E_F will be located within the fundamental gap afterward, the sample will become insulating again. Such a reentrant n-type QH state is shown in Fig. 12(a) for $V_g = -1.4$ V (green trace). For lower gate voltages, a corresponding behavior is observed for a p-type QH state (e.g., red trace for $V_g = -1.8$ V). As Fig. 12(b) shows, the experimental results are in good agreement with the theoretically calculated LL dispersion. The crossing point of the LLs in magnetic field $\mathcal{B}_{\text{cross}}$ can be determined accurately by tuning E_F through the energy gap. Thus, the width of the QW layer can be verified experimentally (König *et al.*, 2007).

Observation of a reentrant QH state is a clear indication of the nontrivial insulating behavior, which is a prerequisite for the existence of the QSH state. In contrast, trivial insulating behavior is obtained for devices with $d_{\text{QW}} < d_c$. For a normal band structure, the energy gap between the lowest LLs of the conduction and valence bands increases in the magnetic field [Fig. 11(a)]. Thus, a sample remains insulating in the magnetic field if E_F is located in the gap at zero field. The details of the physics of this reentrant QH state can be understood within the BHZ model with an added orbital magnetic field (König *et al.*, 2008). This nontrivial LL crossing could also be detected optically (Schmidt *et al.*, 2009).

2. Longitudinal conductance in the quantum spin Hall state

Initial evidence for the QSH state is revealed when Hall bars of dimensions $(L \times W) = (20.0 \times 13.3)$ μm^2 with different thickness d_{QW} are studied. For thin QW devices

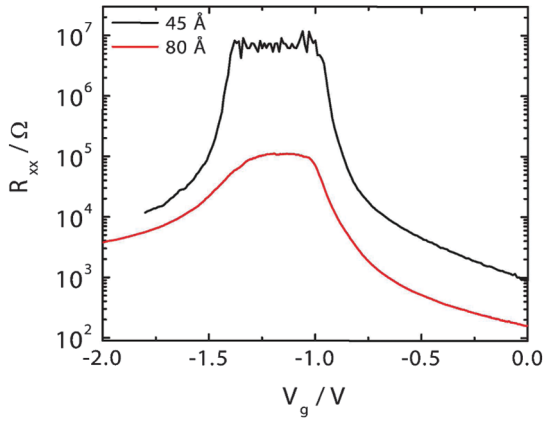

FIG. 13 (color). Longitudinal resistance of a 4.5 nm QW [dashed (black) line] and a 8.0 nm QW [solid (red) line] as a function of gate voltage. From König *et al.*, 2008.

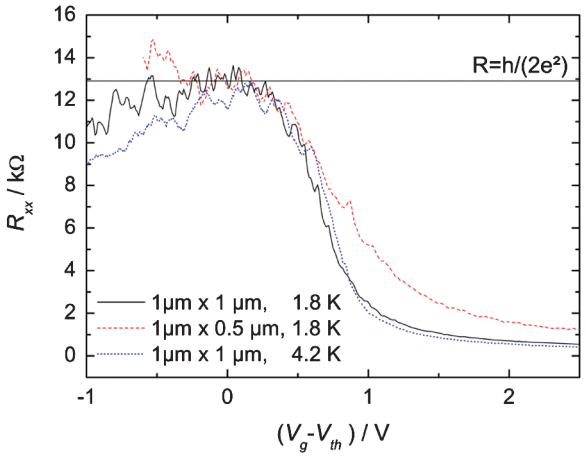

FIG. 14 (color). Longitudinal resistance as a function of gate voltage for two devices with $L = 1$ μm. The width W is 1 μm [solid (black) and dotted (blue) lines] and 0.5 μm [dashed (red) line]. The solid and dashed traces were obtained at a temperature of 1.8 K, and the dotted one at 4.2 K. From König *et al.*, 2008.

with $d_{\mathrm{QW}} < d_c$ and a normal band structure, the sample shows trivial insulating behavior (see Fig. 13). A resistance of several megaohms is measured when the Fermi level lies within the bulk insulating gap. This value can be attributed to the noise level of the measurement setup, and the intrinsic conductance is practically zero. For a thicker device with $d_{\mathrm{QW}} > d_c$ and an inverted band structure, however, the resistance does not exceed 100 kΩ. This behavior is reproduced for various Hall bars with a QW width in the range from 4.5 to 12.0 nm. While devices with a normal band structure, i.e., $d_{\mathrm{QW}} < d_c \approx 6.3$ nm, show trivial insulating behavior, a finite conductance in the insulating regime is observed for samples with an inverted band structure.

The obtained finite resistance $R \approx 100$ kΩ is significantly higher than the four-terminal resistance $h/(2e^2) \approx 12.9$ kΩ one anticipates for the geometry used in the experiments. The enhanced resistance in these samples with a length of $L = 20$ μm can be understood as a consequence of inelastic scattering. While, as discussed above, the helical edge states are robust against single-particle elastic backscattering, inelastic mechanisms can cause backscattering. For n-doped HgTe quantum wells, the typical mobility of the order of 10^5 cm^2/(V s) implies an elastic mean free path of the order of 1 μm (Daumer *et al.*, 2003). Lower mobilities can be anticipated for the QSH regime. The inelastic mean free path, which determines the length scale of undisturbed transport by the QSH edge states, can be estimated to be several times larger due to the suppression of phonons and the reduced electron-electron scattering at low temperatures. Thus, the inelastic scattering length is of the order of a few microns.

For the observation of the QSH conductance, the sample dimensions were reduced below the estimated inelastic mean free path. When Hall bars with a length $L = 1$ μm are studied, a four-terminal resistance close to $h/(2e^2)$ is observed. The threshold voltage Vth is defined such that the QSH regime is in the vicinity of $V_g = V$th. The slight deviation of R from the quantized value $h/(2e^2)$ can be attributed to some residual scattering. This is an indication that the length of the edge states still exceeds the inelastic mean free path. The results presented in Fig. 14 provide evidence that transport in the QSH regime indeed occurs due to edge states. The two devices with $W = 1.0$ and 0.5 μm were fabricated from the same QW structure. The resistance of the two devices differs significantly in the n-conducting regime, where transport is determined by bulk properties. In the QSH regime, however, both devices exhibit the same resistance, even though the width of the devices differs by a factor of 2. This fact clearly shows that the conductance is due to the edge states, which are independent of the sample width.

3. Magnetoconductance in the quantum spin Hall state

Another indication that the observed nontrivial insulating state is caused by the QSH effect is obtained by measurements in a magnetic field. The following experimental results were obtained on a Hall bar with dimensions $(L \times W) = (20.0 \times 13.3)$ μm^2 in a vector magnet system at a temperature of 1.4 K (König, 2007; König *et al.*, 2007). When a magnetic field is applied perpendicular to the QW layer, the QSH conductance decreases significantly already for small fields. A cusplike magnetoconductance peak is observed with a full width at half maximum $\mathcal{B}_{\mathrm{FWHM}}$ of 28 mT. Additional measurements show that the width of the magnetoconductance peak decreases with decreasing temperature. For example, $\mathcal{B}_{\mathrm{FWHM}} = 10$ mT is observed at 30 mK. For various devices of different sizes, a qualitatively similar behavior in magnetic field is observed.

When the magnetic field is tilted toward the plane of the QW, the magnetoconductance peak around $\mathcal{B} = 0$ widens steadily (see Fig. 15). For a tilt angle $\alpha = 90°$, i.e., when the magnetic field is in the QW plane, only a very small decrease in the conductance is observed. The decrease of the conductance for an in-plane field can be described by $\mathcal{B}_{\mathrm{FWHM}} \approx 0.7$ T for any in-plane orientation. From the results shown in Fig. 15, it is evident that a perpendicular field has a much larger influence on the QSH state than an in-plane field. The magnetoresistance in the QSH regime has been investigated theoretically (König *et al.*, 2008; Chu *et al.*, 2009; Tkachov and Hankiewicz, 2010; Maciejko, Qi, and Zhang, 2010). The large anisotropy can be understood by a

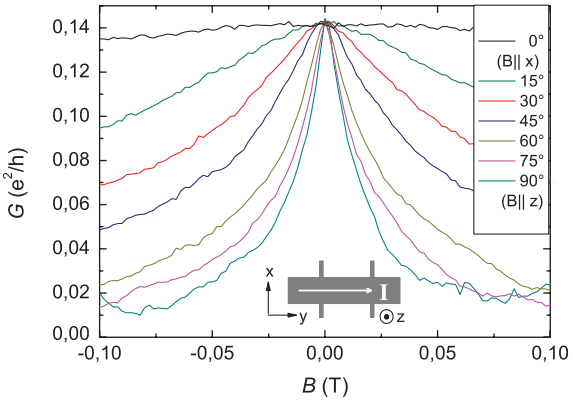

FIG. 15 (color). Four-terminal magnetoconductance $G_{14,23}$ in the QSH regime as a function of tilt angle between the QW plane and the applied magnetic field for a $d = 7.3$ nm QW structure with dimensions $(L \times W) = (20 \times 13.3)$ μm^2 measured in a vector field cryostat at a temperature of 1.4 K. From König *et al.*, 2008.

slightly modified version of the BHZ model with the inclusion of BIA terms and anisotropy in the g factor (König *et al.*, 2008; Maciejko, Qi, and Zhang, 2010). The cusp behavior in the magnetoconductance is possibly due to the presence of strong disorder; numerical simulations (Maciejko, Qi, and Zhang, 2010) are in good agreement with the experimental results.

4. Nonlocal conductance

Further confidence in the helical edge state transport can be gained by performing more extended multiterminal experiments (Roth *et al.*, 2009). The longitudinal resistance of a device was measured by passing a current through contacts 1 and 4 (see Fig. 16) and by detecting the voltage between contacts 2 and 3 ($R_{14,23}$). In this case, one obtains a result similar to the results found previously, i.e., a resistance $h/(2e^2)$ when the bulk of the device is gated into the insulating regime [see Fig. 16(a)]. However, the longitudinal resistance is significantly different in a slightly modified configuration, where the current is passed through contacts 1 and 3 and the voltage is measured between contacts 4 and 5 ($R_{13,45}$) [see Fig. 16(b)]. The result is $R_{13,45} \approx 8.6$ kΩ, which is markedly different from what one would expect for either QH transport or purely diffusive transport, where this

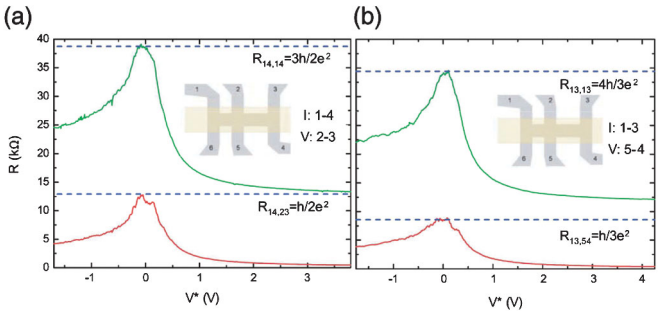

FIG. 16 (color). Experimental measurements of the four- and two-terminal resistance: (a) $R_{14,23}$ (red line) and $R_{14,14}$ (green line) and (b) $R_{13,54}$ (red line) and $R_{13,13}$ (green line). The dotted blue lines indicate the expected resistance value from the theory of the helical edge states. From Roth *et al.*, 2009.

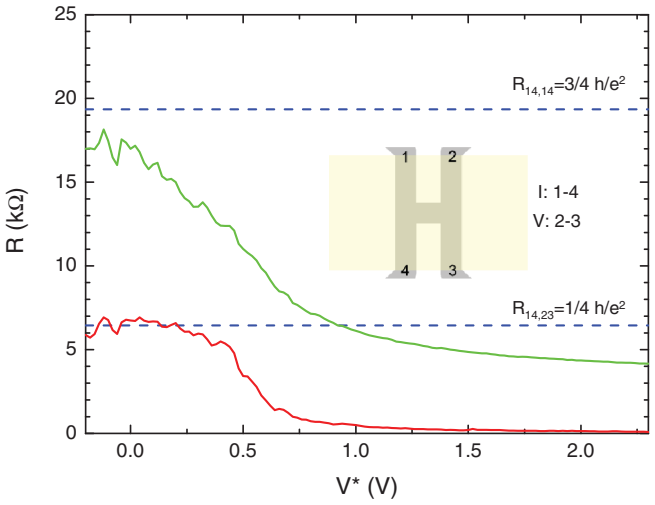

FIG. 17 (color). Nonlocal four-terminal resistance and two-terminal resistance measured on an H-bar device: $R_{14,23}$ (red line) and $R_{14,14}$ (green line). The dotted blue line represents the theoretically expected resistance. From Roth *et al.*, 2009.

configuration is equivalent to the previous one. However, the application of the transport equations (23) and (24) indeed predicts that the observed behavior is what one expects for helical edge channels. One easily finds that this resistance value can be expressed as an integer fraction of the inverse conductance quanta e^2/h: $R_{13,45} = h/3e^2$. This result shows that the current through the device is influenced by the number of Ohmic contacts in the current path. As discussed earlier, these Ohmic contacts lead to the equilibration inside the contact of the chemical potentials of the two counterpropagating helical edge channels.

Another measurement that directly confirms the nonlocal character of the helical edge channel transport in the QSH regime is shown in Fig. 17. This figure shows data obtained from a device in the shape of the letter "H." In this four-terminal device the current is passed through contacts 1 and 4 and the voltage is measured between contacts 2 and 3. In the metallic n-type regime (low gate voltage) the voltage signal tends to zero. In the QSH regime, however, the nonlocal resistance signal increases to ≈ 6.5 kΩ, which again fits perfectly to the result of Laudauer-Büttiker considerations $R_{14,23} = h/4e^2 \approx 6.45$ kΩ. Classically, one would expect only a minimal signal in this configuration (from Poisson's equation, assuming diffusive transport, one estimates a signal of about 40 Ω), and certainly not one that increases so strongly when the bulk of the sample is depleted. The signal measured here is fully nonlocal and can be taken (as was done 20 years ago for the QH regime) as definite evidence of the existence of edge channel transport in the QSH regime.

III. THREE-DIMENSIONAL TOPOLOGICAL INSULATORS

The model Hamiltonian for the 2D topological insulator in HgTe QWs also gives a basic template for generalization to 3D, leading to a simple model Hamiltonian for a class of materials: Bi_2Se_3, Bi_2Te_3, and Sb_2Te_3 (H. Zhang *et al.*, 2009). Similar to their 2D counterpart, the HgTe QWs, these materials can be described by a simple but realistic model,

where SOC drives a band inversion transition at the Γ point. In the topologically nontrivial phase, the bulk states are fully gapped, but there is a topologically protected surface state consisting of a single massless Dirac fermion. The 2D massless Dirac fermion is helical, in the sense that the electron spin points perpendicularly to the momentum, forming a left-handed helical texture in momentum space. Similar to the 1D helical edge states, a single massless Dirac fermion state is "holographic," in the sense that it cannot occur in a purely 2D system with TR symmetry, but can exist as the boundary of a 3D insulator. TR invariant single-particle perturbations cannot introduce a gap for the surface state. A gap can open for the surface state when a TR breaking perturbation is introduced on the surface. Moreover, the system becomes fully insulating, both in the bulk and on the surface. In this case, the topological properties of the fully gapped insulator are characterized by a novel topological magnetoelectric effect.

Soon after the theoretical prediction of the 3D topological insulator in the Bi_2Te_3, Sb_2Te_3, and Bi_2Se_3 (Xia *et al.*, 2009; H. Zhang *et al.*, 2009) class of materials, angle-resolved photoemission spectroscopy (ARPES) observed the surface states with a single Dirac cone (Chen *et al.*, 2009; Xia *et al.*, 2009; Hsieh *et al.*, 2009c). Furthermore, spin-resolved ARPES measurements indeed observed the left-handed helical spin texture of the massless Dirac fermion (Hsieh *et al.*, 2009c). These pioneering theoretical and experimental works inspired much of the subsequent developments reviewed in this section.

We take advantage of the model simplicity of the Bi_2Se_3, Bi_2Te_3, Sb_2Te_3 class of 3D topological insulators and give a pedagogical introduction based on this particular material system. In the next section, we introduce the general theory of the topological insulators. The electronic structure of the Bi_2Se_3, Bi_2Te_3, and Sb_2Te_3 class of topological insulators is simple enough to be captured by a simple model Hamiltonian. However, more powerful methods are needed to determine the topological properties of materials with a more complex electronic structure. In this regard, the TBT played an important role (Fu *et al.*, 2007; Moore and Balents, 2007; Roy, 2009b). In particular, a method due to Fu and Kane (2007) gives a simple algorithm to determine the topological properties of an arbitrarily complex electronic structure with inversion symmetry. This method predicts that Bi_xSb_{1-x} is a topological insulator for a certain range of composition x. ARPES measurements (Hsieh *et al.*, 2008) observed topologically nontrivial surface states in this system, giving the first example of a 3D topological insulator. The topological properties of this material have been further investigated both theoretically and experimentally (Teo *et al.*, 2008; Zhang, Liu, Qi, and Deng *et al.*, 2009; Nishide *et al.*, 2010). However, the surface states in Bi_xSb_{1-x} are rather complicated and cannot be described by simple model Hamiltonians. For this reason, we focus on the Bi_2Se_3, Bi_2Te_3, and Sb_2Te_3 class of topological insulators in this section.

A. Effective model of the three-dimensional topological insulator

In this review we focus on an effective model for 3D topological insulators (H. Zhang *et al.*, 2009), which, simply

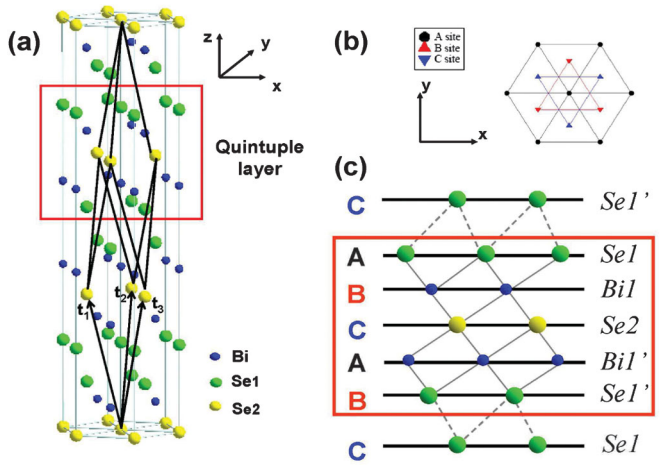

FIG. 18 (color). (a) Crystal structure of Bi_2Se_3 with three primitive lattice vectors denoted by $\mathbf{t}_{1,2,3}$. A quintuple layer with Se1-Bi1-Se2-Bi1′-Se1′ is indicated by the red box. (b) Top view along the z direction. Triangular lattice in one quintuple layer has three inequivalent positions, denoted by A, B, and C. (c) Side view of the quintuple layer structure. Along the z direction, Se and Bi atomic layers are stacked in the sequence $\cdots$-C(Se1′)-A(Se1)-B(Bi1)-C(Se2)-*A*(Bi1′)-B(Se1′)-C(Se1)-$\cdots$. The Se1 (Bi1) layer is related to the Se1′ (Bi1′) layer by inversion, where Se2 atoms play the role of inversion center. Adapted from H. Zhang *et al.*, 2009.

by adjusting parameters, is valid for studying the properties of Bi_2Se_3, Bi_2Te_3, and Sb_2Te_3. Bi_2Se_3, Bi_2Te_3, and Sb_2Te_3 share the same rhombohedral crystal structure with space group D_{3d}^5 ($R\bar{3}m$) and five atoms per unit cell. For example, the crystal structure of Bi_2Se_3 is shown in Fig. 18(a) and consists of a layered structure where individual layers form a triangular lattice. The important symmetry axes are a trigonal axis (three fold rotation symmetry) defined as the z axis, a binary axis (two fold rotation symmetry) defined as the x axis, and a bisectrix axis (in the reflection plane) defined as the y axis. The material consists of five-atom layers stacked along the z direction, known as quintuple layers. Each quintuple layer consists of five atoms per unit cell with two equivalent Se atoms denoted by Se1 and Se1′ in Fig. 18(c), two equivalent Bi atoms denoted by Bi1 and Bi1′ in Fig. 18(c), and a third Se atom denoted by Se2 in Fig. 18(c). The coupling between two atomic layers within a quintuple layer is strong, while that between quintuple layers is much weaker and predominantly of the van der Waals type. The primitive lattice vectors $\mathbf{t}_{1,2,3}$ and rhombohedral primitive unit cells are shown in Fig. 18(a). The Se2 site plays the role of an inversion center. Under inversion, Bi1 is mapped to Bi1′ and Se1 is mapped to Se1′.

To get a better understanding of the band structure and orbitals involved, we start from the atomic energy levels and then consider the effects of crystal field splitting and SOC on the energy eigenvalues at the Γ point in momentum space. This is summarized schematically in three stages: (I), (II), and (III) [see Fig. 19(a)]. Since the states near the Fermi level are primarily from p orbitals, we neglect the s orbitals and start from the atomic p orbitals of Bi (electronic configuration $6s^26p^3$) and Se ($4s^24p^4$). In stage (I), we consider chemical

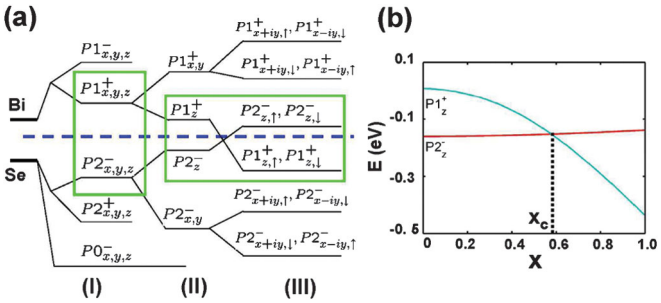

FIG. 19 (color). (a) Schematic picture of the evolution from the atomic $p_{x,y,z}$ orbitals of Bi and Se into the conduction and valence bands of Bi_2Se_3 at the Γ point. The three different stages (I), (II), and (III) represent the effect of turning on chemical bonding, crystal field splitting, and SOC, respectively (see text). The dashed blue line represents the Fermi energy. (b) The energy levels $|P1_z^+\rangle$ and $|P2_z^-\rangle$ of Bi_2Se_3 at the Γ point vs an artificially rescaled atomic SOC $\lambda(\mathrm{Bi}) = x\lambda_0(\mathrm{Bi}) = 1.25x$ (eV), $\lambda(\mathrm{Se}) = x\lambda_0(\mathrm{Se}) = 0.22x$ (eV) (see text). A level crossing occurs between these two states at $x = x_c \simeq 0.6$. Adapted from H. Zhang *et al.*, 2009.

bonding between Bi and Se atoms within a quintuple layer, which corresponds to the largest energy scale in this problem. First, we recombine the orbitals in a single unit cell according to their parity. This results in three states (two odd, one even) from each Se p orbital and two states (one odd, one even) from each Bi p orbital. The formation of chemical bonds hybridizes the states on the Bi and Se atoms, and pushes down all the Se states and lifts all the Bi states. In Fig. 19(a), these five hybridized states are labeled as $|P1^{\pm}_{x,y,z}\rangle$, $|P2^{\pm}_{x,y,z}\rangle$, and $|P0^{-}_{x,y,z}\rangle$, where the superscripts ± stand for the parity of the corresponding states. In stage (II), we consider the effect of crystal field splitting between different p orbitals. According to the point group symmetry, the p_z orbital is split from the p_x and p_y orbitals while the latter two remain degenerate. After this splitting, the energy levels closest to the Fermi energy turn out to be the p_z levels $|P1_z^+\rangle$ and $|P2_z^-\rangle$. In the last stage (III), we take into account the effect of SOC. The atomic SOC Hamiltonian is given by $H_{\mathrm{SO}} = \lambda \mathbf{L}\cdot\mathbf{S}$, with $\mathbf{L}$, $\mathbf{S}$ the orbital and spin angular momentum, respectively, and λ the strength of SOC. The SOC Hamiltonian mixes spin and orbital angular momenta while preserving the total angular momentum. This leads to a level repulsion between $|P1_z^+,\uparrow\rangle$ and $|P1^+_{x+iy},\downarrow\rangle$, and between similar combinations. Consequently, the energy of the $|P1_z^+,\uparrow(\downarrow)\rangle$ state is pushed down by the effect of SOC, and the energy of the $|P2_z^-,\uparrow(\downarrow)\rangle$ state is pushed up. If SOC is larger than a critical value $\lambda > \lambda_c$, the order of these two energy levels is reversed. To illustrate this inversion process explicitly, the energy levels $|P1_z^+\rangle$ and $|P2_z^-\rangle$ have been calculated (H. Zhang *et al.*, 2009) for a model Hamiltonian of Bi_2Se_3 with artificially rescaled atomic SOC parameters $\lambda(\mathrm{Bi}) = x\lambda_0(\mathrm{Bi})$, $\lambda(\mathrm{Se}) = x\lambda_0(\mathrm{Se})$, as shown in Fig. 19(b). Here $\lambda_0(\mathrm{Bi}) = 1.25$ eV and $\lambda_0(\mathrm{Se}) = 0.22$ eV are the actual values of the SOC strength for Bi and Se atoms, respectively (Wittel and Manne, 1974). From Fig. 19(b), one can clearly see that a level crossing occurs between $|P1_z^+\rangle$ and $|P2_z^-\rangle$ when the SOC strength is about 60% of its actual value. Since these two levels have opposite parity, the inversion between them drives the system into a topological insulator phase, similar to the case of HgTe QWs (Bernevig *et al.*, 2006). Therefore, the mechanism for the occurrence of a 3D topological insulating phase in this system is closely analogous to the mechanism for the 2D QSH effect (2D topological insulator) in HgTe (Bernevig *et al.*, 2006). More precisely, to determine whether or not an inversion-symmetric crystal is a topological insulator, we must have full knowledge of the states at all of the eight TR invariant momenta (TRIM) (Fu and Kane, 2007). The system is a (strong) topological insulator if and only if the band inversion between states with opposite parity occurs at an odd number of TRIM. The parity of the Bloch states at all TRIM have been studied by *ab initio* methods for the four materials Bi_2Se_3, Bi_2Te_3, Sb_2Se_3, and Sb_2Te_3 (H. Zhang *et al.*, 2009). Comparing the Bloch states with and without SOC, one concludes that Sb_2Se_3 is a trivial insulator, while the other three are topological insulators. For the three topological insulators, the band inversion occurs only at the Γ point.

Since the topological nature is determined by the physics near the Γ point, it is possible to write down a simple effective Hamiltonian to characterize the low-energy, long-wavelength properties of the system. Starting from the four low-lying states $|P1_z^+,\uparrow(\downarrow)\rangle$ and $|P2_z^-,\uparrow(\downarrow)\rangle$ at the Γ point, such a Hamiltonian can be constructed by the theory of invariants (Winkler, 2003) at a finite wave vector $\mathbf{k}$. The important symmetries of the system are TR symmetry T, inversion symmetry I, and threefold rotation symmetry C_3 around the z axis. In the basis $\{|P1_z^+,\uparrow\rangle, |P2_z^-,\uparrow\rangle, |P1_z^+,\downarrow\rangle, |P2_z^-,\downarrow\rangle\}$, the representation of these symmetry operations is given by $T = i\sigma^y\mathcal{K}\otimes\mathbb{I}_{2\times2}$, $I = \mathbb{I}_{2\times2}\otimes\tau_3$, and $C_3 = \exp[i(\pi/3)\sigma^z\otimes\mathbb{I}_{2\times2}]$, where $\mathbb{I}_{n\times n}$ is the $n\times n$ identity matrix, $\mathcal{K}$ is the complex conjugation operator, and $\sigma^{x,y,z}$ and $\tau^{x,y,z}$ denote the Pauli matrices in the spin and orbital space, respectively. By requiring these three symmetries and keeping only terms up to quadratic order in $\mathbf{k}$, we obtain the following generic form of the effective Hamiltonian:

$$H(\mathbf{k}) = \epsilon_0(\mathbf{k})\mathbb{I}_{4\times4} + \begin{pmatrix} \mathcal{M}(\mathbf{k}) & A_1k_z & 0 & A_2k_- \\ A_1k_z & -\mathcal{M}(\mathbf{k}) & A_2k_- & 0 \\ 0 & A_2k_+ & \mathcal{M}(\mathbf{k}) & -A_1k_z \\ A_2k_+ & 0 & -A_1k_z & -\mathcal{M}(\mathbf{k}) \end{pmatrix}, \tag{31}$$

with $k_\pm = k_x \pm ik_y$, $\epsilon_0(\mathbf{k}) = C + D_1k_z^2 + D_2k_\perp^2$, and $\mathcal{M}(\mathbf{k}) = M - B_1k_z^2 - B_2k_\perp^2$. The parameters in the effective model can be determined by fitting the energy spectrum of the effective Hamiltonian to that of *ab initio* calculations (H. Zhang *et al.*, 2009; Liu, Qi *et al.*, 2010; W. Zhang *et al.*, 2010). The fitting leads to the parameters displayed in Table II (Liu, Qi *et al.*, 2010).

Except for the identity term $\epsilon_0(\mathbf{k})$, the Hamiltonian (31) is similar to the 3D Dirac model with uniaxial anisotropy along the z direction, but with the crucial difference that the mass term is $\mathbf{k}$ dependent. From the fact that $M, B_1, B_2 > 0$ we can see that the order of the bands $|T1_z^+,\uparrow(\downarrow)\rangle$ and $|T2_z^-,\uparrow(\downarrow)\rangle$ is inverted around $\mathbf{k} = 0$ compared to large $\mathbf{k}$, which correctly characterizes the topologically nontrivial nature of the system. In addition, the Dirac mass M, i.e., the bulk insulating

TABLE II. The parameters in the model Hamiltonian (31) obtained from fitting to *ab initio* calculation. Adapted from Liu, Qi *et al.*, 2010.

	Bi_2Se_3	Bi_2Te_3	Sb_2Te_3
A_1 (eV Å)	2.26	0.30	0.84
A_2 (eV Å)	3.33	2.87	3.40
C (eV)	−0.0083	−0.18	0.001
D_1 (eV Å^2)	5.74	6.55	−12.39
D_2 (eV Å^2)	30.4	49.68	−10.78
M (eV)	0.28	0.30	0.22
B_1 (eV Å^2)	6.86	2.79	19.64
B_2 (eV Å^2)	44.5	57.38	48.51

gap, is ~0.3 eV, which allows the possibility of having a room-temperature topological insulator. Such an effective model can be used for further theoretical study of the Bi_2Se_3 system, as long as low-energy properties are concerned.

Corrections to the effective Hamiltonian (31) that are of higher order in $\mathbf{k}$ can also be considered. To cubic (k^3) order, some new terms can break the continuous rotation symmetry around the z axis to a discrete threefold rotation symmetry C_3. Correspondingly, the Fermi surface of the surface state acquires a hexagonal shape (Fu, 2009), which leads to important consequences for experiments on topological insulators such as surface-state quasiparticle interference (Zhou *et al.*, 2009; P. Lee, 2009; T. Zhang *et al.*, 2009; Alpichshev *et al.*, 2010). A modified version of the effective model (31) taking into account corrections up to k^3 has been obtained for the three topological insulators Bi_2Se_3, Bi_2Te_3, and Sb_2Te_3 based on *ab initio* calculations (Liu, Qi *et al.*, 2010). In this same work (Liu, Qi *et al.*, 2010), an eight-band model is also proposed for a more quantitative description of this family of topological insulators.

B. Surface states with a single Dirac cone

The existence of topological surface states is one of the most important properties of topological insulators. The surface states can be directly extracted from *ab initio* calculations by constructing maximally localized Wannier functions and calculating the local density of states on an open boundary (H. Zhang *et al.*, 2009). The result for the Bi_2Se_3 family of materials is shown in Figs. 20(a)–20(d), where one can clearly see the single Dirac-cone surface state for the three topologically nontrivial materials. However, to obtain a better understanding of the physical origin of topological surface states, it is helpful to show how the surface states emerge from the effective model (31) (Linder *et al.*, 2009; H. Zhang *et al.*, 2009; Lu *et al.*, 2010; Liu, Zhang *et al.*, 2010). The surface states can be obtained in a similar way as the edge states of the BHZ model (see Sec. II.B).

Consider the model Hamiltonian (31) on the half-space $z > 0$. In the same way as in the 2D case, we can divide the model Hamiltonian into two parts,

$$\hat{H} = \tilde{H}_0 + \tilde{H}_1, \tag{32}$$

$$\tilde{H}_0 = \tilde{\epsilon}(k_z) + \begin{pmatrix} \tilde{M}(k_z) & A_1 k_z & 0 & 0 \\ A_1 k_z & -\tilde{M}(k_z) & 0 & 0 \\ 0 & 0 & \tilde{M}(k_z) & -A_1 k_z \\ 0 & 0 & -A_1 k_z & -\tilde{M}(k_z) \end{pmatrix},$$
$$\tilde{H}_1 = D_2 k_\perp^2 + \begin{pmatrix} -B_2 k_\perp^2 & 0 & 0 & A_2 k_- \\ 0 & B_2 k_\perp^2 & A_2 k_- & 0 \\ 0 & A_2 k_+ & -B_2 k_\perp^2 & 0 \\ A_2 k_+ & 0 & 0 & B_2 k_\perp^2 \end{pmatrix}, \tag{33}$$

with $\tilde{\epsilon}(k_z) = C + D_1 k_z^2$ and $\tilde{M}(k_z) = M - B_1 k_z^2$. $\tilde{H}_0$ in Eqs. (8) and (32) are identical, with the parameters A, B, C, D, and M in Eq. (8) replaced by A_1, B_1, C, D_1, and M in Eq. (32). Therefore, the surface state at $k_x = k_y = 0$ is determined by the same equation as that for the QSH edge states. A surface-state solution exists for $M/B_1 > 0$. In the same way as in the 2D case, the surface state has a helicity determined by the sign of A_1/B_1. (Here and below we always consider the case with $B_1 B_2 > 0$, $A_1 A_2 > 0$.)

In analogy to the 2D QSH case, the surface effective model can be obtained by projecting the bulk Hamiltonian onto the surface states. To the leading order in k_x, k_y, the effective surface Hamiltonian H_{surf} has the following matrix form (H. Zhang *et al.*, 2009; Liu, Qi *et al.*, 2010):

$$H_{\text{surf}}(k_x, k_y) = C + A_2(\sigma^x k_y - \sigma^y k_x). \tag{34}$$

Higher-order terms such as k^3 terms break the axial symmetry around the z axis down to a three fold rotation symmetry, which has been studied (Fu, 2009; Liu, Qi *et al.*, 2010). For $A_2 = 4.1$ eV Å, the velocity of the surface states is given by $v = A_2/\hbar \simeq 6.2 \times 10^5$ m/s, which agrees reasonably with *ab initio* results (see Fig. 20) $v \simeq 5.0 \times 10^5$ m/s.

To understand the physical properties of the surface states, we need to analyze the form of the spin operators in this system. By using the wave function from *ab initio* calculations and projecting the spin operators onto the subspace spanned by the four basis states, we obtain the spin operators for our model Hamiltonian, with matrix elements between surface states given by $\langle \Psi_\alpha | S_x | \Psi_\beta \rangle = S_{x0} \sigma_x^{\alpha\beta}$, $\langle \Psi_\alpha | S_y | \Psi_\beta \rangle = S_{y0} \sigma_y^{\alpha\beta}$, and $\langle \Psi_\alpha | S_z | \Psi_\beta \rangle = S_{z0} \sigma_z^{\alpha\beta}$, with $S_{x(y,z)0}$ some positive constants. Therefore, we see that the Pauli $\boldsymbol{\sigma}$ matrix in the model Hamiltonian (34) is proportional to the physical spin. As discussed, the spin direction is determined by the sign of the parameter A_1/B_1, which depends on material properties such as the atomic SOC. In the Bi_2Se_3 family of materials, the upper Dirac cone has a left-handed helicity when looking from above the surface [see Figs. 20(e) and 20(f)].

From the discussion above, we see that the surface state is described by a 2D massless Dirac Hamiltonian (34). Another well-known system with a similar property is graphene, a single sheet of graphite (Castro Neto *et al.*, 2009). However, there is a key difference between the surface-state theory for 3D topological insulators and graphene or any 2D Dirac system, which is the number of Dirac cones. Graphene has four Dirac cones at low energies, due to spin and valley

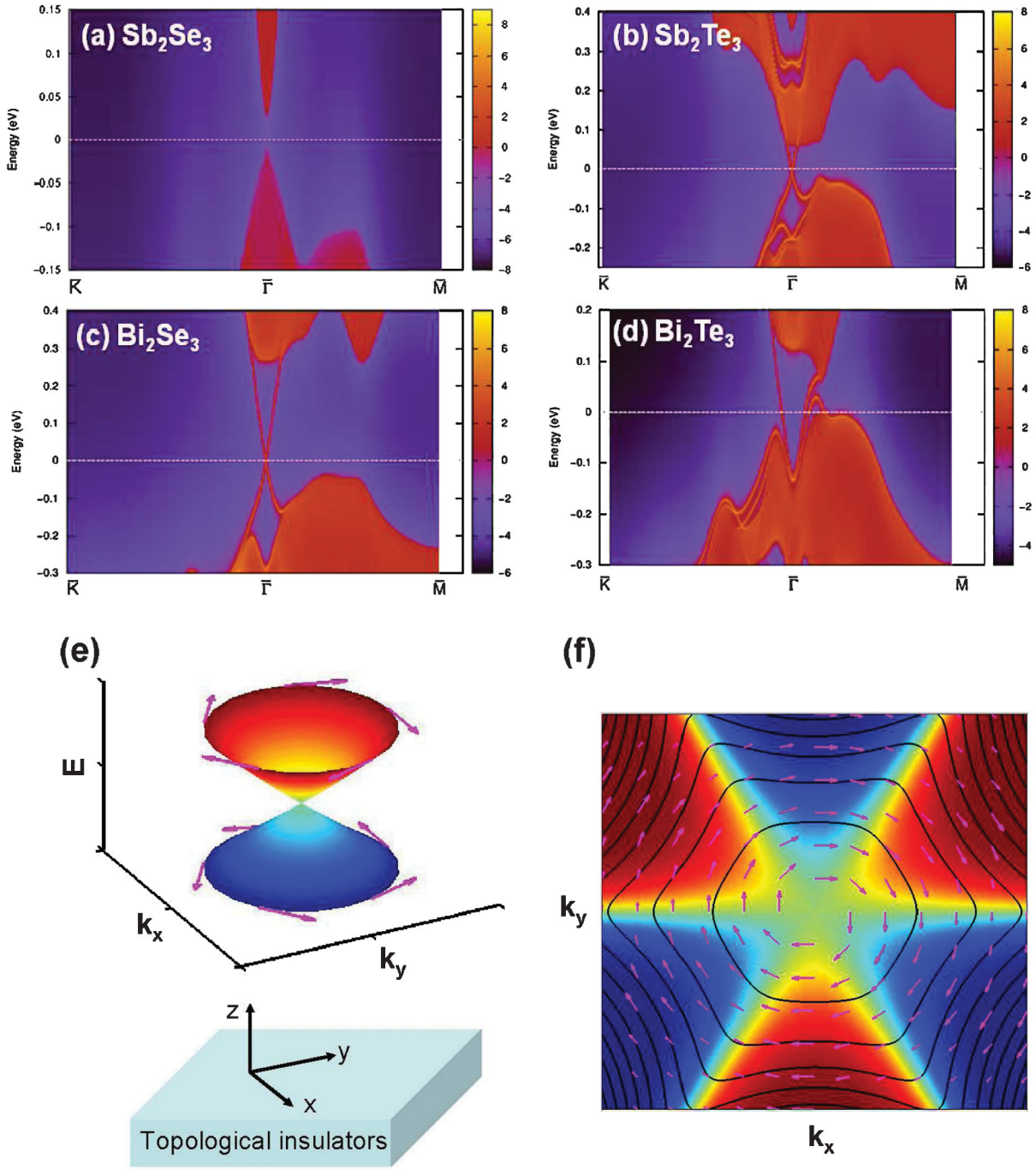

FIG. 20 (color). (a)–(d) Energy and momentum dependence of the local density of states for the Bi_2Se_3 family of materials on the [111] surface. A warmer color represents a higher local density of states. Red regions indicate bulk energy bands and blue regions indicate a bulk energy gap. The surface states can be clearly seen around the Γ point as red lines dispersing inside the bulk gap. (e), (f) Spin polarization of the surface states on the top surface. The z direction in (e) is the surface normal, pointing outward. (f) is a top view of the surface state spin texture, with the arrows representing the x-y planar spin polarization and the color indicates the z component of the spin polarization. The black line gives the constant energy contours. Adapted from H. Zhang *et al.*, 2009, and Liu, Qi *et al.*, 2010.

degeneracy. The valley degeneracy occurs because the Dirac cones are not in the vicinity of $\mathbf{k} = 0$ but rather near the two Brillouin zone corners K and $\bar{K}$. This is generic for a purely 2D system: only an even number of Dirac cones can exist in a TR invariant system. In other words, a single 2D Dirac cone without TR symmetry breaking can exist only on the surface of a topological insulator, which is also an alternate way to understand its topological robustness. As long as TR symmetry is preserved, the surface state cannot be gapped out because no purely 2D system can provide a single Dirac cone. Such a surface state is a "holographic metal" which is 2D but determined by the 3D bulk topological property.

In this section, we discussed the surface states of an insulator surrounded by vacuum. This formalism can be straightforwardly generalized to the interface states between two insulators (Volkov and Pankratov, 1985; Fradkin *et al.*, 1986; Pankratov *et al.*, 1987; Pankratov, 1990). In these pioneering works, the interface states between PbTe and

SnTe and between HgTe and CdTe were investigated. The surface states of topological insulators are also similar to the domain wall fermions of lattice gauge theory (Kaplan, 1992). In fact, domain wall fermions are precisely introduced to avoid the fermion doubling problem on the lattice, which is similar to the concept of a single Dirac cone on the surface of a topological insulator.

The helical spin texture described by the single Dirac cone equation (34) leads to a general relation between charge current density $\mathbf{j}(\mathbf{x})$ and spin density $\mathbf{S}(\mathbf{x})$ on the surface of the topological insulator (Raghu *et al.*, 2010)

$$\mathbf{j}(\mathbf{x}) = v[\psi^\dagger(\mathbf{x})\boldsymbol{\sigma}\psi(\mathbf{x}) \times \hat{\mathbf{z}}] = v\mathbf{S}(\mathbf{x}) \times \hat{\mathbf{z}}. \quad (35)$$

In particular, the plasmon mode on the surface generally carries spin (Burkov and Hawthorn, 2010; Raghu *et al.*, 2010).

C. Crossover from three dimensions to two dimensions

From the discussion above, one can see that the models describing 2D and 3D topological insulators are quite similar. Both systems are described by lattice Dirac-type Hamiltonians. In particular, when inversion symmetry is present, the topologically nontrivial phase in both models is characterized by a band inversion between two states of opposite parity. Therefore, it is natural to study the relation between these two topological states of matter. One natural question is whether a thin film of 3D topological insulator, viewed as a 2D system, is a trivial insulator or a QSH insulator. Besides theoretical interest, this problem is also relevant to experiments, especially in the Bi_2Se_3 family of materials. Indeed, these materials are layered and can be easily grown as thin films either by MBE (G. Zhang *et al.*, 2009; H. D. Li *et al.*, 2010; Y.-Y. Li *et al.*, 2010), catalyst-free vapor-solid growth (Kong, Dang *et al.*, 2010), or by mechanical exfoliation (Hong *et al.*, 2010; Shahil *et al.*, 2010; Teweldebrhan *et al.*, 2010a). Several theoretical works studied thin films of the Bi_2Se_3 family of topological insulators (Linder *et al.*, 2009; Lu *et al.*, 2010; Shan *et al.*, 2010; Liu, Zhang *et al.*, 2010; He *et al.*, 2011). Interestingly, thin films of proper thicknesses are predicted to form a QSH insulator (Lu *et al.*, 2010; Liu, Zhang *et al.*, 2010), which may constitute an approach for simpler realizations of the 2D QSH effect.

Such a crossover from 3D to 2D topological insulators can be studied from two points of view, either from the bulk states of the 3D topological insulator or from the surface states. We first consider the bulk states. A thin film of 3D topological insulator is described by restricting the bulk model (31) to a QW with thickness d, outside which there is an infinite barrier describing the vacuum. To establish the connection between the 2D BHZ model (2) and the 3D topological insulator model (31), we start from the special case $A_1 = 0$ and consider a finite A_1 later on. For $A_1 = 0$ and $k_x = k_y = 0$, the Hamiltonian (31) becomes diagonal and the Schrödinger equation for the infinite QW can be easily solved. The Hamiltonian eigenstates are simply given by $|E_n(H_n)\rangle = \sqrt{(2/d)}\sin(n\pi z/d + n\pi/2)|\Lambda\rangle$, with $|\Lambda\rangle = |P1_z^+, \uparrow(\downarrow)\rangle$ for electron subbands and $|\Lambda\rangle = |P2_z^-, \uparrow(\downarrow)\rangle$ for hole subbands. The corresponding energy spectrum is

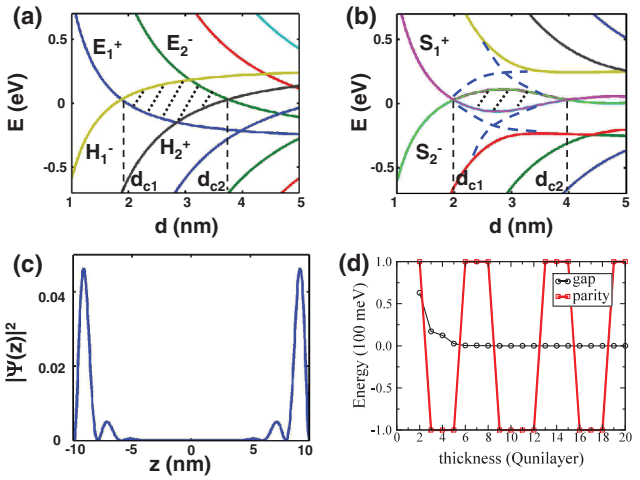

FIG. 21 (color). Energy levels vs quantum well thickness for (a) $A_1 = 0$ eV Å, and (b) $A_1 = 1.1$ eV Å. Other parameters are from H. Zhang *et al.*, 2009. Shaded regions indicate the QSH regime. The blue dashed line in (b) shows how the crossing between $|E_1(H_1)\rangle$ and $|H_2(E_2)\rangle$ evolves into an anticrossing when $A_1 \neq 0$. (c) Probability density in the state $|S_1^+\rangle$ (same for $|S_2^-\rangle$) for $A_1 = 1.1$ eV Å and $d = 20$ nm. (d) Band gap and total parity from *ab initio* calculations on Bi_2Se_3, plotted as a function of the number of quintuple layers. From Liu, Zhang *et al.*, 2010.

$E_e(n) = C + M + (D_1 - B_1)(n\pi/d)^2$ and $E_h(n) = C - M + (D_1 + B_1)(n\pi/d)^2$, respectively. We assume $M < 0$ and $B_1 < 0$ so that the system stays in the inverted regime. The energy spectrum is shown in Fig. 21(a). When the width d is small enough, electron subbands E_n have a higher energy than the hole subbands H_n due to quantum confinement effects. Because the bulk bands are inverted at the Γ point ($M < 0$), the energy of the electron subbands will decrease with increasing d toward their bulk value $M < 0$, while the energy of the hole subbands will increase toward $-M > 0$. Therefore, a crossing point must exist between the electron and hole subbands.

When a finite A_1 is turned on, the electron and hole bands are hybridized so that some of the crossings between the QW levels are avoided. However, as shown in Fig. 21(b), some level crossings cannot be lifted, which is a consequence of inversion symmetry. When the band index n is increased, the parity of the wave functions alternates for both electron and hole subbands. Moreover, the atomic orbitals forming electron and hole bands are $|P1_z^+, \uparrow(\downarrow)\rangle$ and $|P2_z^-, \uparrow(\downarrow)\rangle$, respectively, which have opposite parity. Consequently, $|E_n\rangle$ and $|H_n\rangle$ with the same index n have opposite parity, so that their crossing cannot be avoided by the A_1 term. When a finite k_x, k_y is considered, each level becomes a QW subband. The bottom of the lowest conduction band and the top of the highest valence band are indicated by S_1^+ and S_2^- in Fig. 21(b). Since these two bands have opposite parity, each level crossing between them is a topological phase transition between trivial and QSH insulator phases (Bernevig *et al.*, 2006; Fu and Kane, 2007). Since the system must be trivial in the limit $d \to 0$, we know that the first QSH insulator phase occurs between the first and second level crossings. In the $A_1 \to 0$ limit, the crossing positions are given by the critical

well thicknesses $d_{cn} = n\pi\sqrt{B_1/|M|}$. In principle, there is an infinite number of QSH phases between $d_{c,2n-1}$ and $d_{c,2n}$. However, as seen in Fig. 21(b), the gap between $|S_1^+\rangle$ and $|S_2^-\rangle$ decays quickly for large d. In the 3D limit $d \to \infty$, the two states become degenerate and actually form the top and bottom surface states of the bulk crystal [see Fig. 21(c)].

This relation between the QW valence and conduction bands and the surface states in the $d \to \infty$ limit suggests an alternate way to understand the crossover from 3D to 2D, i.e., from the surface states. In the 3D limit the two surfaces are decoupled and are the only low-energy states. The top surface is described by the effective Hamiltonian (34) while the bottom surface is obtained from the top surface by inversion. Therefore, the complete effective Hamiltonian is given by

$$H_{\text{surf}}(k_x, k_y) = A_2 \begin{pmatrix} 0 & ik_- & 0 & 0 \\ -ik_+ & 0 & 0 & 0 \\ 0 & 0 & 0 & -ik_- \\ 0 & 0 & ik_+ & 0 \end{pmatrix}.$$

When a slab of finite thickness is considered, the two surface states start overlapping, such that off-diagonal terms are introduced in the effective Hamiltonian. An effective Hamiltonian consistent with inversion and TR symmetry and incorporating intersurface tunneling is given by

$$H_{\text{surf}}(k_x, k_y) = A_2 \begin{pmatrix} 0 & ik_- & M_{2D} & 0 \\ -ik_+ & 0 & 0 & M_{2D} \\ M_{2D} & 0 & 0 & -ik_- \\ 0 & M_{2D} & ik_+ & 0 \end{pmatrix}, \quad (36)$$

where M_{2D} is a TR invariant mass term due to intersurface tunneling, which generally depends on the in-plane momentum. Equation (36) is unitarily equivalent to the BHZ Hamiltonian (2) for HgTe QWs. Whether the Hamiltonian corresponds to a trivial or QSH insulator cannot be determined without studying the behavior of this model at large momenta. Indeed, we are missing a regularization term which would play the role of the quadratic term Bk^2 in the BHZ model (see Sec. II.A). However, the transitions between trivial and nontrivial phases are accompanied by a sign change in M_{2D}, independent of the regularization scheme at high momenta. Upon variation of d, the sign of the intersurface coupling M_{2D} oscillates because the surface-state wave functions oscillate [see Fig. 21(b)]. Therefore, we reach the same conclusions as in the bulk approach.

The results above obtained from calculations using an effective model are also confirmed by first-principle calculations. The parity eigenvalues of occupied bands have been calculated as a function of the thickness of the 3D topological insulator film (Liu, Zhang *et al.*, 2010), from which the topological nature of the film can be inferred. The result is shown in Fig. 21(d), which confirms the oscillations found in the effective model. The first nontrivial phase appears at a thickness of three quintuple layers, i.e., about 3 nm for Bi_2Se_3.

D. Electromagnetic properties

In previous sections, we reviewed bulk and surface properties of 3D topological insulators, as well as their relation to 2D topological insulators (QSH insulators), based on a microscopic model. From the effective model of surface states, one can understand their robustness protected by TR symmetry. However, similar to the quantized Hall response in QH systems, the topological structure in topological insulators should not only lead to robust gapless surface states, but also to unique, quantized electromagnetic response coefficients. The quantized electromagnetic response of 3D topological insulators turns out to be a TME (Qi, Hughes, and Zhang, 2008b; Qi *et al.*, 2009), which occurs when TR symmetry is broken on the surface, but not in the bulk. The TME effect is a generic property of 3D topological insulators, which can be obtained theoretically from generic models and from an effective field theory approach (Fu and Kane, 2007; Qi, Hughes, and Zhang, 2008b; Essin *et al.*, 2009), independently of microscopic details. However, in order to develop a physical intuition for the TME effect, in this section we review this effect and its physical consequences based on the simplest surface effective model and postpone a discussion in the framework of a general effective theory to Sec. IV. We also discuss various experimental manifestations of the TME effect.

1. Half-quantum Hall effect on the surface

We start by analyzing generic perturbations to the effective surface-state Hamiltonian (34). The only momentum-independent perturbation one can add is $H_1 = \sum_{a=x,y,z} m_a \sigma^a$, and the perturbed Hamiltonian has the spectrum $E_{\mathbf{k}} = \pm\sqrt{(A_2 k_y + m_x)^2 + (A_2 k_x - m_y)^2 + m_z^2}$. Thus, the only parameter that can open a gap and destabilize the surface states is m_z, and we consider only this perturbation in the following. The mass term $m_z\sigma^z$ is odd under TR, as expected from the topological stability of surface states protected by TR symmetry. By comparison, if the surface states consist of an even number of Dirac cones, one can check that a TR invariant mass term is indeed possible. For example, if there are two identical Dirac cones, an imaginary coupling between the cones can be introduced, which leads to the gapped TR invariant Hamiltonian

$$H'_{\text{surf}}(\mathbf{k}) = \begin{pmatrix} A_2(\sigma^x k_y - \sigma^y k_x) & -im\sigma^z \\ im\sigma^z & A_2(\sigma^x k_y - \sigma^y k_x) \end{pmatrix}.$$

From such a difference between an even and an odd number of Dirac cones, one sees that the stability of the surface theory (34) is protected by a $\mathbb{Z}_2$ topological invariant.

Although the surface state with a single Dirac cone does not remain gapless when a TR breaking mass term $m_z\sigma^z$ is added, an important physical property is induced by such a mass term: a half-integer quantized Hall conductance. As discussed in Sec. II.E, the Hall conductance of a generic two-band Hamiltonian $h(\mathbf{k}) = d_a(\mathbf{k})\sigma^a$ is determined by Eq. (29), which is the winding number of the unit vector $\hat{\mathbf{d}}(\mathbf{k}) = \mathbf{d}(\mathbf{k})/|\mathbf{d}(\mathbf{k})|$ on the Brillouin zone. The perturbed surface-state Hamiltonian,

$$H_{\text{surf}}(\mathbf{k}) = A_2\sigma^x k_y - A_2\sigma^y k_x + m_z\sigma^z, \tag{37}$$

corresponds to a vector $\mathbf{d}(\mathbf{k}) = (A_2 k_y, -A_2 k_x, m_z)$. At $\mathbf{k} = 0$, the unit vector $\hat{\mathbf{d}}(\mathbf{k}) = (0, 0, m_z/|m_z|)$ points toward the north (south) pole of the unit sphere for $m_z > 0$ ($m_z < 0$). For $|\mathbf{k}| \gg |m_z|/A_2$, the unit vector $\hat{\mathbf{d}}(\mathbf{k}) \simeq A_2(k_y, -k_x, 0)/|\mathbf{k}|$ almost lies in the equatorial plane of the unit sphere. From such a "meron" configuration one sees that $\hat{\mathbf{d}}(\mathbf{k})$ covers half of the unit sphere, which leads to a winding number $\pm 1/2$ and corresponds to a Hall conductance

$$\sigma_H = \frac{m_z}{|m_z|}\frac{e^2}{2h}. \tag{38}$$

From this formula, it can be seen that the Hall conductance remains finite even in the limit $m_z \to 0$, and has a jump at $m_z = 0$. As a property of the massive Dirac model, such a half Hall conductance has been studied a long time ago in high-energy physics. In that context, the effect is termed the "parity anomaly" (Redlich, 1984b; Semenoff, 1984), because the massless theory preserves parity (and TR) but an infinitesimal mass term necessarily breaks these symmetries.

The analysis above only applies if the continuum effective model (34) applies, i.e., if the characteristic momentum $|m_z|/A_2$ is much smaller than the size of the Brillouin zone $2\pi/a$ with a the lattice constant. Since deviations from this Dirac-type effective model at large momenta are not included in the above calculation of the Hall conductance (Fu and Kane, 2007; D.-H. Lee, 2009), one cannot unambiguously predict the Hall conductance of the surface. In fact, if the effective theory describes a 2D system rather than the surface of a 3D system, additional contributions from large-momentum corrections to the effective model are necessary, since the Hall conductance of any gapped 2D band insulator must be quantized in *integer* units of e^2/h (Thouless *et al.*, 1982). For example, the QAH insulator [Eq. (28)] with mass term $M \to 0$ is also described by the same effective theory as Eq. (37), but has Hall conductance 0 or 1 rather than $\pm 1/2$ (Fradkin *et al.*, 1986).

Interestingly, the surface of a 3D topological insulator is different from all 2D insulators, in the sense that such contributions from large momenta vanish due to the requirement of TR symmetry (Qi, Hughes, and Zhang, 2008). This fact is discussed more rigorously in Sec. IV based on the general effective field theory. Here we present an argument based on the bulk to surface relationship. To understand this, consider the jump in Hall conductance at $m_z = 0$. Although deviations from the Dirac effective model at large momenta may lead to corrections to the Hall conductance for a given m_z, the change in Hall conductance $\Delta\sigma_H = \sigma_H(m_z \to 0^+) - \sigma_H(m_z \to 0^-) = (m_z/|m_z|)e^2/h$ is independent of the large-momentum contributions. Indeed, the effect of the mass term $m_z\sigma^z$ on the large-momentum sector of the theory is negligible as long as $m_z \to 0$. Therefore, any contributions to σ_H from large momenta should be continuous functions of m_z and thus cannot affect the value of the discontinuity $\Delta\sigma_H$. On the other hand, since the surface theory with $m_z = 0$ is TR invariant, TR transforms the system with mass m_z to that with mass $-m_z$. Consequently, from TR symmetry we have

$$\sigma_H(m_z \to 0^+) = -\sigma_H(m_z \to 0^-).$$

Together with the condition $\Delta\sigma_H = (m_z/|m_z|)e^2/h$, we see that the half Hall conductance given by Eq. (38) is robust, and the contribution from large-momentum corrections must vanish. By comparison, in a 2D QAH Hamiltonian discussed in Sec. II.E, i.e., the upper 2×2 block of Eq. (2), the Hamiltonian with mass M is not the TR conjugate of that with mass $-M$, and the above argument does not apply. Therefore, the half Hall conductance is a unique property of the surface states of 3D topological insulators which is determined by the bulk topology. This property distinguishes the surface states of 3D topological insulators from all pure 2D systems or topologically trivial surface states.

The analysis above has considered only translationally invariant perturbations to the surface states, but the conclusions remain robust when disorder is considered. A 2D metal without SOC belongs to the orthogonal or unitary symmetry classes of random Hamiltonians, the eigenfunctions of which are always localized when random disorder is introduced. This effect is known as Anderson localization (Abrahams *et al.*, 1979). Anderson localization is a quantum interference effect induced by constructive interference between different backscattering paths. By comparison, a system with TR invariance and SOC belongs to the symplectic class, where the constructive interference becomes destructive. In that case, the system has a metallic phase at weak disorder, which turns into an insulator phase by going through a metal-insulator transition at a certain disorder strength (Hikami *et al.*, 1980; Evers and Mirlin, 2008). Naively, one expects the surface state with nonmagnetic disorder to be in the symplectic class. However, Nomura, Koshino, and Ryu (2007) showed that the surface state is metallic even for an arbitrary impurity strength, which is consistent with the topological robustness of the surface state.

On the contrary, with TR symmetry-breaking disorder, the system belongs to the unitary class, which exhibits localization for arbitrarily weak disorder strength. While the longitudinal resistivity flows to infinity due to localization, the Hall conductivity flows to the quantized value $\pm e^2/2h$ (Nomura *et al.*, 2008). Therefore, the system enters a half-QH phase once an infinitesimal TR symmetry-breaking perturbation is introduced, independently of the detailed form of the TR breaking perturbation. Physically, TR breaking disorder is induced by magnetic impurities, the spin of which not only contributes a random TR breaking field, but also has its own dynamics. For example, the simplest exchange interaction between impurity spin and surface state can be written as $H_{\text{int}} = \sum_i J_i \mathbf{S}_i \cdot \psi^\dagger \boldsymbol{\sigma} \psi(\mathbf{R}_i)$, with $\mathbf{S}_i$ the impurity spin, $\psi^\dagger \boldsymbol{\sigma} \psi(\mathbf{R}_i)$ the spin density of surface electrons at the impurity position $\mathbf{R}_i$, and J_i the exchange coupling. To understand the physical properties of the topological insulator surface in the presence of magnetic impurities, it is instructive to study the interaction between impurity spins mediated by the surface electrons (Liu *et al.*, 2009). As in a usual Fermi liquid, if the surface state has a finite Fermi wave vector k_F, a Ruderman-Kittel-Kasuya-Yosida interaction between the impurity spins is introduced, the sign of which oscillates with wavelength $\propto \frac{1}{2}k_F$ (Liu *et al.*, 2009; Ye *et al.*, 2010). If the Fermi level is close to the Dirac point, i.e., $k_F \to 0$, the sign of the Ruderman-Kittel-Kasuya-Yosida interaction does not oscillate but is uniform. The sign of the resulting uniform

spin-spin interaction is determined by the coupling to the surface electrons, which turns out to be ferromagnetic. Physically, the interaction is ferromagnetic rather than antiferromagnetic, because a uniform spin polarization can maximize the gap opened on the surface, which is energetically favorable. Because of this ferromagnetic spin-spin interaction, the system can order ferromagnetically when the chemical potential is near the Dirac point (Liu *et al.*, 2009). This mechanism is of practical importance, because it provides a way to generate a surface TR symmetry-breaking field by coating the surface with magnetic impurities and tuning the chemical potential near the Dirac point (Cha *et al.*, 2010; Chen and Wan, 2010; Feng *et al.*, 2010; Tran and Kim, 2010; Žitko, 2010).

2. Topological magnetoelectric effect

As discussed, the surface half-QH effect is a unique property of a TR symmetry-breaking surface and is determined by the bulk topology, independently of details of the surface TR symmetry-breaking perturbation. A key difference between the surface half-QH effect and the usual integer QH effect is that the former cannot be measured by a dc transport experiment. An integer QH system has chiral edge states which contribute to the quantized Hall current while being connected to leads. However, it is a simple mathematical fact that the surface of a finite sample of 3D topological insulator is always a closed manifold without an edge. If the whole surface of a topological insulator sample is gapped by magnetic impurities, there are no edge states to carry a dc transport current. If the magnetic impurities form a ferromagnetic phase and there is a domain wall in the magnetic moment, the Hall conductance has a jump at the domain wall due to Eq. (38). In this case, the jump of Hall conductance is e^2/h across the domain wall, so that a chiral gapless edge state propagates along the domain wall [see Fig. 22(a)] (Qi, Hughes, and Zhang, 2008). This mechanism provides another route toward the QAH effect without any external magnetic field and the associated LLs. This is very much like the boundary between two ordinary QH states with Hall conductance ne^2/h and $(n+1)e^2/h$. The wave function for an edge state along a straight domain wall can also be solved for analytically following the same procedure as that used in Sec. II.B. Interestingly, if one attaches voltage and current

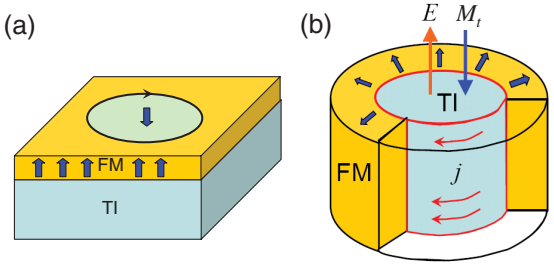

FIG. 22 (color). (a) Ferromagnetic layer on the surface of the topological insulator with a magnetic domain wall, along which a chiral edge state propagates. (b) Relation between surface half-QH effect and bulk topological magnetoelectric effect. A magnetization is induced by an electric field due to the surface Hall current. From Qi, Hughes, and Zhang, 2008b.

leads to the domain wall in the same way as for an ordinary Hall bar, one should observe a Hall conductance of e^2/h rather than $e^2/2h$, since the domain wall chiral state behaves in the same way as the edge state of a $\sigma_H = e^2/h$ QH system. Thus again we see that from dc transport measurements, one cannot observe the half Hall conductance.

Such a difference between integer QH effect and surface half-QH effect indicates that the surface half-QH effect is actually a new topological phenomenon which, in terms of its observable consequences, is qualitatively different from the usual integer QH effect. Alternatively, the proper detection of this new topological phenomenon actually probes a unique electromagnetic response property of the bulk, the TME (Qi, Hughes, and Zhang, 2008; Essin *et al.*, 2009). A magnetoelectric effect is defined as a magnetization induced by an electric field, or alternatively, a charge polarization induced by a magnetic field. To understand the relation between the surface half-QH effect and the magnetoelectric effect, consider the configuration shown in Fig. 22(b), where the side surface of a 3D topological insulator is covered by magnetic impurities with ferromagnetic order, so that the surface is gapped and exhibits a half quantized Hall conductance. When an electric field $\mathbf{E}$ is applied parallel to the surface, a Hall current $\mathbf{j}$ is induced [Eq. (39)], which circulates along the surface. This surface current perpendicular to $\mathbf{E}$ will then induce a magnetic field parallel to $\mathbf{E}$, so that the system exhibits a magnetoelectric response. The Hall response equation is written as

$$\mathbf{j} = \frac{m}{|m|}\frac{e^2}{2h}\hat{\mathbf{n}} \times \mathbf{E}, \tag{39}$$

with $\hat{\mathbf{n}}$ a unit vector normal to the surface, and the sign of the mass $m/|m|$ is determined by the direction of the surface magnetization. Such a Hall response is equivalent to a magnetization proportional to the electric field

$$\mathbf{M}_t = -\frac{m}{|m|}\frac{e^2}{2hc}\mathbf{E}.$$

This magnetization is a topological response to the electric field and is independent of the details of the system. Similarly, a topological contribution to the charge polarization can be induced by a magnetic field. The complete electromagnetic response of the system is described by the following modified constituent equations:

$$\begin{aligned}\mathbf{H} &= \mathbf{B} - 4\pi\mathbf{M} + 2P_3\alpha\mathbf{E},\\ \mathbf{D} &= \mathbf{E} + 4\pi\mathbf{P} - 2P_3\alpha\mathbf{B},\end{aligned} \tag{40}$$

with $\alpha = e^2/\hbar c$ the fine structure constant, and $P_3 \equiv m/2|m| = \pm 1/2$ the quantum of Hall conductance. A detailed explanation of the coefficient P_3 and the effective field theory description of the TME effect is discussed in Sec. IV. In this section we focus on the physical consequences of the TME effect. We simply note the fact that, more generally, for topological insulators P_3 can take the value $n + 1/2$ with arbitrary integer n, since the number of Dirac cones on the surface can be any odd integer.

3. Image magnetic monopole effect

One of the most direct consequences of the TME effect is the image magnetic monopole effect (Qi *et al.*, 2009). Consider bringing an electric charge into proximity with an ordinary 3D insulator. The electric charge will polarize the dielectric, which can be described by the appearance of an image electric charge inside the insulator. If the same thing is done with a topological insulator, of which the surface states have been gapped by TR symmetry breaking, in addition to the image electric charge an image magnetic monopole will also appear inside the insulator.

This image magnetic monopole effect can be studied straightforwardly by solving Maxwell's equations with the modified constituent equations (40), in the same way as the image charge problem in an ordinary insulator. Consider the geometry shown in Fig. 23 (left panel). The lower half-space $z<0$ is occupied by a topological insulator with dielectric constant ϵ_2 and magnetic permeability μ_2, while the upper half-space $z>0$ is occupied by a conventional insulator with dielectric constant ϵ_1 and magnetic permeability μ_1. An electric point charge q is located at $(0, 0, d)$ with $d>0$. We assume that the surface states are gapped by some local TR symmetry-breaking field m, so that the surface half-QH effect and TME exist. The boundary of the topological insulator acts as a domain wall where P_3 jumps from $1/2$ to 0. In this semi-infinite geometry, an image point magnetic monopole with flux g_2 is located at the mirror position $(0, 0, -d)$, together with an image electric point charge q_2. Physically, the magnetic field of such an image monopole

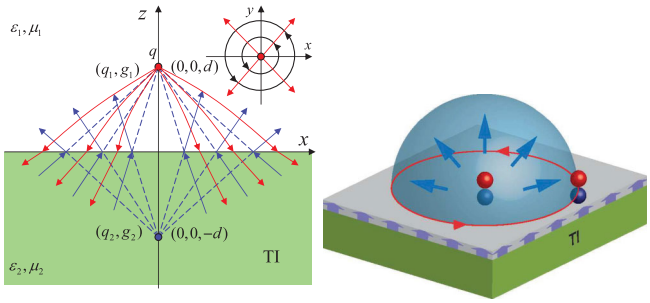

FIG. 23 (color). (Left panel) Image electric charge and image magnetic monopole due to an external electric point charge. The lower half-space is occupied by a topological insulator (TI) with dielectric constant ϵ_2 and magnetic permeability μ_2. The upper half-space is occupied by a topologically trivial insulator (e.g., vacuum) with dielectric constant ϵ_1 and magnetic permeability μ_1. An electric point charge q is located at $(0, 0, d)$. Seen from the lower half-space, the image electric charge q_1 and magnetic monopole g_1 are at $(0, 0, d)$. Seen from the upper half-space, the image electric charge q_2 and magnetic monopole g_2 are at $(0, 0, -d)$. The red (blue) solid lines represent the electric (magnetic) field lines. The inset is a top-down view showing the in-plane component of the electric field on the surface (red arrows) and the circulating surface current (black circles). (Right panel) Illustration of the fractional statistics induced by the image monopole effect. Each electron forms a "dyon" with its image monopole. When two electrons are exchanged, an Aharonov-Bohm phase factor is obtained, which is determined by half of the image monopole flux, independent of the exchange path, leading to the phenomenon of statistical transmutation. From Qi *et al.*, 2009.

configuration is induced by circulating Hall currents on the surface, which are induced by the electric field of the external charge. A similar effect has been studied in the integer QH effect (Haldane and Chen, 1984). Conversely, the electromagnetic field strength inside the topological insulator is described by an image magnetic monopole g_1 and electric charge q_1 in the upper half-space, at the same point as the external charge. The image magnetic monopole flux and image electric charge (q_1, g_1) and (q_2, g_2) are given by

$$q_1 = q_2 = \frac{1}{\epsilon_1}\frac{(\epsilon_1-\epsilon_2)(1/\mu_1+1/\mu_2)-4\alpha^2P_3^2}{(\epsilon_1+\epsilon_2)(1/\mu_1+1/\mu_2)+4\alpha^2P_3^2}q,$$
$$g_1 = -g_2 = -\frac{4\alpha P_3}{(\epsilon_1+\epsilon_2)(1/\mu_1+1/\mu_2)+4\alpha^2P_3^2}q. \tag{41}$$

Interestingly, by making use of electric-magnetic duality these expressions can be simplified to more compact forms (Karch, 2009). It is worth pointing out that a similar effect can also occur in other systems with magnetoelectric effect, such as multiferroic insulators. However, as discussed, for three-dimensional insulators with TR invariance in the bulk, the TME effect with a quantized value of P_3 and thus the image monopole effect are unique signatures of 3D topological insulators.

Moreover, interesting phenomena appear when we consider the dynamics of the external charge. For example, consider a 2D electron gas at a distance d above the surface of the 3D topological insulator. If the motion of the electron is slow enough (with respect to the time scale $\hbar/m$ corresponding to the TR symmetry-breaking gap m), the image monopole will follow the electron adiabatically, such that the electron forms an electron-monopole composite, i.e., a dyon (Witten, 1979). When two electrons wind around each other, each electron perceives the magnetic flux of the image monopole attached to the other electron, which leads to statistical transmutation. The statistical angle is determined by the electron charge and image monopole flux as

$$\theta = \frac{g_1 q}{2\hbar c} = \frac{2\alpha^2 P_3}{(\epsilon_1+\epsilon_2)(1/\mu_1+1/\mu_2)+4\alpha^2P_3^2}. \tag{42}$$

Besides the image monopole effect, other interaction terms between the surface electrons and the surface magnetism can induce additional terms in the interaction between the surface electrons. However, the statistical angle is determined by the net magnetic flux induced by each electron, which is insensitive to local perturbations such as inducing a magnetic dipole moment. The statistical angle can be modified only by modifying the long-wavelength behavior of the surface system, such as modifying ϵ and μ due to a finite surface electron density. The image monopole can be detected directly by local probes sensitive to small magnetic fields, such as scanning superconducting quantum interference devices and scanning magnetic force microscopy (Qi *et al.*, 2009). The current due to the image monopole can also be detected in principle (Zang and Nagaosa, 2010).

4. Topological Kerr and Faraday rotation

Another way to detect the TME effect is through the transmission and reflection of polarized light. When linearly

polarized light propagates through a medium which breaks TR symmetry, the plane of polarization of the transmitted light may be rotated, which is known as the Faraday effect (Landau and Lifshitz, 1984). A similar rotation may occur for light reflected by a TR symmetry-breaking surface, which is known as the magneto-optical Kerr effect (Landau and Lifshitz, 1984). Since the bulk of the topological insulator is TR invariant, no Faraday rotation will occur in the bulk. However, if TR symmetry is broken on the surface, the TME effect occurs and a unique kind of Kerr and Faraday rotation is induced on the surface. Physically, the plane of polarization of the transmitted and reflected light is rotated because the electric field $\mathbf{E}_0(\mathbf{r}, t)$ of linearly polarized light generates a magnetic field $\mathbf{B}(\mathbf{r}, t)$ in the same direction, due to the TME effect. Similarly as for the image monopole effect, the Faraday and Kerr rotation angles can be calculated by solving Maxwell's equations with the modified constituent Eqs. (40) if the energy of the photon $\hbar\omega$ is much smaller than both the bulk and surface gaps. In the simplest case of a single surface between a trivial insulator and a semi-infinite topological insulator (see Fig. 24, left panel), the rotation angle for light incident from the trivial insulator is given by (Qi, Hughes, and Zhang *et al.*, 2008b; Karch, 2009; Maciejko *et al.*, 2010; Wang-Kong Tse, 2010)

$$\tan\theta_K = \frac{4\alpha P_3\sqrt{\epsilon_1/\mu_1}}{\epsilon_2/\mu_2 - \epsilon_1/\mu_1 + 4\alpha^2 P_3^2}, \tag{43}$$

$$\tan\theta_F = \frac{2\alpha P_3}{\sqrt{\epsilon_1/\mu_1} + \sqrt{\epsilon_2/\mu_2}}, \tag{44}$$

where ϵ_1 and μ_1 are the dielectric constant and magnetic permeability of the trivial insulator, and ϵ_2 and μ_2 are those of the topological insulator.

Although the surface Faraday and Kerr rotations are induced by the topological property of the bulk and are determined by the magnetoelectric response with quantized coefficient αP_3, the rotation angle is not universal and depends on the material parameters ϵ and μ. The TME response always coexists with the ordinary electromagnetic response, which makes it difficult to observe the topological quantization phenomenon. However, recently new proposals have been made to avoid the dependence on nonuniversal material parameters (Maciejko *et al.*, 2010; Wang-Kong Tse, 2010). The key idea is to consider a slab of topological insulator of finite thickness with two surfaces, with vacuum on one side and a substrate on the other (see Fig. 24, right panel). The combination of Kerr and Faraday angles measured at *reflectivity minima* provides enough information to determine the quantized coefficient αP_3 (Maciejko *et al.*, 2010),

$$\frac{\cot\theta_F + \cot\theta_K}{1 + \cot^2\theta_F} = 2\alpha P_3, \tag{45}$$

provided that both top and bottom surfaces have the same surface Hall conductance $\sigma_H = P_3 e^2/h$. In Eq. (45), the quantized coefficient αP_3 is expressed solely in terms of the measurable Kerr and Faraday angles. This enables a direct experimental measurement of P_3 without a separate measurement of the nonuniversal optical constants ϵ and μ of the topological insulator film and the substrate. If the two surfaces have different surface Hall conductances, it is still possible to determine them separately through a measurement of the Kerr and Faraday angles at reflectivity *maxima* (Maciejko *et al.*, 2010).

The typical surface gap that can be induced by TR breaking is of the order of 10 meV, so that the experiments proposed above need to be done in THz frequency. The current experimental technique is sufficient in observing the proposed effect, and preliminary experimental efforts have started (Jenkins *et al.*, 2010).

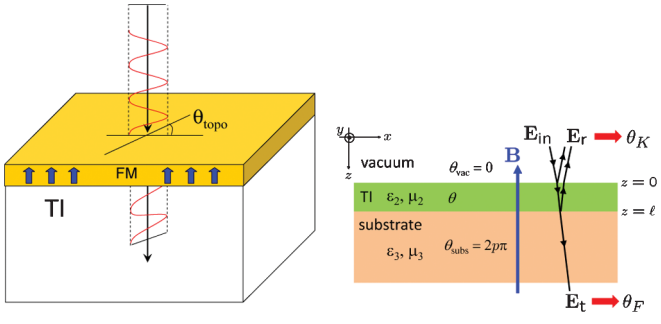

FIG. 24 (color). (Left panel) Illustration of the Faraday rotation on one surface of topological insulator. Adapted from Qi, Hughes, and Zhang, 2008b. (Right panel) A more complicated geometry with Kerr and Faraday rotation on two surfaces of the topological insulator. In this geometry, the effect of nonuniversal properties of the material can be eliminated and the quantized magnetoelectric coefficient αP_3 can be directly measured. From Maciejko *et al.*, 2010.

5. Related effects

The TME has other interesting consequences. The TME effect corresponds to a term $\theta\mathbf{E}\cdot\mathbf{B}$ in the action [see Sec. IV for more details], which mediates the transmutation between the electric field and magnetic field (Qi, Hughes, and Zhang, 2008b). In the presence of a magnetic monopole, such an electric-magnetic transmutation induces an electric field around the magnetic monopole, so that the monopole carries an electric charge (Witten, 1979) $q = e(\theta/2\pi)g/\phi_0$ with $\phi_0 = hc/e$ the flux quanta. Such a composite particle carries both magnetic flux and electric charge and is called a dyon. In principle, the topological insulator provides a physical system which can detect a magnetic monopole through this effect (Rosenberg and Franz, 2010). For a topological insulator, we have $\theta = \pi$, which corresponds to a half-charge $q = e/2$ for a monopole with unit flux. Such a half-charge corresponds to a zero energy bound state induced by the monopole. The charge of the monopole is $e/2$ when the bound state is occupied and $-e/2$ when it is unoccupied. Such a half-charge and zero mode is similar to charge fractionalization in 1D systems (Su *et al.*, 1979). If the monopole passes through a hole in the topological insulator, the charge will follow it, which corresponds to a charge pumping effect (Rosenberg *et al.*, 2010). It was recently proposed that the strength and sign of the Casimir force between two topological insulator plates can be tuned by means of external tunable parameters, due to the TME effect (Grushin and Cortijo, 2011).

All effects discussed up to this point are consequences of the TME in a topological insulator with surface TR symmetry

breaking. No effects of electron correlation have been taken into account. When the electron-electron interaction is considered, interesting new effects can occur. For example, if a topological insulator is realized by transition metal compounds with strong electron correlation effects, antiferromagnetic (AFM) long-range order may develop in this material. Since the AFM order breaks TR symmetry and inversion symmetry, the magnetoelectric coefficient P_3 defined in Eq. (40) deviates from its quantized value $n + 1/2$. Denoting the AFM Néel vector by $\mathbf{n}(\mathbf{r}, t)$, we have $P_3(\mathbf{n}) = P_3(\mathbf{n} = 0) + \delta P_3(\mathbf{n})$, where $P_3(\mathbf{n} = 0)$ is the quantized value of P_3 in the absence of AFM order. This change in the magnetoelectric coefficient has interesting consequences when spin-wave excitations are considered. Fluctuations of the Néel vector $\delta\mathbf{n}(\mathbf{r}, t)$ induce in general fluctuations of δP_3, leading to a coupling between spin waves and the electromagnetic field (R. Li *et al.*, 2010). In high-energy physics, such a particle coupled to the $\mathbf{E} \cdot \mathbf{B}$ term is called an "axion" (Peccei and Quinn, 1977; Wilczek, 2009). Physically, in a background magnetic field such an "axionic" spin wave is coupled to the electric field with a coupling constant tunable by the magnetic field. Consequently, a polariton can be formed by the hybridization of the spin wave and photon, similar to the polariton formed by optical phonons (Mills and Burstein, 1974). The polariton gap is controlled by the magnetic field, which may realize a tunable optical modulator.

Another interesting effect emerges from electron correlations when a thin film of topological insulator is considered. When the film is thick enough so that there is no direct tunneling between the surface states on the top and bottom surfaces, but not too thick so that the long-range Coulomb interaction between the two surfaces is still important, an intersurface particle-hole excitation, i.e., an exciton, can be induced (Seradjeh *et al.*, 2009). Denoting the fermion annihilation operator on the two surfaces by ψ_1, ψ_2, the exciton creation operator is $\psi_1^\dagger \psi_2$. In particular, when the two surfaces have opposite Fermi energy with respect to the Dirac point, there is nesting between the two Fermi surfaces, which leads to an instability toward exciton condensation. In the exciton condensate phase, the exciton creation operator acquires a nonzero expectation value $\langle \psi_1^\dagger \psi_2 \rangle \neq 0$, which corresponds to an effective intersurface tunneling. Interestingly, one can consider a vortex in this exciton condensate. Such a vortex corresponds to a complex spatially dependent intersurface tunneling amplitude and is equivalent to a magnetic monopole. According to the Witten effect mentioned above (Rosenberg and Franz, 2010), such a vortex of the exciton condensate carries charge $\pm e/2$, which provides a way to test the Witten effect in the absence of a real magnetic monopole.

Besides the effects discussed above, there are many other physical effects related to the TME effect, or surface half-QH effect. The magnetotransport properties of the topological surface states have been studied in various situations (Mondal *et al.*, 2010a, 2010b; Yazyev *et al.*, 2010; Yokoyama, Tanaka, and Nagaosa, 2010). The half-QH effect of the surface states induced by a magnetic layer deposited on top of the topological insulator surface can be considered as a coupling between the magnetic moment and the surface electric current (Qi, Hughes, and Zhang, 2008b). Such a coupling leads to the inverse of the half-QH effect, which means that a charge current on the surface can flip the magnetic moment of the magnetic layer (Garate and Franz, 2010; Yokoyama, Zang, and Nagaosa, 2010). Similar to such a coupling between charge current and magnetic moment, a charge density is coupled to magnetic textures such as domain walls and vortices (Nomura and Nagaosa, 2010). This effect can be used to drive magnetic textures by electric fields. These effects on a topological insulator surface coupled with magnetic layers are relevant to potential applications of topological insulators in designing new spintronic devices.

E. Experimental results

1. Material growth

There have been many interesting theoretical proposals for novel effects in topological insulators, but perhaps the most exciting aspect of the field is the rapid increase in experimental efforts focused on topological insulators. High-quality materials are being produced in several groups around the world and of all different types. Bulk materials were first grown for experiments on topological insulators in the Cava group at Princeton University including the $Bi_{1-x}Sb_x$ alloy (Hsieh *et al.*, 2008) and Bi_2Se_3, Bi_2Te_3 and Sb_2Te_3 crystals (Hsieh *et al.*, 2009b; Xia *et al.*, 2009). Crystalline samples of Bi_2Te_3 have also been grown at Stanford University in the Fisher group (Chen *et al.*, 2009). In addition to bulk samples, Bi_2Se_3 nanoribbons (Hong *et al.*, 2010; Kong, Randel *et al.*, 2010; Peng *et al.*, 2010) have been fabricated in the Cui group at Stanford University, and thin films of Bi_2Se_3 and Bi_2Te_3 have been grown by MBE by the Xue group at Tsinghua University (Y.-Y. Li *et al.*, 2010; Y. Zhang *et al.*, 2010), as well as other groups (G. Zhang *et al.*, 2009; H. D. Li *et al.*, 2010). Thin films can also be obtained by exfoliation from bulk samples (Hong *et al.*, 2010; Shahil *et al.*, 2010; Teweldebrhan *et al.*, 2010b). The stoichiometric compounds Bi_2Se_3, Bi_2Te_3, and Sb_2Te_3 are not extremely difficult to grow, which should allow more experimental groups to have access to high-quality topological insulator samples (G. Zhang *et al.*, 2009; Butch *et al.*, 2010). Because of intrinsic doping from vacancy and antisite defects, Bi_2Se_3 and Bi_2Te_3 (Chen *et al.*, 2009; Hsieh *et al.*, 2009b; Xia *et al.*, 2009) are shown to contain n-type carriers while Sb_2Te_3 (Hsieh *et al.*, 2009b) is a p type. Consequently, controllable extrinsic doping is required to tune the Fermi energy to the Dirac point of the surface states. For example, Bi_2Te_3 can be doped with Sn (Chen *et al.*, 2009) and Bi_2Se_3 can be doped with Sb (Analytis, McDonald *et al.*, 2010) or Ca (Wang *et al.*, 2010; Hor *et al.*, 2011). The tuning of the Fermi level to the Dirac point is first achieved by a combination of bulk doping and surface NO_2 doping of Bi_2Se_3 (Hsieh *et al.*, 2009a). Furthermore, it is found that doping Bi_2Se_3 with Cu can induce superconductivity (Hor *et al.*, 2010b), while Fe and Mn dopants may yield ferromagnetism (Xia *et al.*, 2008; Cha *et al.*, 2010; Chen *et al.*, 2010a; Hor *et al.*, 2010a; Wray *et al.*, 2010).

2. Angle-resolved photoemission spectroscopy

ARPES experiments are uniquely positioned to detect the topological surface states. The first experiments on

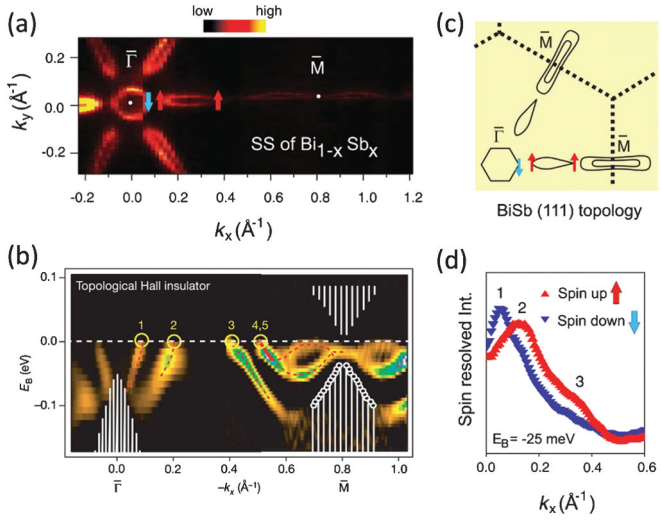

FIG. 25 (color). (a) ARPES data for the surface-state Fermi surface of $Bi_0.9Sb_0.1$. (b) The band dispersion along the $\bar{\Gamma} - \bar{M}$ direction in the surface Brillouin zone crosses the Fermi energy an odd (5) number of times, a signature of a 3D topological insulator. (c) The spin-resolved Fermi surface derived from spin-resolved ARPES spectra such as shown in (d). From Hsieh *et al.*, 2008, 2009c.

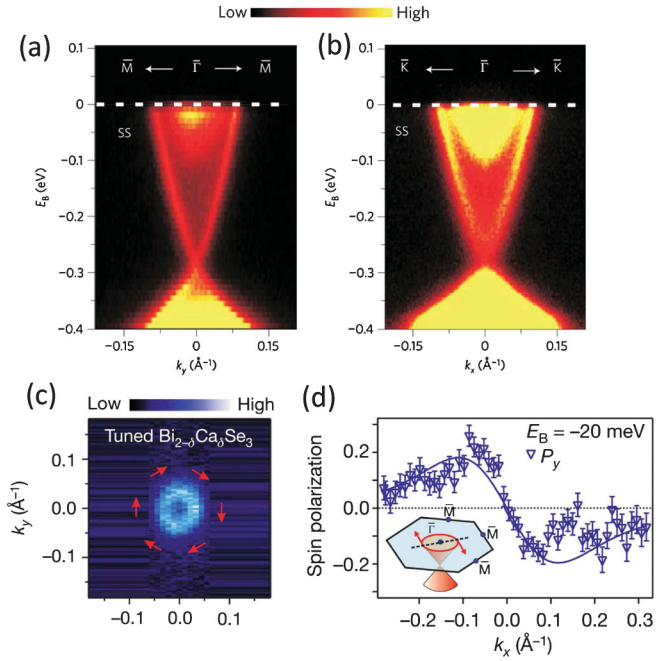

FIG. 26 (color). ARPES data for the dispersion of the surface states of Bi_2Se_3, along directions (a) $\bar{\Gamma} - \bar{M}$ and (b) $\bar{\Gamma} - \bar{K}$ in the surface Brillioun zone. Spin-resolved ARPES data are shown along $\bar{\Gamma} - \bar{M}$ for a fixed energy in (d), from which the spin polarization in momentum space (c) can be extracted. From Xia *et al.*, 2009, Hsieh *et al.*, 2009a.

topological insulators were ARPES experiments carried out on the $Bi_{1-x}Sb_x$ alloy (Hsieh *et al.*, 2008). Observation of five branches of surface states, together with the respective spin polarizations determined later by spin-resolved ARPES (Hsieh *et al.*, 2009c), confirms the nontrivial topological nature of the surface states of $Bi_{1-x}Sb_x$, as shown in Fig. 25.

ARPES work on Bi_2Se_3 (Xia *et al.*, 2009) and Bi_2Te_3 (Chen *et al.*, 2009; Hsieh *et al.*, 2009a) soon followed. Unlike the multiple branches of surface states observed for $Bi_{1-x}Sb_x$, these experiments report a remarkably simple surface-state spectrum with a single Dirac cone located at the Γ point and a large bulk band gap, in accordance with the theoretical predictions. For Bi_2Se_3, a single Dirac cone with linear dispersion is clearly shown at the $\bar{\Gamma}$ point within the band gap in Figs. 26(a) and 26(b). Figure 26(d) shows the y component of the spin polarization along the k_x ($\bar{\Gamma} - \bar{M}$) direction measured by spin-resolved ARPES (Hsieh *et al.*, 2009a). The opposite spin polarization in the y direction for opposite $\mathbf{k}$ indicates the helical nature of the spin polarization for surface states. As discussed, Bi_2Se_3 has a finite density of n-type carriers due to intrinsic doping. Therefore, the above ARPES data [Fig. 26(a) and 26(b)] show that the Fermi energy is above the conduction band bottom and the sample is, in fact, a metal rather than an insulator in the bulk. To obtain a true topological insulating state with the Fermi energy tuned into the bulk gap, careful control of external doping is required. Such control was first reported by Chen *et al.* (Fig. 27) for a sample of Bi_2Te_3 with 0.67% Sn doping (Chen *et al.*, 2009). A similar result was also realized for Bi_2Se_3 with Ca doping (Hsieh *et al.*, 2009a). Some recent work on Sb_2Te_3 (Hsieh *et al.*, 2009b) supports the theoretical prediction that this material is also a topological insulator (H. Zhang *et al.*, 2009). This family of materials is moving to the forefront of research on topological insulators due to the large bulk gap and the simplicity of the surface-state spectrum.

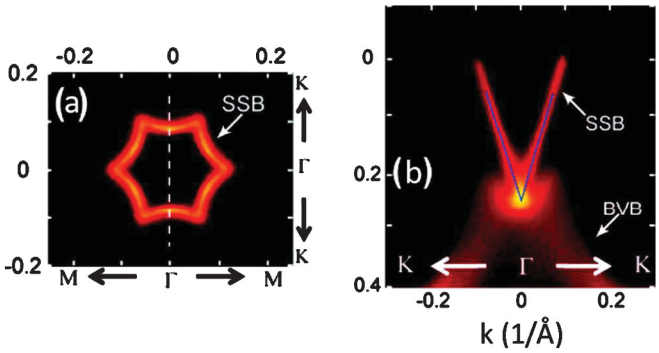

FIG. 27 (color). ARPES measurement of (a) shape of the Fermi surface and (b) band dispersion along the $K - \Gamma - K$ direction, for Bi_2Te_3 nominally doped with 0.67% Sn. From Chen *et al.*, 2009.

Although the simple model (34) captures most of the surface-state physics of these systems, experiments report a hexagonal surface-state Fermi surface (Fig. 27), while Eq. (34) describes only a circular Fermi surface sufficiently close to the Dirac point. However, such a hexagonal warping effect can easily be taken into account by including an additional term in the surface Hamiltonian which is cubic in k (Fu, 2009). The surface Hamiltonian for Bi_2Te_3 can be written as

$$H(\mathbf{k}) = E_0(\mathbf{k}) + v_{\mathbf{k}}(k_x\sigma^y - k_y\sigma^x) + \frac{\lambda}{2}(k_+^3 + k_-^3)\sigma^z, \tag{46}$$

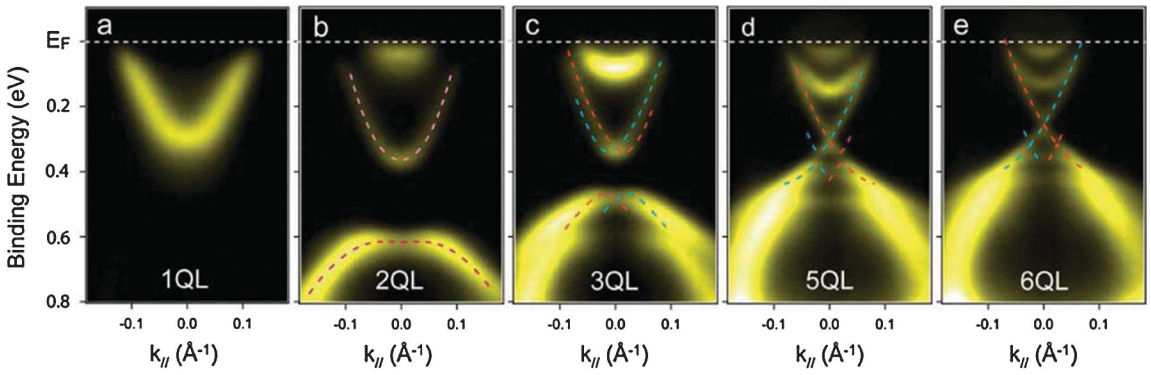

FIG. 28 (color). ARPES data for Bi_2Se_3 thin films of thickness (a) 1QL, (b) 2QL, (c) 3QL, (d) 5QL, and (e) 6QL, measured at room temperature (QL stands for quintuple layer). From Y. Zhang *et al.*, 2010.

where $E_0(\mathbf{k}) = \mathbf{k}^2/(2m^*)$ breaks the particle-hole symmetry, the Dirac velocity $v_\mathbf{k} = v(1 + \alpha\mathbf{k}^2)$ acquires a quadratic dependence on $\mathbf{k}$, and λ parametrizes the amount of hexagonal warping (Fu, 2009).

In addition to its usefulness for studying bulk crystalline samples, ARPES has also been used to characterize the thin films of Bi_2Se_3 and Bi_2Te_3 (Li *et al.*, 2010c; Sakamoto *et al.*, 2010; Y. Zhang *et al.*, 2010). The thin films were grown to initiate a study of the crossover (Liu, Zhang *et al.*, 2010) from a 3D topological insulator to a 2D QSH state (see Sec. III.C). In Fig. 28, ARPES spectra are shown for several thicknesses of a Bi_2Se_3 thin film, which show the evolution of the surface states from hybridization gaps for thin samples to vanishing gaps for thicker samples.

3. Scanning tunneling microscopy

In addition to the ARPES characterization of 3D topological insulators, scanning tunneling microscopy (STM) and scanning tunneling spectroscopy (STS) provide another kind of surface-sensitive technique to probe the topological surface states. A set of materials have been investigated in STM or STS experiments: $Bi_{1-x}Sb_x$ (Roushan *et al.*, 2009), Bi_2Te_3 (T. Zhang *et al.*, 2009; Alpichshev *et al.*, 2010), and Sb (Gomes *et al.*, 2009). (Although Sb is topologically nontrivial, it is a semimetal instead of an insulator.) The comparison between STM or STS and ARPES was first performed for Bi_2Te_3 (Alpichshev *et al.*, 2010), where it was found that the integrated density of states obtained from ARPES [Fig. 29(a)] agrees well with the differential conductance dI/dV obtained from STS measurements [Fig. 29(b)]. From such a comparison, different characteristic energies (E_F, E_A, E_B, E_C, and E_D in Fig. 29) can be easily and unambiguously identified.

Besides the linear Dirac dispersion, which has already been well established by ARPES experiments, STM or STS can provide further information about the topological nature of the surface states, such as the interference patterns of impurities or edges (Gomes *et al.*, 2009; Roushan *et al.*, 2009; T. Zhang *et al.*, 2009; Alpichshev, Analytis, Chu, Fisher, and Kapitulnik, 2010). When there are impurities on the surface of a topological insulator, the surface states will be scattered and form an interference pattern around the impurities. Fourier transforming the interference pattern into momentum space, one can quantitatively extract the scattering intensity for a fixed energy and scattering wave vector. With such information one can determine what types of scattering events are suppressed. Figures 30(a) and 30(c) show the interference pattern in momentum space for Bi_xSb_{1-x} (Roushan *et al.*, 2009) and Bi_2Te_3 (T. Zhang *et al.*, 2009), respectively. In order to analyze the interference pattern (P. Lee, 2009), we take Bi_2Te_3 as an example [Figs. 30(c) and 30(d)]. The Fermi surface of Bi_2Te_3 is shown in Fig. 30(d), for which the possible scattering events are dominated by the wave vectors $\mathbf{q}_1$ along the $\bar{K}$ direction, $\mathbf{q}_2$ along the $\bar{M}$ direction, and $\mathbf{q}_3$ between the $\bar{K}$ and $\bar{M}$ directions. However, from Fig. 30(c) we see that there is a peak along

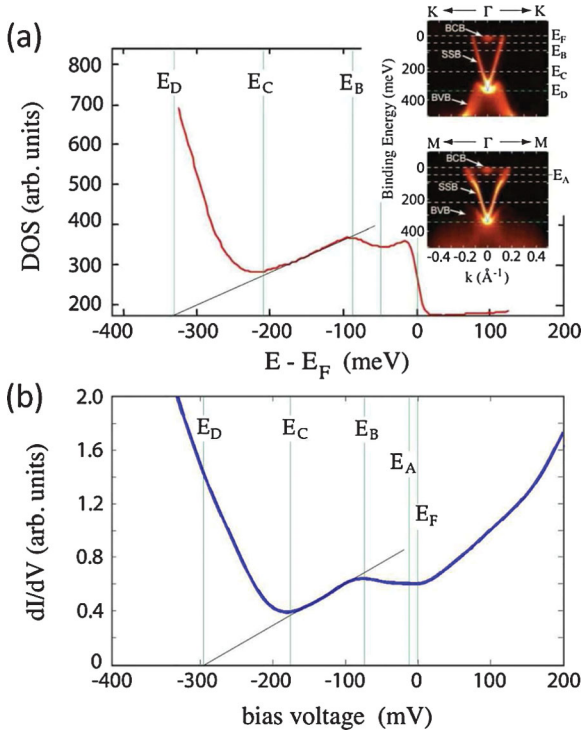

FIG. 29 (color). Good agreement is found between (a) the integrated density of states from ARPES and (b) a typical scanning tunneling spectroscopy spectrum. E_F is the Fermi level, E_A is the bottom of the bulk conduction band, E_B is the point where the surface states become warped, E_C is the top of the bulk valence band, and E_D is the Dirac point. From Alpichshev *et al.*, 2010.

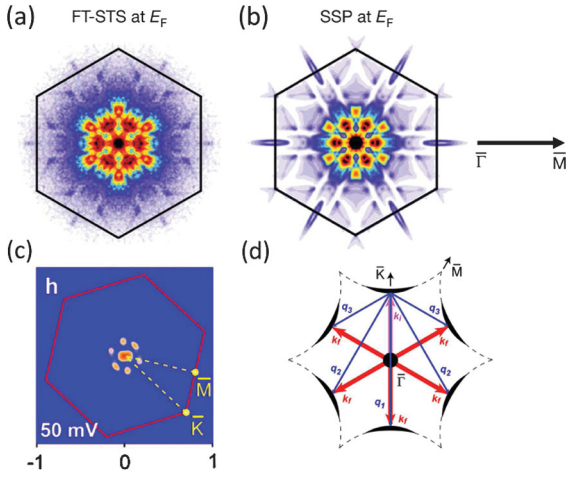

FIG. 30 (color). (a) Measured interference pattern in momentum space for impurities on the surface of Bi_xSb_{1-x}. (b) Pattern calculated from ARPES data on Bi_xSb_{1-x}, which agrees well with the interference pattern in (a). (c) Similar interference pattern and (d) possible scattering wave vectors for Bi_2Te_3. From Roushan *et al.*, 2009, and T. Zhang *et al.*, 2009.

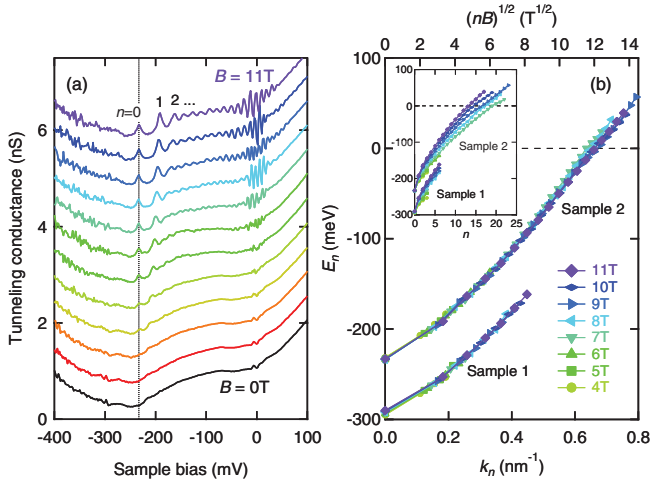

FIG. 31 (color). Tunneling spectra for the surface of Bi_2Se_3 in a magnetic field, showing a series of peaks attributed to the occurrence of surface Landau levels. From Cheng *et al.*, 2010, and Hanaguri *et al.*, 2010.

the $\bar{\Gamma}-\bar{M}$ direction, while scattering along the $\bar{\Gamma}-\bar{K}$ direction is suppressed. This observation coincides with the theoretical prediction that backscattering between $\mathbf{k}$ and $-\mathbf{k}$ is forbidden due to TR symmetry, which supports the topological nature of the surface states. Other related theoretical analyses are also consistent (Zhou *et al.*, 2009; Biswas and Balatsky, 2010; Guo and Franz, 2010). A similar analysis can be applied to the surface of Bi_xSb_{1-x}, and the obtained pattern [Fig. 30(b)] also agrees well with the experimental data [Fig. 30(a)] (Roushan *et al.*, 2009). More recently, STM experiments further demonstrated that the topological surface states can penetrate barriers while maintaining their extended nature (Seo *et al.*, 2010).

Another important result of STM/STS measurements is the observation of surface-state LLs in a magnetic field (Cheng *et al.*, 2010; Hanaguri *et al.*, 2010). As shown in Figs. 31(a) and 31(b), discrete LLs appear as a series of peaks in the differential conductance spectrum (dI/dV), which supports the 2D nature of the surface states. Further analysis on the dependence of the LLs on the magnetic field B shows that the energy of the LLs is proportional to $\sqrt{nB}$, where n is the Landau level index instead of the usual linear-in-B dependence. This unusual dependence provides additional evidence for the existence of surface states consisting of massless Dirac fermions. Furthermore, the narrow peaks in the spectrum also indicate the good quality of the sample surface.

4. Transport

In addition to the above surface-sensitive techniques, a large effort has been devoted to transport measurements including dc transport (Analytis, Chu *et al.*, 2010; Butch *et al.*, 2010; J. Chen *et al.*, 2010; Eto *et al.*, 2010; Steinberg *et al.*, 2010; Tang *et al.*, 2010) and measurements in the microwave (Analytis, McDonald *et al.*, 2010) and infrared regimes (Butch *et al.*, 2010; LaForge *et al.*, 2010; Sushkov *et al.*, 2010), which are necessary steps toward the direct measurement of topological effects such as the TME, and for future device applications. However, transport experiments on topological insulators turn out to be much more difficult than surface-sensitive measurements such as ARPES and STM. The main difficulty arises from the existence of a finite residual bulk carrier density. Materials such as $Bi_{1-x}Sb_x$ or Bi_2Se_3 are predicted to be topological insulators if they are perfectly crystalline. However, real materials always have impurities and defects such as antisites and vacancies. Therefore, as-grown materials are not truly insulating but have a finite bulk carrier density. As discussed in Sec. III.E.2, such a residual bulk carrier density is also observed in ARPES for Bi_2Se_3 and Bi_2Te_3 (Chen *et al.*, 2009; Hsieh *et al.*, 2009a). From the ARPES results it seems that the residual carrier density can be compensated for by chemical doping (Chen *et al.*, 2009). Nevertheless, in transport experiments the compensation of bulk carriers appears to be much more difficult. Even samples which appear as bulk insulators in ARPES experiments still exhibit some finite bulk carrier density in transport measurements (Analytis, Chu *et al.*, 2010), which suggests the existence of an offset between bulk and surface Fermi levels. Another difficulty in transport measurements is that a cleaved surface rapidly becomes heavily n doped when exposed to air. This leads to further discrepancies between the surface condition observed in transport and surface-sensitive measurements.

In spite of the complexity described above, the signature of 2D surface states in transport experiments has recently been reported (Analytis, Chu *et al.*, 2010; Ayala-Valenzuela *et al.*, 2010). For example, Fig. 32(a) shows the quantum oscillation observed in magnetoresistance of $Bi(Sb)_2Se_3$ (Analytis, Chu *et al.*, 2010). As shown in Fig. 32(b), in strong magnetic field, the quantum oscillation scales only with perpendicular magnetic field $B_\perp$, which is the signature of 2D surface states. A similar experiment has also been done for Bi_xSb_{1-x} (Taskin and Ando, 2009). A microwave spectroscopy experiment (Ayala-Valenzuela *et al.*, 2010) on Bi_2Se_3 has shown that

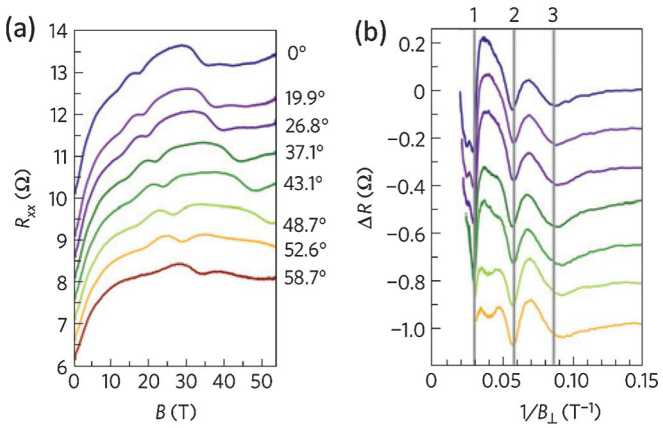

FIG. 32 (color). (a) R_{xx} as a function of the magnetic field with indicated angles for a single crystal of Bi_2Se_3 doped with Sb with the carrier density $n \sim 4 \times 10^{16}$ cm^{-3}. $\theta = 0$ is defined when the field is perpendicular to the surface (parallel to the trigonal c axis). (b) R_{xx} with a smooth background subtracted from the raw data is plotted as a function of $1/B_\perp$ with $B_\perp = B\cos\theta$ the perpendicular component of the magnetic field. Adapted from Analytis, Chu *et al.*, 2010.

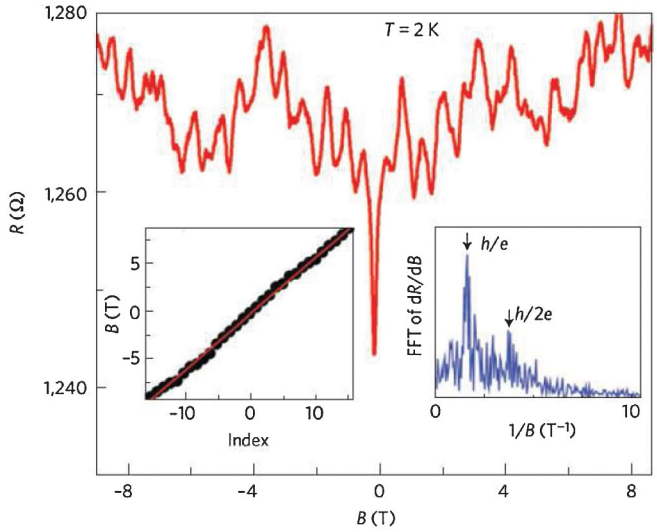

FIG. 33 (color). Magnetoresistance for fields up to ±9 T. Left inset: Magnetic fields at which well-developed resistance minima are observed. Right inset: Fast Fourier transform of the resistance derivative dR/dB, where peaks correspond to hc/e and $hc/2e$ oscillations are labeled. From Peng *et al.*, 2010.

the cyclotron resonance frequency in a strong magnetic field depends only on the perpendicular component of the field, which further supports the existence of 2D surface states. Signatures of the topological surface states have also been searched for in the temperature dependence of the resistance (Checkelsky *et al.*, 2009; Analytis, McDonald *et al.*, 2010; Checkelsky *et al.*, 2011), the magnetoresistance (Tang *et al.*, 2010), and weak antilocalization effects (J. Chen *et al.*, 2010; Checkelsky *et al.*, 2011). However, besides the experiments mentioned above with positive evidence for the existence of topological surface states, some experiments show that the transport data can be entirely explained by bulk carriers (Butch *et al.*, 2010; Eto *et al.*, 2010). The resolution of this controversy requires further improvements in experiments and sample quality.

To reach the intrinsic topological insulator state without bulk carriers, various efforts have been made to reduce the bulk carrier density. One approach consists of compensating the bulk carriers by chemical doping, e.g., doping Bi_2Se_3 with Sb (Analytis, McDonald *et al.*, 2010), Ca (Hor *et al.*, 2009; Hsieh *et al.*, 2009a), or doping Bi_2Te_3 with Sn (Chen *et al.*, 2009). Although chemical doping is an efficient way to reduce the bulk carrier density, the mobility will usually be reduced due to foreign dopants. However, we note that the substitution of the isovalent Bi with Sb can reduce the carrier density but still keep high mobilities (Analytis, McDonald *et al.*, 2010). Also, it is difficult to achieve accurate tuning of the carrier density by chemical doping, because each different chemical doping level needs to be reached by growing a new sample. The second method consists of suppressing the contribution of bulk carriers to transport by reducing the sample size down to the nanoscale, such as quasi-1D nanoribbons (Kong, Randel *et al.*, 2010; Peng *et al.*, 2010; Steinberg *et al.*, 2010), or quasi-2D thin film (J. Chen *et al.*, 2010; Y.-Y. Li *et al.*, 2010; Checkelsky *et al.*, 2011). In Fig. 33, the magnetoresistance of a nanoribbon exhibits a primary hc/e

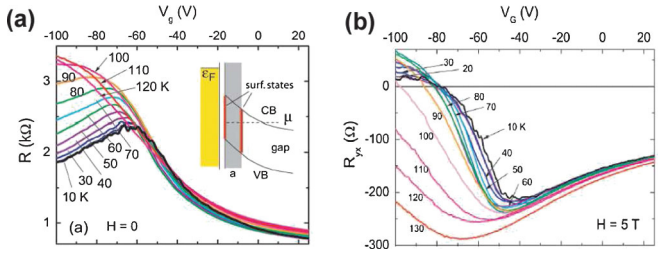

FIG. 34 (color). (a) Gate-voltage dependence of the resistance in zero magnetic field for different temperatures. (b) Gate-voltage dependence of the Hall resistance R_{yx} in a magnetic field of 5 T for different temperatures. From Checkelsky *et al.*, 2011.

oscillation, which corresponds to Aharonov-Bohm oscillations of the surface state around the surface of the nanoribbon (Peng *et al.*, 2010). This oscillation also indicates that the bulk carrier density has been greatly reduced so that the contribution of the surface states can be observed. The Aharonov-Bohm oscillation has also been investigated theoretically (Bardarson *et al.*, 2010; Zhang and Vishwanath, 2010). An important advantage of a sample of mesoscopic size is the possibility of tuning the carrier density by an external gate voltage. Gate control of the carrier density is rather important because it can tune the bulk carrier density continuously while preserving the quality of the sample. Gate control of the carrier density has been indeed observed in nanoribbons of Bi_2Se_3 (Steinberg *et al.*, 2010), mechanically exfoliated thin films (Checkelsky *et al.*, 2011), and epitaxially grown thin films (J. Chen *et al.*, 2010). In particular, tuning of the carrier polarity from n type to p type has been reported (Checkelsky *et al.*, 2011), where the change in polarity corresponds to a sign change of the Hall resistance R_{yx} in a magnetic field [Fig. 34(b)].

F. Other topological insulator materials

The topological materials HgTe, $Bi_{1-x}Sb_x$, Bi_2Se_3, Bi_2Te_3, and Sb_2Te_3 not only provide us with a prototype material for 2D and 3D topological insulators, but also give us a rule of thumb to search for new topological insulator materials. The nontrivial topological property of topological insulators originates from the inverted band structure induced by SOC. Therefore, it is more likely to find topological insulators in materials which consist of covalent compounds with narrow band gaps and heavy atoms with strong SOC. Following such a guiding principle, a large number of topological insulator materials have been proposed recently, which can be roughly classified into several different groups.

The first group is similar to the tetradymite semiconductors, where the atomic p orbitals of Bi or Sb play an essential role. Thallium-based III-V-VI2 ternary chalcogenides, including $TlBiQ_2$ and $TlSbQ_2$ with Q = Te, Se, and S, belong to this class (Lin, Markiewicz *et al.*, 2010; Yan *et al.*, 2010). These materials have the same rhombohedral crystal structure (space group D_{3d}^5) as the tetradymite semiconductors, but are genuinely 3D, in contrast to the layered tetradymite compounds. These materials have recently been experimentally observed to be topological insulators (Chen *et al.*, 2010b; Sato, Segawa *et al.*, 2010).

A typical material of the second group is distorted bulk HgTe. In contrast to conventional zinc blende semiconductors, HgTe has an inverted bulk band structure with the Γ_8 band being higher in energy than the Γ_6 band. However, HgTe by itself is a semimetal with the Fermi energy at the touching point between the light-hole and heavy-hole Γ_8 bands. Consequently, in order to get a topological insulator, the crystal structure of HgTe should be distorted along the [111] direction to open a gap between the heavy-hole and light-hole bands (Dai *et al.*, 2008). A similar band structure also exists in ternary Heusler compounds (Chadov *et al.*, 2010; Lin, Wray *et al.*, 2010), and around 50 of them are found to exhibit band inversion. These materials become 3D topological insulators upon distortion, or they can be grown in quantum well form similar to HgTe/CdTe to realize the 2D or the QSH insulators. Because of the diversity of Heusler materials, multifunctional topological insulators can be realized with additional properties ranging from superconductivity to magnetism and heavy-fermion behavior.

Besides the above two large groups of materials, there are also some other theoretical proposals of new topological insulator materials with electron correlation effects. An example is the case of Ir-based materials. The QSH effect has been proposed in Na_2IrO_3 (Shitade *et al.*, 2009), and topological Mott insulator phases have been proposed in Ir-based pyrochlore oxides $Ln_2Ir_2O_7$ with Ln = Nd, Pr (Guo and Franz, 2009; Pesin and Balents, 2010; Yang and Kim, 2010; Wan *et al.*, 2011). Furthermore, a topological structure has also been considered in Kondo insulators, with a possible realization in SmB_6 and CeNiSn (Dzero *et al.*, 2010).

In a number of recent proposals, it has been shown that topological insulators can also be realized in optical lattice systems (Zhu *et al.*, 2006; Wu, 2008; Zhang *et al.*, 2008; Bermudez *et al.*, 2009; Goldman *et al.*, 2009; Goldman *et al.*, 2010; Stanescu *et al.*, 2010; Bermudez, Goldman *et al.*, 2010; Bermudez, Mazza *et al.*, 2010; Bercioux *et al.*, 2011).

IV. GENERAL THEORY OF TOPOLOGICAL INSULATORS

The TFT (Qi, Hughes, and Zhang, 2008) and the TBT (Kane and Mele, 2005b; Fu and Kane, 2007; Fu *et al.*, 2007; Moore and Balents, 2007; Roy, 2009b) are two different general theories of the topological insulators. The TBT is valid for the noninteracting system without disorder, although in some cases the stability of the topological phases described by TBT upon weak disorder and interaction has been studied through the boundary theory (Wu *et al.*, 2006; Xu and Moore, 2006; Nomura *et al.*, 2007). The TBT has given simple and important criteria to evaluate which band insulators are topologically nontrivial. The TFT is generally valid for interacting systems including disorder, and thus it identifies the physical response associated with the topological order. Remarkably, the TFT reduces exactly to the TBT in the noninteracting limit. In this section, we review both general theories and also discuss their connections.

A. Topological field theory

We are generally interested in the long-wavelength and low-energy properties of a condensed matter system. In this case, the details of the microscopic Hamiltonian are not important, and we want to capture essential physical properties in terms of a low-energy effective field theory. For conventional broken-symmetry states, the low-energy effective field theory is fully determined by the order parameter, symmetry, and dimensionality (Anderson, 1997). Topological states of quantum matter are similarly described by a low-energy effective field theory. In this case, the effective field theory generally involves topological terms which describe the universal topological properties of the state. The coefficient of the topological term can be generally identified as the topological order parameter of the system. A successful example is the TFT of the QH effect (Zhang, 1992), which captures the universal topological properties such as the quantization of the Hall conductance, the fractional charge and statistics of the quasiparticles, and the ground-state degeneracy on a topologically nontrivial spatial manifold. In this section, we describe the TFT of the TR invariant topological insulators.

1. Chern-Simons insulator in 2 + 1 dimensions

We start from the previously mentioned QH system in (2 + 1)D, the TFT of which is given as (Zhang, 1992)

$$S_{\text{eff}} = \frac{C_1}{4\pi}\int d^2x \int dt A_\mu \epsilon^{\mu\nu\tau}\partial_\nu A_\tau, \tag{47}$$

where the coefficient C_1 is generally given by (Wang *et al.*, 2010b)

$$C_1 = \frac{\pi}{3}\int \frac{d^3k}{(2\pi)^3}\,\mathrm{Tr}[\epsilon^{\mu\nu\rho}G\partial_\mu G^{-1}G\partial_\nu G^{-1}G\partial_\rho G^{-1}], \tag{48}$$

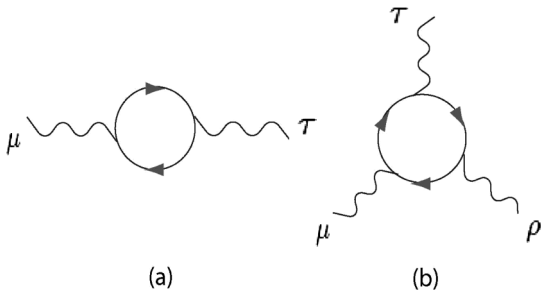

FIG. 35. Fermion loop diagrams leading to the Chern-Simons term. (a) The (2 + 1)D Chern-Simons term is calculated from a loop diagram with two external photon lines. (b) The (4 + 1)D Chern-Simons term is calculated from a loop diagram with three external photon lines.

in which $G(k) \equiv G(\mathbf{k}, \omega)$ is the imaginary-time single-particle Green's function of a fully interacting insulator, and $\mu, \nu, \rho = 0, 1, 2 \equiv t, x, y$. For a general interacting system, assuming that G is nonsingular, we have a map from the three-dimensional momentum space to the space of nonsingular Green's functions, belonging to the group $\mathrm{GL}(n, \mathbb{C})$, whose third homotopy group is labeled by an integer (Wang *et al.*, 2010b)

$$\pi_3(\mathrm{GL}(n, \mathbb{C})) \cong \mathbb{Z}. \tag{49}$$

The winding number for this homotopy class is exactly measured by C_1, defined in Eq. (48). Here $n \geq 3$ is the number of bands. In the noninteracting limit, C_1 in Eq. (47) can be calculated explicitly from a single Feynman diagram [Fig. 35(a)] (Niemi and Semenoff, 1983; Golterman *et al.*, 1993; Volovik, 2002; Qi, Hughes, and Zhang, 2008), and one obtains C_1 as given in Eq. (48), but with G replaced by the noninteracting Green's function G_0. Carrying out the frequency integral explicitly, one obtains the Thouless–Kohmoto–Nightingale–den Nijs (TKNN) invariant expressed as an integral of the Berry curvature (Thouless *et al.*, 1982)

$$C_1 = \frac{1}{2\pi} \int dk_x \int dk_y f_{xy}(\mathbf{k}) \in \mathbb{Z}, \tag{50}$$

with

$$f_{xy}(\mathbf{k}) = \frac{\partial a_y(\mathbf{k})}{\partial k_x} - \frac{\partial a_x(\mathbf{k})}{\partial k_y},$$
$$a_i(\mathbf{k}) = -i \sum_{\alpha \in \mathrm{occ}} \langle \alpha \mathbf{k} | \frac{\partial}{\partial k_i} | \alpha \mathbf{k} \rangle, \qquad i = x, y.$$

Under TR, we have $A_0 \to A_0$, $\mathbf{A} \to -\mathbf{A}$, from which we see that the (2 + 1)D CS field theory in Eq. (47) breaks TR symmetry. The low-energy response of the QH system can be derived from this TFT. For instance, from the effective Lagrangian in Eq. (47), taking a functional derivative with respective to A_μ, we obtain the current

$$j_\mu = \frac{C_1}{2\pi} \epsilon^{\mu\nu\tau} \partial_\nu A_\tau. \tag{51}$$

The spatial component of this current is given by

$$j_i = \frac{C_1}{2\pi} \epsilon^{ij} E_j, \tag{52}$$

while the temporal component is given by

$$j_0 = \frac{C_1}{2\pi} \epsilon^{ij} \partial_i A_j = \frac{C_1}{2\pi} B. \tag{53}$$

This is exactly the QH response with Hall conductance $\sigma_H = C_1/(2\pi)$, implying that an electric field induces a transverse current, and a magnetic field induces charge accumulation. The Maxwell term contains more derivatives than the CS term and is therefore less relevant at low energies in the renormalization group sense. Therefore, the topological response of the QH state is exactly contained in the low-energy TFT of Eq. (47).

2. Chern-Simons insulator in 4 + 1 dimensions

The TFT of the QH effect not only captures the universal low-energy physics, but also points out a way to generalize the TR symmetry-breaking QH state to TR invariant topological states. The CS field theory can be generalized to all odd-dimensional spacetimes (Nakahara, 1990). This observation led Zhang and Hu (2001) to discover a generalization of the QH insulator state which is TR invariant, and defined in (4 + 1)D. It is the fundamental TR invariant insulator state from which all the lower-dimensional cases are derived and is described by the TFT (Fröhlich and Pedrini, 2000; Werner, 2000; Bernevig *et al.*, 2002)

$$S_{\mathrm{eff}} = \frac{C_2}{24\pi^2} \int d^4x dt \epsilon^{\mu\nu\rho\sigma\tau} A_\mu \partial_\nu A_\rho \partial_\sigma A_\tau. \tag{54}$$

Under TR, we have $A_0 \to A_0$, $\mathbf{A} \to -\mathbf{A}$, and this term is explicitly TR invariant. Generally, the coefficient C_2 is expressed in terms of the Green's function of an interacting system as (Wang, Qi, and Zhang, 2010b)

$$C_2 \equiv \frac{\pi^2}{15} \int \frac{d^5k}{(2\pi)^5} \mathrm{Tr}[\epsilon^{\mu\nu\rho\sigma\tau} G \partial_\mu G^{-1} G \partial_\nu G^{-1} G \partial_\rho \times G^{-1} G \partial_\sigma G^{-1} G \partial_\tau G^{-1}], \tag{55}$$

which labels the homotopy group (Wang, Qi, and Zhang, 2010b)

$$\pi_5(\mathrm{GL}(n, \mathbb{C})) \cong \mathbb{Z}, \tag{56}$$

similar to the case of the (2 + 1)D CS term. The generalization of the Green's function approach to the topological characterization of more generic classes of topological insulators and the effect of zeros of the Green's function has been studied recently by Gurarie (2011).

For a noninteracting system, C_2 can be calculated from a single Feynman diagram [Fig. 35(b)] and one obtains C_2 as given in Eq. (55), with G replaced by the noninteracting Green's function G_0. Explicit integration over the frequency gives the second Chern number (Qi, Hughes, and Zhang, 2008b)

$$C_2 = \frac{1}{32\pi^2} \int d^4k \epsilon^{ijk\ell} \mathrm{tr}[f_{ij} f_{k\ell}], \tag{57}$$

with

$$f_{ij}^{\alpha\beta} = \partial_i a_j^{\alpha\beta} - \partial_j a_i^{\alpha\beta} + i[a_i, a_j]^{\alpha\beta},$$
$$a_i^{\alpha\beta}(\mathbf{k}) = -i\langle\alpha, \mathbf{k}|\frac{\partial}{\partial k_i}|\beta, \mathbf{k}\rangle,$$

where $i, j, k, \ell = 1, 2, 3, 4 \equiv x, y, z, w$.

Unlike the (2 + 1)D case, the CS term is less relevant than the nontopological Maxwell term in (4 + 1)D, but is still of primary importance when understanding topological phenomena such as the chiral anomaly in a (3 + 1)D system, which can be regarded as the boundary of a (4 + 1)D system (Qi, Hughes, and Zhang, 2008b). Similar to the (2 + 1)D QH case, the physical response of (4 + 1)D CS insulators is given by

$$j^\mu = \frac{C_2}{2\pi^2}\epsilon^{\mu\nu\rho\sigma\tau}\partial_\nu A_\rho \partial_\sigma A_\tau, \tag{58}$$

which is the nonlinear response to the external field A_μ. To understand this response better, we consider a special field configuration (Qi, Hughes, and Zhang, 2008b):

$$A_x = 0, \qquad A_y = B_z x,$$
$$A_z = -E_z t, \qquad A_w = A_t = 0, \tag{59}$$

where x, y, z, and w are spatial coordinates and t is time. The only nonvanishing components of the field strength are $F_{xy} = B_z$ and $F_{zt} = -E_z$. According to Eq. (58), this field configuration induces the current

$$j_w = \frac{C_2}{4\pi^2}B_z E_z.$$

If we integrate the equation above over the x, y dimensions, with periodic boundary conditions and assuming that E_z does not depend on x, y, we obtain

$$\int dxdy j_w = \frac{C_2}{4\pi^2}\left(\int dxdy B_z\right)E_z \equiv \frac{C_2 N_{xy}}{2\pi}E_z, \tag{60}$$

where $N_{xy} = \int dxdy B_z/2\pi$ is the number of flux quanta through the x–y plane, which is always quantized to be an integer. This is exactly the 4D generalization of the QH effect mentioned earlier (Zhang and Hu, 2001). Therefore, from this example we can understand the physical response associated with a nonvanishing second Chern number. In a (4 + 1)D insulator with second Chern number C_2, a quantized Hall conductance $C_2 N_{xy}/2\pi$ in the z–w plane is induced by a magnetic field with flux $2\pi N_{xy}$ in the perpendicular (x–y) plane.

We have discussed the CS insulators in (2 + 1)D and (4 + 1)D. Actually, these discussions can be straightforwardly generalized to higher dimensions. In doing so, it is worth noting that there is an even-odd alternation of the homotopy groups of $\mathrm{GL}(n, \mathbb{C})$: we have $\pi_{2k+1}(\mathrm{GL}(n, \mathbb{C})) \cong \mathbb{Z}$, while $\pi_{2k}(\mathrm{GL}(n, \mathbb{C})) = 0$. This is the mathematical mechanism underlying the fact that CS insulators of integer class exist in even spatial dimensions, but do not exist in odd spatial dimensions. Reduced to noninteracting insulators, this becomes the alternation of Chern numbers. As a number characteristic of complex fiber bundles, Chern numbers exist only in even spatial dimensions. This is an example of the relationship between homotopy theory and homology theory. We will see another example of this relationship in the following section: Both the Wess-Zumino-Witten (WZW) terms and the CS terms are well defined only modulo an integer.

3. Dimensional reduction to the three-dimensional $\mathbb{Z}_2$ topological insulator

The 4D generalization of the QH effect gives the fundamental TR invariant topological insulator from which all lower-dimensional topological insulators can be derived systematically by a procedure called dimensional reduction (Qi, Hughes, and Zhang, 2008). Starting from the (4 + 1)D CS field theory in Eq. (54), we consider field configurations where $A_\mu(x) = A_\mu(x_0, x_1, x_2, x_3)$ is independent of the "extra dimension" $x_4 \equiv w$, for $\mu = (x_0, x_1, x_2, x_3)$, and $A_4 \equiv A_w$ depending on all coordinates $(x_0, x_1, x_2, x_3, x_4)$. We consider the geometry where the extra dimension x_4 forms a small circle. In this case, the x_4 integral in Eq. (54) can be carried out explicitly. After restoring the unit of electron charge e and flux hc/e following the convention in electrodynamics, we obtain an effective TFT in (3 + 1)D

$$S_\theta = \frac{\alpha}{32\pi^2}\int d^3x dt \theta(x, t)\epsilon^{\mu\nu\rho\tau}F_{\mu\nu}F_{\rho\tau}(x, t), \tag{61}$$

where $\alpha = e^2/\hbar c \simeq 1/137$ is the fine-structure constant and

$$\theta(x, t) \equiv C_2\phi(x, t) = C_2\oint dx_4 A_4(x, t, x_4), \tag{62}$$

which can be interpreted as the flux due to the gauge field $A_4(x, t, x_4)$ through the compact extra dimension (Fig. 36). The field $\theta(x, t)$ is called the axion field in the field theory literature (Wilczek, 1987). In order to preserve the spatial and temporal translation symmetry, $\theta(x, t)$ can be chosen as a constant parameter rather than a field. Furthermore, we already explained that the original (4 + 1)D CS TFT is TR invariant. Therefore, it is natural to ask: How can TR symmetry be preserved in the dimensional reduction? If we choose $C_2 = 1$, then $\theta = \phi$ is the magnetic flux threading the compactified circle, and the physics should be invariant under a shift of θ by 2π. TR transforms θ to $-\theta$. Therefore, there are two and only two values of θ which are consistent with TR symmetry, namely, $\theta = 0$ and $\theta = \pi$. In the latter case, TR transforms $\theta = \pi$ to $\theta = -\pi$, which is equivalent to $\theta = \pi$ mod 2π. We therefore conclude that there are two

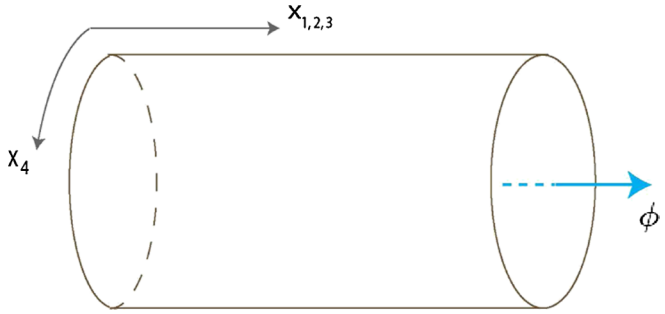

FIG. 36 (color online). Dimensional reduction from (4 + 1)D to (3 + 1)D. The x_4 direction is compactified into a small circle, with a finite flux ϕ threading through the circle due to the gauge field A_4. To preserve TR symmetry, the total flux can be either 0 or π, resulting in a $\mathbb{Z}_2$ classification of 3D topological insulators.

different classes of TR invariant topological insulators in 3D, the topologically trivial class with $\theta = 0$ and the topologically nontrivial class with $\theta = \pi$.

As just seen, it is most natural to view the 3D topological insulator as a dimensionally reduced version of the 4D topological insulator. However, for most physical systems in 3D, we are generally given an interacting Hamiltonian, and we want to define a topological order parameter that can be evaluated directly for any 3D model Hamiltonian. Since the θ angle can take only the two values 0 and π in the presence of TR symmetry, it can be naturally defined as the topological order parameter itself. For a generally interacting system, it is given by (Wang *et al.*, 2010b)

$$P_3 \equiv \frac{\theta}{2\pi} = \frac{\pi}{6}\int_0^1 du \int \frac{d^4k}{(2\pi)^4}\,\mathrm{Tr}\epsilon^{\mu\nu\rho\sigma}[G\partial_\mu G^{-1} G\partial_\nu \times G^{-1}G\partial_\rho G^{-1}G\partial_\sigma G^{-1}G\partial_u G^{-1}], \tag{63}$$

where the momentum $\mathbf{k} = (k_1, k_2, k_3)$ is integrated over the 3D Brillouin zone and the frequency k_0 is integrated over $(-\infty, +\infty)$. $G(k, u = 0) \equiv G(k_0, \mathbf{k}, u = 0) \equiv G(k_0, \mathbf{k})$ is the imaginary-time single-particle Green's function of the interacting many-body system, and $G(k, u)$ for $u \neq 0$ is a smooth extension of $G(k, u = 0)$, with a fixed reference value $G(k, u = 1)$ corresponding to the Green's function of a topologically trivial insulating state. $G(k, u = 1)$ can be chosen as a diagonal matrix with $G_{\alpha\alpha} = (ik_0 - \Delta)^{-1}$ for empty bands α and $G_{\beta\beta} = (ik_0 + \Delta)^{-1}$ for filled bands β, where $\Delta > 0$ is independent of $\mathbf{k}$. Even though P_3 is a physical quantity in 3D, a WZW (Witten, 1983) type of extension parameter u is introduced in its definition, which plays the role of k_4 in Eq. (55) defining the 4D topological insulator (TI). The definition in momentum space is analogous to the real-space WZW term. Similar to the WZW term, P_3 is only well defined modulo an integer and can take only the quantized values of 0 or $1/2$ modulo an integer for an TR invariant insulator (Wang *et al.*, 2010b).

Essential for the definition of P_3 in Eq. (63) is the TR invariance identity (Wang *et al.*, 2010b)

$$G(k_0, -\mathbf{k}) = TG(k_0, \mathbf{k})^T T^{-1}, \tag{64}$$

which is crucial for the quantization of P_3. Therefore, we see that unlike the integer-class CS insulators, the $\mathbb{Z}_2$ insulators are *symmetry-protected* topological insulators. This can be clearly seen from the viewpoint of the topological order parameter. In fact, the quantization of P_3 is protected by TR symmetry. In other words, if TR symmetry in Eq. (64) is broken, then P_3 can be tuned continuously and can be adiabatically connected from $1/2$ to 0. This is fundamentally different from the CS insulators, for which the coefficient of the CS term given by Eq. (55) is always quantized to be an integer, regardless of the presence or absence of symmetries. This integer, if nonzero, cannot be smoothly connected to zero provided that the energy gap remains open. There exists a more exhaustive classification scheme for topological insulators in various dimensions (Qi, Hughes, and Zhang, 2008b; Kitaev, 2009; Ryu, Schnyder *et al.*, 2010) which takes into account the constraints imposed by various symmetries.

For a noninteracting system, the full Green's function G in the expression for P_3 [Eq. (63)] is replaced by the noninteracting Green's function G_0. Furthermore, the frequency integral can be carried out explicitly. After some manipulations, one finds a simple formula

$$P_3 = \frac{1}{16\pi^2}\int d^3k\epsilon^{ijk}\,\mathrm{Tr}\left\{\left[f_{ij}(\mathbf{k}) - \frac{2}{3}ia_i(\mathbf{k})a_j(\mathbf{k})\right]a_k(\mathbf{k})\right\}, \tag{65}$$

which expresses P_3 as the integral of the CS form over the 3D momentum space. For explicit models of topological insulators, such as the model by H. Zhang *et al.* (2009) discussed in Sec. III.A, one can evaluate this formula explicitly to obtain

$$P_3 = \theta/2\pi = 1/2 \tag{66}$$

in the topologically nontrivial state (Qi, Hughes, and Zhang, 2008b). Essin, Moore, and Vanderbilt (2009) also calculated P_3 for a variety of interesting models. In a generic system without time-reversal or inversion symmetry, there may be nontopological contributions to the effective action (61) which modifies the formula of P_3 given in Eq. (65). However, such corrections vanish when time-reversal symmetry or inversion symmetry is present, so that the quantized value $P_3 = 1/2 \pmod 1$ in the topological insulator remains robust (Essin *et al.*, 2010; Malashevich *et al.*, 2010).

Similar to the case of (4 + 1)D CS insulators, there is also an important difference between the θ term for (3 + 1)D topological insulators and the (2 + 1)D CS term for QH systems, which we shall briefly discuss (Maciejko *et al.*, 2010). In (2 + 1)D, the topological CS term dominates over the nontopological Maxwell term at low energies in the renormalization group flow, as a simple result of dimensional analysis. However, in (3 + 1)D, the θ term has the same scaling dimension as the Maxwell term and is therefore equally important at low energies. The full set of modified Maxwell's equations including the topological term (62) is given by

$$\frac{1}{4\pi}\partial_\nu F^{\mu\nu} + \partial_\nu \mathcal{P}^{\mu\nu} + \frac{\alpha}{4\pi}\epsilon^{\mu\nu\sigma\tau}\partial_\nu(P_3 F_{\sigma\tau}) = \frac{1}{c}j^\mu, \tag{67}$$

which can be written in component form as

$$\begin{aligned}
&\nabla\cdot\mathbf{D} = 4\pi\rho + 2\alpha(\nabla P_3\cdot\mathbf{B}),\\
&\nabla\times\mathbf{H} - \frac{1}{c}\frac{\partial\mathbf{D}}{\partial t} = \frac{4\pi}{c}\mathbf{j} - 2\alpha\left((\nabla P_3\times\mathbf{E}) + \frac{1}{c}(\partial_t P_3)\mathbf{B}\right),\\
&\nabla\times\mathbf{E} + \frac{1}{c}\frac{\partial\mathbf{B}}{\partial t} = 0, \qquad \nabla\cdot\mathbf{B} = 0,
\end{aligned} \tag{68}$$

where $\mathbf{D} = \mathbf{E} + 4\pi\mathbf{P}$ and $\mathbf{H} = \mathbf{B} - 4\pi\mathbf{M}$ include only the nontopological contributions. Alternatively, one can use the ordinary Maxwell's equations with modified constituent equations (40). These sets of modified Maxwell equations are called the axion electrodynamics in field theory (Wilczek, 1987).

Even though the conventional Maxwell term and the topological term are both present, experimental designs exist which can in principle extract the purely topological contributions (Maciejko *et al.*, 2010). Furthermore, the topological response is completely captured by the TFT, as is discussed

below. Starting from the TFT [Eq. (61)], we take a functional derivative with respect to A_μ and obtain the current as

$$j^\mu = \frac{1}{2\pi}\epsilon^{\mu\nu\sigma\tau}\partial_\nu P_3 \partial_\sigma A_\tau, \tag{69}$$

which is the general topological response of (3 + 1)D insulators. It is worth noting that we do not assume TR invariance here; otherwise, P_3 should be quantized to be an integer or half-integer. In fact, here we assume an inhomogeneous $P_3(x, t)$. It is interesting to note that this electromagnetic response looks similar to the 4D response in Eq. (58), with the only difference being that A_4 is replaced by P_3 in Eq. (69). This is a manifestation of dimensional reduction at the level of the electromagnetic response. A more systematic treatment on this topic in phase space can be also be performed (Qi, Hughes, and Zhang, 2008b). The physical consequences of Eq. (69) can be understood by studying the following two cases.

1. Half-QH effect on the surface of a 3D topological insulator: Consider a system in which $P_3 = P_3(z)$ depends only on z. For example, this can be realized by the lattice Dirac model (Qi, Hughes, and Zhang, 2008b) with $\theta = \theta(z)$ (Fradkin *et al.*, 1986; Wilczek, 1987). In this case, Eq. (69) becomes

$$j^\mu = \frac{\partial_z P_3}{2\pi}\epsilon^{\mu\nu\rho}\partial_\nu A_\rho,\ \mu, \nu, \rho = t, x, y,$$

which describes a QH effect in the x–y plane with Hall conductivity $\sigma_{xy} = \partial_z P_3/2\pi$. A uniform electric field E_x along the x direction induces a current density along the y direction $j_y = (\partial_z P_3/2\pi)E_x$, the integration of which along the z direction gives the Hall current

$$J_y^{2\mathrm{D}} = \int_{z_1}^{z_2} dz j_y = \frac{1}{2\pi}\left(\int_{z_1}^{z_2} dP_3\right)E_x,$$

which corresponds to a 2D QH conductance

$$\sigma_{xy}^{2\mathrm{D}} = \int_{z_1}^{z_2} dP_3/2\pi. \tag{70}$$

For an interface between a topologically nontrivial insulator with $P_3 = 1/2$ and a topologically trivial insulator with $P_3 = 0$, which can be taken as the vacuum, the Hall conductance is $\sigma_H = \Delta P_3 = \pm 1/2$. Aside from an integer ambiguity, the QH conductance is exactly quantized, independent of the details of the interface. As discussed in Sec. III.D.1, the half-quantum Hall effect on the surface is a reflection of the bulk topology with $P_3 = 1/2$, and cannot be determined purely from the low-energy surface models.

2. Topological magnetoelectric effect induced by a temporal gradient of P_3: Having considered a time-independent P_3, we now consider the case when $P_3 = P_3(t)$ is spatially uniform, but time dependent. Equation (69) now becomes

$$j^i = -\frac{\partial_t P_3}{2\pi}\epsilon^{ijk}\partial_j A_k, \quad i, j, k = x, y, z,$$

which can be simply written as

$$\mathbf{j} = -\frac{\partial_t P_3}{2\pi}\mathbf{B}. \tag{71}$$

Because the charge polarization $\mathbf{P}$ satisfies $\mathbf{j} = \partial_t \mathbf{P}$, we can integrate Eq. (71) in a static, uniform magnetic field B to get $\partial_t \mathbf{P} = -\partial_t(P_3 \mathbf{B}/2\pi)$, so that

$$\mathbf{P} = -\frac{\mathbf{B}}{2\pi}(P_3 + \mathrm{const}). \tag{72}$$

This equation describes the charge polarization induced by a magnetic field, which is a magnetoelectric effect. The prominent feature here is that it is exactly quantized to a half-integer for a TR invariant topological insulator, which is called the TME (Qi, Hughes, and Zhang, 2008b).

Another related effect originating from the TFT is the Witten effect (Witten, 1979; Qi, Hughes, and Zhang, 2008b). For this discussion, we assume that there are magnetic monopoles. For a uniform P_3, Eq. (71) leads to

$$\nabla \cdot \mathbf{j} = -\frac{\partial_t P_3}{2\pi}\nabla \cdot \mathbf{B}. \tag{73}$$

Even if the magnetic monopoles do not exist as elementary particles, for a lattice system, the monopole density $\rho_m = \nabla \cdot \vec{B}/2\pi$ can still be nonvanishing, and we obtain

$$\partial_t \rho_e = (\partial_t P_3)\rho_m. \tag{74}$$

Therefore, when P_3 is adiabatically changed from zero to $\Theta/2\pi$, the magnetic monopole will acquire an electric charge of

$$Q_e = \frac{\Theta}{2\pi}Q_m, \tag{75}$$

where Q_m is the magnetic charge. Such a relation was first derived by Witten in the context of the topological term in quantum chromodynamics (Witten, 1979) and later discussed in the context of topological insulators (Qi, Hughes, and Zhang, 2008b; Rosenberg and Franz, 2010). This effect could also appear under a different guise in topological exciton condensation (Seradjeh *et al.*, 2009), where a $e/2$ charge is induced by a vortex in the exciton condensate, which serves as the "magnetic monopole."

4. Further dimensional reduction to the two-dimensional $\mathbb{Z}_2$ topological insulator

Now we turn our attention to (2 + 1)D TR invariant $\mathbb{Z}_2$ topological insulators. Similar to the WZW-type topological order parameter P_3 in (3 + 1)D, there is also a topological order parameter defined for (2 + 1)D TR invariant insulators. The main difference between (2 + 1)D and (3 + 1)D is that in (2 + 1)D we need two WZW extension parameters u and v, in contrast to a single parameter u in (3 + 1)D, which is a manifestation of the fact that both descend from the fundamental (4 + 1)D topological insulator (Zhang and Hu, 2001). For a general interacting insulator, the (2 + 1)D topological order parameter is expressed as (Wang *et al.*, 2010b)

$$\begin{aligned} P_2 = \frac{1}{120}\epsilon^{\mu\nu\rho\sigma\tau}\int_{-1}^{1} du \int_{-1}^{1} dv \int \frac{d^3k}{(2\pi)^3}\,\mathrm{Tr}[G\partial_\mu G^{-1} \\ \times G\partial_\nu G^{-1} G\partial_\rho G^{-1} G\partial_\sigma G^{-1} G\partial_\tau G^{-1}] \\ = 0 \quad \text{or} \quad 1/2(\mathrm{mod}\mathbb{Z}), \end{aligned} \tag{76}$$

where $\epsilon^{\mu\nu\rho\sigma\tau}$ is the totally antisymmetric tensor in five dimensions, taking value 1 when the variables are an even permutation of (k_0, k_1, k_2, u, v). The cases $P_2 = 0$ and $P_2 = 1/2$ modulo an integer correspond to topologically trivial and nontrivial TR invariant insulators in (2 + 1)D, respectively. This topological order parameter is valid for interacting QSH systems in (2 + 1)D, including states in the Mott regime (Raghu *et al.*, 2008). P_2 can be physically measured by the fractional charge at the edge of the QSH state (Qi, Hughes, and Zhang, 2008a).

5. General phase diagram of topological Mott insulator and topological Anderson insulator

So far we have introduced topological order parameters for TR invariant topological insulators in 4D, 3D, and 2D. These topological order parameters are defined in terms of the full single-particle Green's function. A caution in order is that these topological order parameters are not applicable to fractional states with ground-state degeneracy (Bernevig and Zhang, 2006; Levin and Stern, 2009; Swingle *et al.*, 2010; Maciejko, Qi, Karch, Zhang, 2010), for which a TFT approach is still possible, but simple topological order parameters are harder to find. In 3D, fractional topological insulators are characterized by a topological order parameter P_3 that is a rational multiple of $1/2$ (Maciejko, Qi, Karch, Zhang, 2010; Swingle *et al.*, 2010). Such states are consistent with TR symmetry if fractionally charged excitations and ground-state degeneracies on spatial manifolds of nontrivial topology are present. When TR symmetry is broken on the surface, a fractional TME gives rise to half of a fractional QH effect on the surface (Maciejko, Qi, Karch, Zhang, 2010; Swingle *et al.*, 2010).

Next we discuss the physical consequences implied by the topological order parameters such as P_2 and P_3. The discussion we present is very general and its applicability does not depend on the spatial dimensions. Furthermore, since the topological order parameters are expressed in terms of the full Green's function of an interacting system, they can be useful to general interacting systems. Suppose we have a family of Hamiltonians labeled by several parameters. To be specific, we consider a typical phase diagram (Wang *et al.*, 2010b) (see Fig. 37) for an interacting Hamiltonian $H = H_0(\lambda) + H_1(g)$, where H_0 is the noninteracting part including terms such as $t_{ij}c_i^\dagger c_j$, and H_1 is the electron-electron interaction part including terms such as the Hubbard interaction $gn_{i\downarrow}n_{i\uparrow}$. These two parts are determined by single-particle parameters $\lambda = (\lambda_1, \lambda_2, \ldots)$ and coupling constants $g = (g_1, g_2, \ldots)$. When (λ, g) are smoothly tuned, the ground state also evolves smoothly, as long as the energy gap remains open and the topological order parameters, such as P_2 and P_3, remain unchanged. Only when the gap closes and the full Green's function G becomes singular do these topological order parameters have a jump, as indicated by the curve ab in Fig. 37. [More generically, there may be a metal phase rather than a direct transition between the two topologically distinct insulator phases (Murakami *et al.*, 2007) but our discussion here is insensitive to the nature of the transition and/or the intermediate phases.] The most important point in Fig. 37 can be illustrated by considering the vertical line BF. Starting from a noninteracting state F, one

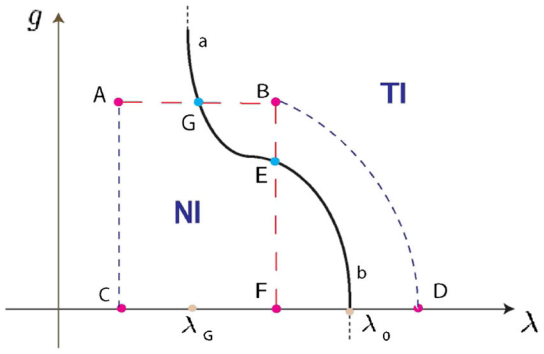

FIG. 37 (color online). Phase diagram in the (λ, g) plane. The dark curve ab is the phase boundary separating normal insulators (NI) and topological insulators (TI). All phases are gapped, except on ab. The true parameter space is in fact infinite dimensional, but this 2D diagram illustrates the main features. From Wang *et al.*, 2010b.

adiabatically tunes on interactions, and eventually there is a phase transition at E to the TI state. The interacting state B, which is an interaction-induced topological insulator state, has a different topological order parameter from the corresponding noninteracting normal insulator state F. The difference in the topological order parameter thus provides a criterion for distinguishing topological classes of insulators in the presence of general interactions.

There have already been several theoretical proposals of strongly interacting topological insulators, i.e., topological Mott insulators (Raghu *et al.*, 2008). 2D topologically nontrivial insulating states have been obtained from the combination of a trivial noninteracting band structure and interaction terms (Raghu *et al.*, 2008; Guo and Franz, 2009; Weeks and Franz, 2010). Such topological insulators can be regarded as topologically nontrivial states arising from dynamically generated SOC (Wu and Zhang, 2004; Wu *et al.*, 2007). The effect of interactions on the QSH state has also been recently studied (Rachel and Hur, 2010). In 3D, strong topological insulators with topological excitations have been obtained (Zhang, Ran, and Vishwanath, 2009; Pesin and Balents, 2010). Topological insulators have been suggested to exist in transition metal oxides (Shitade *et al.*, 2009), where the correlation effect is strong. It was also proposed that one could achieve the topological insulator state in Kondo insulators (Dzero *et al.*, 2010). All these topological Mott insulator states can be understood in the framework of the topological order parameter expressed in terms of the full Green's function (Wang *et al.*, 2010b). Interaction-induced topological insulator states such as the topological Mott insulators proposed by Raghu *et al.* (2008) correspond to regions represented by point B in Fig. 37, which has a trivial noninteracting unperturbed Hamiltonian $H_0(B)$, but acquires a nontrivial topological order parameter due to the interaction part $H_1(B)$ of the Hamiltonian. The previously discussed topological order parameters are useful for determining the phase diagrams of interacting systems.

For disordered systems, the topological order parameters are still applicable, with the momenta in the Green's functions replaced by twist boundary conditions. In this case, Fig. 37 can be regarded as a simple phase diagram of

disordered systems, with g interpreted as the disorder strength. The representative point B is a disorder-induced topological insulator state. The disorder-induced TI state has been studied recently (Obuse *et al.*, 2007, 2008; Ryu *et al.*, 2007; Groth *et al.*, 2009; Imura *et al.*, 2009; Jiang *et al.*, 2009; Li *et al.*, 2009; Shindou and Murakami, 2009; Guo, 2010; Guo *et al.*, 2010; Loring and Hastings, 2010; Olshanetsky *et al.*, 2010; Ostrovsky *et al.*, 2010; Ryu, Mudry *et al.*, 2010). Therefore, the topological order parameters previously discussed have the ability to describe both interacting and disordered systems.

B. Topological band theory

We now give a brief introduction to TBT. Even though this theory is valid only for noninteracting systems, it has become an important tool in the discovery of new topological materials. Unfortunately, evaluating the $\mathbb{Z}_2$ invariants for a generic band structure is in general a difficult problem. Several approaches have been explored in the literature including spin Chern numbers (Sheng *et al.*, 2006; Fukui and Hatsugai, 2007; Prodan, 2009), topological invariants constructed from Bloch wave functions (Kane and Mele, 2005b; Fu and Kane, 2006; Moore and Balents, 2007; Roy, 2009b), and discrete indices calculated from single-particle states at TRIM in the Brillouin zone (Fu and Kane, 2007). We focus on the last method for its simplicity (Fu and Kane, 2007).

This basic quantity in this approach is the matrix element of the TR operator T between states with TR conjugate momenta $\mathbf{k}$ and $-\mathbf{k}$ (Fu and Kane, 2006)

$$B_{\alpha\beta}(\mathbf{k}) = \langle -\mathbf{k}, \alpha | T | \mathbf{k}, \beta \rangle. \tag{77}$$

Since $B_{\alpha\beta}$ is defined as a matrix element between Bloch states at TR conjugate momenta, it is expected that this quantity contains some information about the band topology of TR invariant topological insulators. At the TRIM Γ_i (see Fig. 38), $B(\mathbf{k} = \Gamma_i)$ is antisymmetric, so that the following quantity can be defined (Fu and Kane, 2006):

$$\delta_i = \frac{\sqrt{\det[B(\Gamma_i)]}}{\mathrm{Pf}[B(\Gamma_i)]}, \tag{78}$$

in which Pf stands for the Pfaffian of an antisymmetric matrix. Since $\mathrm{Pf}[B(\Gamma_i)]^2 = \det[B(\Gamma_i)]$, we have $\delta_i = \pm 1$. It should be noted that the wave functions $|\mathbf{k}, \alpha\rangle$ must be chosen continuously in the BZ to avoid ambiguity in the definition of δ_i. In 1D, there are only two TRIM, and a "TR polarization" (Fu and Kane, 2006) can be defined as the product of δ_i

$$\pi \equiv (-1)^{P_\theta} = \delta_1 \delta_2, \tag{79}$$

which is a $\mathbb{Z}_2$ analog to the charge polarization (Thouless, 1983; Zak, 1989; King-Smith and Vanderbilt, 1993; Resta, 1994). A further analogy between the charge polarization and the TR polarization suggests the form of the $\mathbb{Z}_2$ invariant for TR invariant topological insulators. If an angular parameter θ is tuned from 0 to 2π, the change in the charge polarization P after such a cycle is expressed as the first Chern number C_1 in the (k, θ) space. In fact, the same C_1 gives the TKNN invariant (Thouless, 1983) if θ were regarded as a momentum. By analogy with P, the $\mathbb{Z}_2$ invariant for (2 + 1)D topological insulators can be defined as

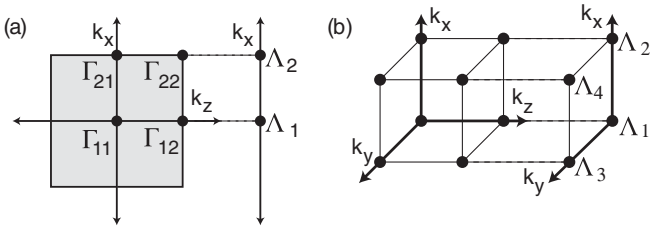

FIG. 38. (a) The 2D bulk Brillouin zone projected onto the 1D edge Brillouin zone. The two edge TRIM Λ_1 and Λ_2 are projections of pairs of the four bulk TRIM $\Gamma_{i=(a\mu)}$. (b) Projection of the TRIM of the 3D Brillouin zone onto a 2D surface Brillouin zone. From Fu and Kane, 2007.

$$(-1)^{\nu_{2D}} = (-1)^{P_\theta(k_2=0) - P_\theta(k_2=\pi)}, \tag{80}$$

where $(-1)^{P_\theta(k_2)} = \delta_1 \delta_2$, δ_i is defined at the TRIM $k_1 = 0$ or π, and k_2 is regarded as a parameter. Expanding Eq. (80) gives

$$(-1)^{\nu_{2D}} = \prod_{i=1}^{4} \delta_i, \tag{81}$$

where $i = 1$, 2, 3, and 4 labels the four TRIM in the 2D Brillouin zone. $(-1)^{\nu_{2D}} = +1$ implies a trivial insulator, while $(-1)^{\nu_{2D}} = -1$ implies a topological insulator. Furthermore, as a TR polarization, ν_{2D} also determines the way in which Kramers pairs of surface states are connected (see Fig. 39), which suggests that bulk topology and edge physics are intimately related. This is another example of the "holographic principle" for topological phenomena in condensed matter physics.

We now discuss 3D topological insulators. It is interesting to note that in TBT the natural route is "dimensional increase," in contrast to the "dimensional reduction" procedure of TFT. From this dimensional increase, the 3D (strong) topological invariant is naturally defined as (Fu and Kane, 2007; Fu *et al.*, 2007)

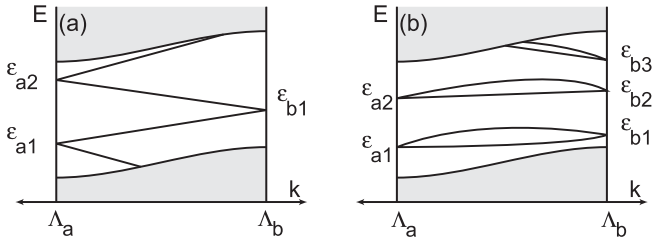

FIG. 39. Schematic representation of the surface energy levels of a crystal in either 2D or 3D, as a function of surface crystal momentum on a path connecting TRIM Λ_a and Λ_b. The shaded region shows the bulk continuum states, and the lines show discrete surface (or edge) bands localized near one of the surfaces. The Kramers degenerate surface states at Λ_a and Λ_b can be connected to each other in two possible ways, shown in (a) and (b), which reflect the change in TR polarization ΔP_θ of the cylinder between those points. (a) occurs in topological insulators and guarantees that the surface bands cross any Fermi energy inside the bulk gap. From Fu *et al.*, 2007.

$$(-1)^{\nu_{3D}} = \prod_{i=1}^{8} \delta_i. \tag{82}$$

In addition to the strong invariant, it has been shown that the product of any four δ_i's for which the Γ_i lie in the same plane is also gauge invariant and defines topological invariants characterizing the band structure (Fu and Kane, 2007). This fact leads to the definition of three additional invariants in 3D, known as weak topological invariants (Fu and Kane, 2007; Fu *et al.*, 2007; Moore and Balents, 2007; Roy, 2009a). These $\mathbb{Z}_2$ invariants can be arranged as a 3D vector with elements ν_k given by

$$(-1)^{\nu_k} = \prod_{n_k=1; n_{j\neq k}=0,1} \delta_{i=(n_1 n_2 n_3)}, \tag{83}$$

where $(\nu_1\nu_2\nu_3)$ depend on the choice of reciprocal lattice vectors and are only strictly well defined when a well-defined lattice is present. It is useful to view these invariants as components of a mod 2 reciprocal lattice vector,

$$\mathbf{G}_\nu = \nu_1\mathbf{b}_1 + \nu_2\mathbf{b}_2 + \nu_3\mathbf{b}_3. \tag{84}$$

When $\nu_0 = 0$, states are classified according to $\mathbf{G}_\nu$, and are called *weak* topological insulators (Fu *et al.*, 2007) when the weak indices ν_k are odd. The only topological insulator with nontrivial weak topological indices which has been realized experimentally is $Bi_{1-x}Sb_x$ alloy, which has $\nu_1 = \nu_2 = \nu_3 = \nu_{3D} = 1$ (Fu and Kane, 2007; Hsieh *et al.*, 2008).

Heuristically these states can be interpreted as stacked QSH states. As an example, consider planes of QSH stacked in the z direction. When the coupling between the layers is zero, the band dispersion will be independent of k_z. It follows that the four δ_i's associated with the plane $k_z = \pi/a$ will have a product of -1 and will be the same as the four associated with the plane $k_z = 0$. The topological invariants will then be given by $\nu_0 = 0$ and $\mathbf{G}_\nu = (2\pi/a)\hat{\mathbf{z}}$. This structure will remain when hopping between the layers is introduced. More generally, when QSH states are stacked in the $\mathbf{G}$ direction, the invariant will be $\mathbf{G}_\nu = \mathbf{G}$ mod 2. This implies that QSH states stacked along different directions $\mathbf{G}_1$ and $\mathbf{G}_2$ are equivalent if $\mathbf{G}_1 = \mathbf{G}_2$ mod 2 (Fu and Kane, 2007). As for the surface states, when the coupling between the layers is zero, it is clear that the gap in the 2D system implies there will be no surface states on the top and bottom surfaces; only the side surfaces will have gapless states. We can also think about the stability of the surface states for the weak insulators. In fact, weak topological insulators are unstable with respect to disorder. We can heuristically see that they are less stable than the strong insulators in the following way. If we stack an odd number of QSH layers, there would at least be one delocalized surface branch. However, the surface states for an even number of layers can be completely localized by disorder or perturbations. Despite this instability, it has been shown (Ran *et al.*, 2009) that the weak topological invariants guarantee the existence of gapless modes on certain crystal defects. For a dislocation with Burgers vector $\mathbf{b}$ it was shown that there will be gapless modes on the dislocation if $\mathbf{G}_\nu \cdot \mathbf{b} = (2n+1)\pi$ for integer n.

Similar to the 2D topological insulator, there are connections between the bulk invariants of the 3D topological insulator and the corresponding 2D surface-state spectrum.

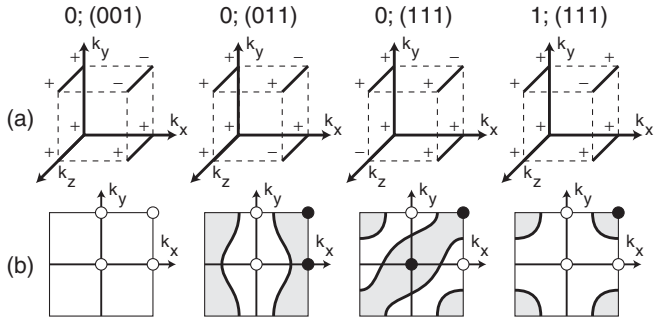

FIG. 40. Diagrams depicting four different phases indexed by $\nu_0;(\nu_1\nu_2\nu_3)$. (a) The signs of δ_i at the points Γ_i on the vertices of a cube. (b) The band structure of a 001 surface for each phase. The solid and open circles depict the TR polarization π_a at the surface momenta Λ_a, which are projections of pairs of Γ_i which differ only in their z component. The thick lines indicate possible Fermi arcs which enclose specific Λ_a. From Fu *et al.*, 2007.

As a sample, Fig. 40 shows four different topological classes for 3D band structures labeled with the corresponding $(\nu_0;\nu_1\nu_2\nu_3)$. The eight Γ_i are represented as the vertices of a cube in momentum space, with the corresponding δ_i shown as $\pm$ signs. The lower panel shows a characteristic surface Brillouin zone for a 001 surface with the four Λ_a labeled by either filled or solid circles, depending on the value of $\pi_a = \delta_{i=(a1)}\delta_{i=(a2)}$. Generically it is expected that the surface band structure will resemble Fig. 39(b) on paths connecting two filled circles or two empty circles and will resemble Fig. 39(a) on paths connecting a filled circle to an empty circle (Fu and Kane, 2007). This consideration determines the 2D surface states qualitatively.

If an insulator has inversion symmetry, there is a simple algorithm to calculate the $\mathbb{Z}_2$ invariant (Fu and Kane, 2007): indeed, the replacement in Eqs. (81) and (82) of δ_i by

$$\delta_i = \prod_{m=1}^{N} \xi_{2m}(\Gamma_i) \tag{85}$$

gives the correct $\mathbb{Z}_2$ invariants. Here $\xi_{2m}(\Gamma_i) = \pm 1$ is the parity eigenvalue of the $2m$th occupied energy band at Γ_i (Fig. 38), which shares the same eigenvalue $\xi_{2m} = \xi_{2m-1}$ with its degenerate Kramers partner (Fu and Kane, 2007). The product is over only half of the occupied bands. Since the definition of the δ_i relies on parity eigenvalues, the δ_i are only well defined in this case when inversion symmetry is present (Fu and Kane, 2007). However, for insulators without inversion symmetry, this algorithm is also useful. In fact, if we can deform a given insulator to an inversion-symmetric insulator and keep the energy gap open along the way, the resultant $\mathbb{Z}_2$ invariants are the same as the initial ones due to topological invariance, but can be calculated from parity (Fu and Kane, 2007).

C. Reduction from topological field theory to topological band theory

We now discuss the relation between the TFT and TBT. On the one hand, the TFT approach is very powerful to reveal various aspects of the low-energy physics, and it also provide

a deep understanding of the universality among different systems. Furthermore, in contrast to TBT, TFT is valid for interacting systems. On the other hand, from a practical viewpoint, we also need fast algorithms to calculate topological invariants, which is the goal of TBT. An intuitive understanding of the TBT of $\mathbb{Z}_2$ topological insulators is as follows. For integer-class CS topological insulators, the topological invariant C_n is expressed as the integral of Green's functions (or Berry curvature, in the noninteracting limit). Therefore, the knowledge of Bloch states over the whole Brillouin zone is needed to calculate C_n. For TR invariant $\mathbb{Z}_2$ topological insulators, the TR symmetry constraint enables us to determine the topological class of a given insulator with less information: We do not need the information over the entire Brillouin zone. For insulators with inversion symmetry, the parity at several high-symmetry points completely determines the topological class (Fu and Kane, 2007), which explains the success of TBT. As naturally expected, the TBT approach is related to the TFT approach. In fact, it has been recently proven (Wang *et al.*, 2010a) that the TFT description can be exactly reduced to the TBT in the noninteracting limit. We now outline this proof (Wang *et al.*, 2010a). Starting from the expression for P_3 in Eqs. (63) and (65), one can show that

$$2P_3(\mathrm{mod}\,2) = -\frac{1}{24\pi^2}\int d^3k\epsilon^{ijk}\,\mathrm{Tr}[(B\partial_i B^\dagger)(B\partial_j B^\dagger) \times (B\partial_k B^\dagger)](\mathrm{mod}\,2). \tag{86}$$

By some topological argument, this expression for P_3 is shown to give the degree $\deg f$ of a certain map f (Dubrovin *et al.*, 1985) from the Brillouin zone three-torus T^3 to the SU(2) group manifold. There are two seemingly different expressions for $\deg f$, one of which is of integral form as given by Eq. (86), while the other is of discrete form and given simply by the number of points mapped to a arbitrarily chosen image in SU(2). Because of TR symmetry, if we choose the image point as one of the two antisymmetric matrices in SU(2) (e.g., $i\sigma_y$), we have an interesting ''pair annihilation'' of those points other than the eight TRIM (Wang *et al.*, 2010a). The final result is exactly the $\mathbb{Z}_2$ invariant from TBT. The explicit relation between TFT and TBT is (Wang *et al.*, 2010a)

$$(-1)^{2P_3} = (-1)^{\nu_{3D}}. \tag{87}$$

V. TOPOLOGICAL SUPERCONDUCTORS AND SUPERFLUIDS

Soon after their discovery, the study of TR invariant topological insulators was generalized to TR invariant topological superconductors and superfluids (Roy, 2008; Schnyder *et al.*, 2008; Kitaev, 2009; Qi, Hughes *et al.*, 2009a). There is a direct analogy between superconductors and insulators because the Bogoliubov–de Gennes (BdG) Hamiltonian for the quasiparticles of a superconductor is analogous to the Hamiltonian of a band insulator, with the superconducting gap corresponding to the band gap of the insulator.

^{3}He-B is an example of such a topological superfluid state. This TR invariant state has a full pairing gap in the bulk and gapless surface states consisting of a single Majorana cone (Roy, 2008; Schnyder *et al.*, 2008; Chung and Zhang, 2009; Qi, Hughes *et al.*, 2009a). In fact, the BdG Hamiltonian for ^{3}He-B is identical to the model Hamiltonian of a 3D topological insulator (H. Zhang *et al.*, 2009) and is investigated extensively in Sec. III.A. In 2D, the classification of topological superconductors is similar to that of topological insulators. TR breaking superconductors are classified by an integer (Volovik, 1988b; Read and Green, 2000), similar to quantum Hall insulators (Thouless *et al.*, 1982), while TR invariant superconductors are classified (Roy, 2008; Schnyder *et al.*, 2008; Kitaev, 2009; Qi, Hughes *et al.*, 2009a) by a $\mathbb{Z}_2$ invariant in 1D and 2D, but by an integer ($\mathbb{Z}$) invariant in 3D (Schnyder *et al.*, 2008; Kitaev, 2009).

Besides the TR invariant topological superconductors, the TR breaking topological superconductors have also attracted a lot of interest recently, because of their relation with non-Abelian statistics and their potential application to topological quantum computation. The TR breaking topological superconductors are described by an integer $\mathcal{N}$. The vortex of a topological superconductor with odd topological quantum number $\mathcal{N}$ carries an odd number of Majorana zero modes (Volovik, 1999), giving rise to non-Abelian statistics (Read and Green, 2000; Ivanov, 2001) which could provide a platform for topological quantum computing (Nayak *et al.*, 2008). The simplest model for an $\mathcal{N}=1$ chiral topological superconductor is realized in the p_x+ip_y pairing state of spinless fermions (Read and Green, 2000). A spinful version of the chiral superconductor has been predicted to exist in Sr_2RuO_4 (Mackenzie and Maeno, 2003), but the experimental situation is far from definitive. Recently, several new proposals to realize Majorana fermion states in conventional superconductors have been investigated by making use of strong SOC (Fu and Kane, 2008; P. Lee, 2009; Qi *et al.*, 2010a; Santos *et al.*, 2010; Sau *et al.*, 2010).

A. Effective models of time-reversal invariant superconductors

The simplest way to understand TR invariant topological superconductors is through their analogy with topological insulators. The 2D chiral superconducting state is the superconductor analog of the QH state. A QH state with Chern number N has N chiral edge states, while a chiral superconductor with topological quantum number $\mathcal{N}$ has $\mathcal{N}$ chiral Majorana edge states. Since the positive and negative energy states of the BdG Hamiltonian of a superconductor describe the same physical degrees of freedom, each chiral Majorana edge state has half the degrees of freedom of the chiral edge state of a QH system. Therefore, the chiral superconductor is the ''minimal'' topological state in 2D. The analogy between a chiral superconductor and a QH state is illustrated in the upper panels of Fig. 41. Following the same analogy, one can consider the superconducting analog of QSH state, a helical superconductor in which fermions with up spins are paired in the p_x+ip_y state, and fermions with down spins are paired in the p_x-ip_y state. Such a TR invariant state has a full gap in the bulk and counterpropagating helical Majorana states at the edge. In contrast, the edge states of the TR invariant topological insulator are helical *Dirac* fermions with twice the degrees of freedom. As is the case for the QSH state, a mass term for the edge states is forbidden by TR symmetry. Therefore, such a superconducting phase is topologically

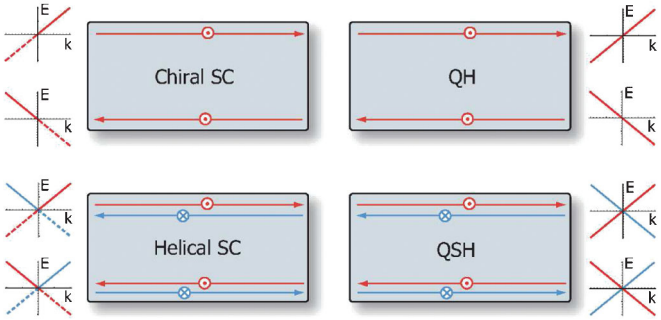

FIG. 41 (color). (Top row) Schematic comparison of 2D chiral superconductor and QH states. In both systems, TR symmetry is broken and the edge states carry a definite chirality. (Bottom row) Schematic comparison of 2D TR invariant topological superconductor and QSH insulator. Both systems preserve TR symmetry and have a helical pair of edge states, where opposite spin states counterpropagate. The dashed lines show that the edge states of the superconductors are Majorana fermions so that the $E<0$ part of the quasiparticle spectrum is redundant. In terms of the edge state degrees of freedom, we have symbolically QSH $=$ (QH)^2 $=$ (helical SC)^2 $=$ (chiral SC)^4. From Qi, Hughes *et al.*, 2009a.

protected in the presence of TR symmetry and can be described by a $\mathbb{Z}_2$ topological quantum number (Roy, 2008; Schnyder *et al.*, 2008; Kitaev, 2009; Qi, Hughes *et al.*, 2009a). The four types of 2D topological states of matter discussed here are summarized in Fig. 41.

As a starting point, we first consider the Hamiltonian of the simplest nontrivial TR breaking superconductor, the $p+ip$ superconductor (Read and Green, 2000) for spinless fermions:

$$H=\frac{1}{2}\sum_{p}(c_{\mathbf{p}}^{\dagger},c_{-\mathbf{p}})\begin{pmatrix}\epsilon_{\mathbf{p}} & \Delta p_{+}\\ \Delta^{*}p_{-} & -\epsilon_{\mathbf{p}}\end{pmatrix}\begin{pmatrix}c_{\mathbf{p}}\\ c_{-\mathbf{p}}^{\dagger}\end{pmatrix}, \tag{88}$$

with $\epsilon_{\mathbf{p}}=\mathbf{p}^2/2m-\mu$ and $p_{\pm}=p_x\pm ip_y$. In the weak pairing phase with $\mu>0$, the p_x+ip_y *chiral* superconductor is known to have chiral Majorana edge states propagating on each boundary, described by the Hamiltonian

$$H_{\text{edge}}=\sum_{k_y\geq 0}v_F k_y\psi_{-k_y}\psi_{k_y}, \tag{89}$$

where $\psi_{-k_y}=\psi_{k_y}^{\dagger}$ is the quasiparticle creation operator (Read and Green, 2000) and the boundary is taken parallel to the y direction. The strong pairing phase $\mu<0$ is trivial, and the two phases are separated by a topological phase transition at $\mu=0$.

In the BHZ model for the QSH state in HgTe (Bernevig *et al.*, 2006), if we ignore the coupling terms between spin-up and spin-down electrons, the system is a direct product of two independent QH systems in which spin-up and spin-down electrons have opposite Hall conductance. In the same way, the simplest model for the topologically nontrivial TR invariant superconductor in 2D is given by the following Hamiltonian:

$$H=\frac{1}{2}\sum_{p}\tilde{\Psi}^{\dagger}\begin{pmatrix}\epsilon_{\mathbf{p}} & \Delta p_{+} & 0 & 0\\ \Delta^{*}p_{-} & -\epsilon_{\mathbf{p}} & 0 & 0\\ 0 & 0 & \epsilon_{\mathbf{p}} & -\Delta^{*}p_{-}\\ 0 & 0 & -\Delta p_{+} & -\epsilon_{\mathbf{p}}\end{pmatrix}\tilde{\Psi}, \tag{90}$$

with $\tilde{\Psi}(\mathbf{p})\equiv(c_{\uparrow\mathbf{p}},c_{\uparrow-\mathbf{p}}^{\dagger},c_{\downarrow\mathbf{p}},c_{\downarrow-\mathbf{p}}^{\dagger})^T$. From Eq. (90) we see that spin-up (spin-down) electrons form p_x+ip_y (p_x-ip_y) Cooper pairs. Comparing this model Hamiltonian (90) for the topological superconductor with the BHZ model of the HgTe topological insulator [Eq. (2)], we first see that the term proportional to the identity matrix in the BHZ model is absent here, reflecting the generic particle-hole symmetry of the BdG Hamiltonian for superconductors. On the other hand, the terms proportional to the Pauli matrices σ^a are *identical* in both cases. Therefore, a topological superconductor can be viewed as a topological insulator with particle-hole symmetry. The topological superconductor Hamiltonian also has half as many degrees of freedom as the topological insulator. The model Hamiltonian (90) is expressed in terms of the Nambu spinor $\tilde{\Psi}(\mathbf{p})$ which artificially doubles the degrees of freedom as compared to the topological insulator Hamiltonian. Bearing these differences in mind, in analogy with the QSH system, we know that the edge states of the TR invariant system described by the Hamiltonian (90) consist of spin-up and spin-down quasiparticles with opposite chiralities

$$H_{\text{edge}}=\sum_{k_y\geq 0}v_F k_y(\psi_{-k_y\uparrow}\psi_{k_y\uparrow}-\psi_{-k_y\downarrow}\psi_{k_y\downarrow}). \tag{91}$$

The quasiparticle operators $\psi_{k_y\uparrow}$ and $\psi_{k_y\downarrow}$ can be expressed in terms of the eigenstates $u_{k_y}(x)$ and $v_{k_y}(x)$ of the BdG Hamiltonian as

$$\psi_{k_y\uparrow}=\int d^2x[u_{k_y}(x)c_{\uparrow}(x)+v_{k_y}(x)c_{\uparrow}^{\dagger}(x)],$$
$$\psi_{k_y\downarrow}=\int d^2x[u_{-k_y}^{*}(x)c_{\downarrow}(x)+v_{-k_y}^{*}(x)c_{\downarrow}^{\dagger}(x)],$$

from which the TR transformation of the quasiparticle operators can be determined to be $T\psi_{k_y\uparrow}T^{-1}=\psi_{-k_y\downarrow}$, and $T\psi_{k_y\downarrow}T^{-1}=-\psi_{-k_y\uparrow}$. In other words $(\psi_{k_y\uparrow},\psi_{-k_y\downarrow})$ transform under TR as a Kramers doublet, which forbids a gap in the edge state spectrum when TR is preserved by preventing the mixing of spin-up and spin-down modes. To see this explicitly, note that the only k_y-independent term that can be added to the edge Hamiltonian (91) is $im\sum_{k_y}\psi_{-k_y\uparrow}\psi_{k_y\downarrow}$, with m real. However, such a term is odd under TR, which implies that any backscattering between quasiparticles is forbidden by TR symmetry. The discussion above is exactly parallel to the $\mathbb{Z}_2$ topological characterization of the QSH system. The edge states of the QSH insulator consist of an odd number of Kramers pairs, which remain gapless under any small TR invariant perturbation (Wu *et al.*, 2006; Xu and Moore, 2006). Such a "helical liquid" with an odd number of Kramers pairs at the Fermi energy cannot be realized in any bulk 1D system, and can appear only *holographically* as the edge theory of a 2D QSH insulator (Wu *et al.*, 2006). Similarly, the edge state theory Eq. (91) can be called a

"helical Majorana liquid," and can exist only on the boundary of a $\mathbb{Z}_2$ topological superconductor. Once such a topological phase is established, it is robust under any TR invariant perturbations such as Rashba-type SOC and s-wave pairing, even if spin rotation symmetry is broken. The edge helical Majorana liquid can be detected by electric transport through a quantum point contact between two topological superconductors (Asano *et al.*, 2010).

The 2D Hamiltonian (90) describes a spin-triplet pairing, the spin polarization of which is correlated with the orbital angular momentum of the pair. Such a correlation can be naturally generalized to 3D where spin polarization and orbital angular momentum are both vectors. The Hamiltonian of such a 3D superconductor is given by

$$H = \frac{1}{2}\sum_p \Psi^\dagger \begin{pmatrix} \epsilon_{\mathbf{p}} \mathbb{I}_{2\times 2} & i\sigma^2\sigma^\alpha \Delta^{\alpha j} p_j \\ \text{H.c.} & -\epsilon_{\mathbf{p}} \mathbb{I}_{2\times 2} \end{pmatrix} \Psi, \tag{92}$$

where we use a different basis $\Psi(\mathbf{p}) \equiv (c_{\uparrow\mathbf{p}}, c_{\downarrow\mathbf{p}}, c^\dagger_{\uparrow-\mathbf{p}}, c^\dagger_{\downarrow-\mathbf{p}})^T$. $\Delta^{\alpha j}$ is a 3×3 matrix with $\alpha = 1, 2$, and 3 and $j = x$, y, and z. Interestingly, an example of such a Hamiltonian is given by the well-known ^{3}He-B phase, for which the order parameter $\Delta^{\alpha j}$ is determined by an orthogonal matrix $\Delta^{\alpha j} = \Delta u^{\alpha j}$, $u \in$ SO(3) (Vollhardt and Wölfle, 1990). Here and below we ignore the dipole-dipole interaction term (Leggett, 1975), since it does not affect any essential topological properties. Performing a spin rotation, $\Delta^{\alpha j}$ can be diagonalized to $\Delta^{\alpha j} = \Delta\delta^{\alpha j}$, in which case the Hamiltonian (92) can be expressed as

$$H = \frac{1}{2}\int d^2x \Psi^\dagger \times \begin{pmatrix} \epsilon_{\mathbf{p}} & 0 & \Delta p_+ & -\Delta p_z \\ 0 & \epsilon_{\mathbf{p}} & -\Delta p_z & -\Delta p_- \\ \Delta^* p_- & -\Delta^* p_z & -\epsilon_{\mathbf{p}} & 0 \\ -\Delta^* p_z & -\Delta^* p_+ & 0 & -\epsilon_{\mathbf{p}} \end{pmatrix} \Psi. \tag{93}$$

Compared with the model Hamiltonian Eq. (31) for the simplest 3D topological insulators (H. Zhang *et al.*, 2009), we see that the Hamiltonian (93) has the same form as that for Bi_2Se_3 (up to a basis transformation), but with complex fermions replaced by Majorana fermions. The kinetic energy term $\mathbf{p}^2/2m - \mu$ corresponds to the momentum-dependent mass term $M(\mathbf{p}) = M - B_1 p_z^2 - B_2 p_\parallel^2$ of the topological insulator. The weak pairing phase $\mu > 0$ corresponds to the nontrivial topological insulator phase, and the strong pairing phase $\mu < 0$ corresponds to the trivial insulator. The two phases are separated by a topological phase transition (Béri, 2010). From this analogy, we see that the superconductor Hamiltonian in the weak pairing phase describes a topological *superconductor* with gapless surface states protected by TR symmetry. Different from the topological insulator, the surface states of the topological superconductor are Majorana fermions described by

$$H_{\text{surf}} = \frac{1}{2}\sum_{\mathbf{k}} v_F \psi^T_{-\mathbf{k}} (k_x\sigma_y - k_y\sigma_x)\psi_{\mathbf{k}}, \tag{94}$$

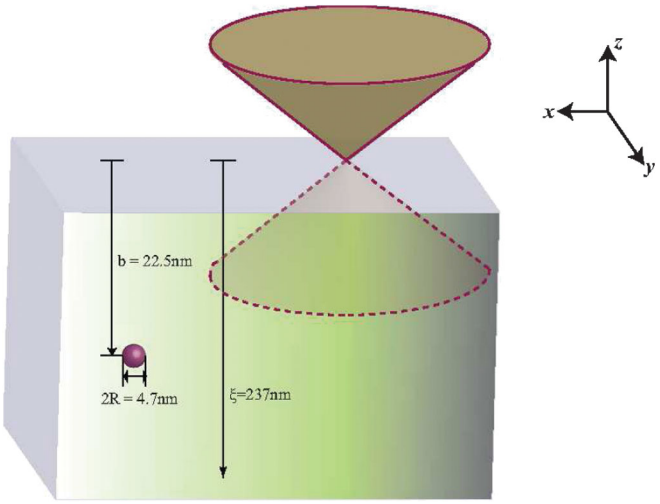

FIG. 42 (color). Setting for detecting the Majorana surface states of the ^{3}He-B phase, which consist of a single Majorana cone. When electrons are injected into ^{3}He-B, they exist as "bubbles." If the injected electrons are spin polarized, the spin will relax by interaction with the surface Majorana modes, and this relaxation is strongly anisotropic. From Chung and Zhang, 2009.

with the Majorana condition $\psi_{-\mathbf{k}} = \sigma_x \psi^{\dagger T}_{\mathbf{k}}$. We see that this Hamiltonian for the surface Majorana fermions of a topological superconductor takes the same form as the surface Dirac Hamiltonian of a topological insulator in this special basis. However, because of the generic particle-hole symmetry of the BdG Hamiltonian for superconductors, the possible particle-hole symmetry-breaking terms for surface Dirac fermions such as a finite chemical potential are absent for surface Majorana fermions. Because of the particle-hole symmetry and TR symmetry, the spin lies strictly in the plane perpendicular to the surface normal, and the integer winding number of the spin around the momentum is now a well-defined quantity. This integer winding number gives a $\mathbb{Z}$ classification of the 3D topological superconductor (Schnyder *et al.*, 2008; Kitaev, 2009). The surface state remains gapless under any small TR invariant perturbation, since the only available mass term $m\sum_{\mathbf{k}} \psi^T_{-\mathbf{k}} \sigma^y \psi_{\mathbf{k}}$ is TR odd. The Majorana surface state is spin polarized and can thus be detected by its special contribution to the spin relaxation of an electron on the surface of ^{3}He-B, similar to the measurement of electron spin correlation in a solid state system by nuclear magnetic resonance (Chung and Zhang, 2009; Shindou *et al.*, 2010). The measurement proposed by Chung and Zhang (2009) is illustrated in Fig. 42.

B. Topological invariants

From the discussion above, we see that the model Hamiltonian for the topological superconductor is the same as that for the topological insulator, but with the additional particle-hole symmetry. The simultaneous presence of both TR and particle-hole symmetry gives a different classification for the 2D and 3D topological superconductors, in that the 3D TR invariant topological superconductors are classified by integer ($\mathbb{Z}$) classes, and the 2D TR invariant topological superconductors are classified by the $\mathbb{Z}_2$ classes. To define an integer-valued topological invariant (Schnyder *et al.*,

2008), we start from a generic mean-field BdG Hamiltonian for a 3D TR invariant superconductor, which can be written in momentum space as

$$H = \sum_{\mathbf{k}} [\psi_{\mathbf{k}}^\dagger h_{\mathbf{k}} \psi_{\mathbf{k}} + 1/2(\psi_{\mathbf{k}}^\dagger \Delta_{\mathbf{k}} \psi_{-\mathbf{k}}^{\dagger T} + \text{H.c.})].$$

In a different basis we have $H = \sum_{\mathbf{k}} \Psi_{\mathbf{k}}^\dagger H_{\mathbf{k}} \Psi_{\mathbf{k}}$ with

$$\Psi_{\mathbf{k}} = \frac{1}{\sqrt{2}} \begin{pmatrix} \psi_{\mathbf{k}} - i\mathcal{T}\psi_{-\mathbf{k}}^\dagger \\ \psi_{\mathbf{k}} + i\mathcal{T}\psi_{-\mathbf{k}}^\dagger \end{pmatrix},$$
$$H_{\mathbf{k}} = \frac{1}{2} \begin{pmatrix} 0 & h_{\mathbf{k}} + i\mathcal{T}\Delta_{\mathbf{k}}^\dagger \\ h_{\mathbf{k}} - i\mathcal{T}\Delta_{\mathbf{k}}^\dagger & 0 \end{pmatrix}. \tag{95}$$

In general, $\psi_{\mathbf{k}}$ is a vector with N components, and $h_{\mathbf{k}}$ and $\Delta_{\mathbf{k}}$ are $N \times N$ matrices. The matrix $\mathcal{T}$ is the TR matrix satisfying $\mathcal{T}^\dagger h_{\mathbf{k}} \mathcal{T} = h_{-\mathbf{k}}^T$, $\mathcal{T}^2 = -\mathbb{I}$, and $\mathcal{T}^\dagger \mathcal{T} = \mathbb{I}$, with $\mathbb{I}$ the identity matrix. We have chosen a special basis in which the BdG Hamiltonian $H_{\mathbf{k}}$ has a special off-diagonal form. It should be noted that such a choice is possible only when the system has both TR symmetry and particle-hole symmetry. These two symmetries also require $\mathcal{T}\Delta_{\mathbf{k}}^\dagger$ to be Hermitian, which makes the matrix $h_{\mathbf{k}} + i\mathcal{T}\Delta_{\mathbf{k}}^\dagger$ generically non-Hermitian. The matrix $h_{\mathbf{k}} + i\mathcal{T}\Delta_{\mathbf{k}}^\dagger$ can be decomposed by a singular value decomposition as $h_{\mathbf{k}} + i\mathcal{T}\Delta_{\mathbf{k}}^\dagger = U_{\mathbf{k}}^\dagger D_{\mathbf{k}} V_{\mathbf{k}}$ with $U_{\mathbf{k}}$ and $V_{\mathbf{k}}$ unitary matrices and $D_{\mathbf{k}}$ a diagonal matrix with non-negative elements. One can see that the diagonal elements of $D_{\mathbf{k}}$ are actually the positive eigenvalues of $H_{\mathbf{k}}$. For a fully gapped superconductor, $D_{\mathbf{k}}$ is positive definite, and we can adiabatically deform it to the identity matrix $\mathbb{I}$ without closing the superconducting gap. During this deformation, the matrix $h_{\mathbf{k}} + i\mathcal{T}\Delta_{\mathbf{k}}^\dagger$ is deformed to a unitary matrix $Q_{\mathbf{k}} = U_{\mathbf{k}}^\dagger V_{\mathbf{k}} \in U(N)$. The integer-valued topological invariant characterizing topological superconductors is defined as the winding number of $Q_{\mathbf{k}}$ (Schnyder *et al.*, 2008)

$$N_W = \frac{1}{24\pi^2} \int d^3k \epsilon^{ijk} \text{Tr}[Q_{\mathbf{k}}^\dagger \partial_i Q_{\mathbf{k}} Q_{\mathbf{k}}^\dagger \partial_j Q_{\mathbf{k}} Q_{\mathbf{k}}^\dagger \partial_k Q_{\mathbf{k}}]. \tag{96}$$

We note that the topological invariant (96) is expressed as an integral over the entire Brillouin zone, similar to its counterpart for topological insulators. However, there is a key difference. Whereas the insulating gap is well defined over the entire Brillouin zone, the superconducting pairing gap in the BdG equation is only well defined close to the Fermi surface. Indeed, superconductivity arises from a Fermi surface instability, at least in the BCS limit. Therefore, we should define topological invariants for a topological superconductor strictly in terms of Fermi surface quantities. The desired topological invariant can be obtained by reducing the winding number in Eq. (96) to an integral over the Fermi surface (Qi, Hughes, and Zhang, 2010b)

$$N_W = \frac{1}{2} \sum_s \text{sgn}(\delta_s) C_{1s}, \tag{97}$$

where s is summed over all disconnected Fermi surfaces and $\text{sgn}(\delta_s)$ denotes the sign of the pairing amplitude on the sth Fermi surface. C_{1s} is the first Chern number of the sth Fermi surface (denoted by FS_s)

$$C_{1s} = \frac{1}{2\pi} \int_{\text{FS}_s} d\Omega^{ij} [\partial_i a_{sj}(\mathbf{k}) - \partial_j a_{si}(\mathbf{k})], \tag{98}$$

with $a_{si} = -i\langle s\mathbf{k}|\partial/\partial k_i|s\mathbf{k}\rangle$ the adiabatic connection defined for the band $|s\mathbf{k}\rangle$ which crosses the Fermi surface, and $d\Omega^{ij}$ the surface element two-form of the Fermi surface.

As an example, we consider a two-band model with non-interacting Hamiltonian $h_{\mathbf{k}} = \mathbf{k}^2/2m - \mu + \alpha \mathbf{k} \cdot \sigma$, for which there are two Fermi surfaces with opposite Chern number $C_\pm = \pm 1$ [Figs. 43(a) and 43(b)]. If we choose $\Delta_{\mathbf{k}} = i\Delta_0 \sigma^y$, which has the same δ_s for both Fermi surfaces, we obtain $N_W = 0$ [Fig. 43(b)]. If we instead choose $\Delta_{\mathbf{k}} = i\Delta_0 \sigma^y \sigma \cdot \mathbf{k}$, we obtain $N_W = 1$ [Fig. 43(a)]. In the latter case, if we take the $\alpha \to 0$ limit, we arrive at the result $N_W = 1$ for the ^{3}He-B phase, which indicates that ^{3}He-B is topologically nontrivial (Volovik, 2003).

For 2D TR invariant superconductors, a procedure of dimensional reduction leads to the following simple Fermi surface topological invariant:

$$N_{2D} = \prod_s [\text{sgn}(\delta_s)]^{m_s} \tag{99}$$

The criterion (99) is quite simple: A 2D TR invariant superconductor is topologically nontrivial (trivial) if there is an odd (even) number of Fermi surfaces, each of which encloses one TR invariant point in the Brillouin zone and has negative pairing. As an example, see Fig. 43(c), where Fermi surfaces 2 and 3 have negative pairing. Fermi surfaces 3 and 4 enclose an even number of TR invariant momenta, which do not affect the $\mathbb{Z}_2$ topological invariant. There is only one Fermi surface, surface 2, which encloses an odd number of TR invariant momenta and has negative pairing. As a result, the $\mathbb{Z}_2$ topological invariant is $(-1)^1 = -1$.

For 1D TR invariant superconductors, a further dimensional reduction can be carried out to give

$$N_{1D} = \prod_s [\text{sgn}(\delta_s)], \tag{100}$$

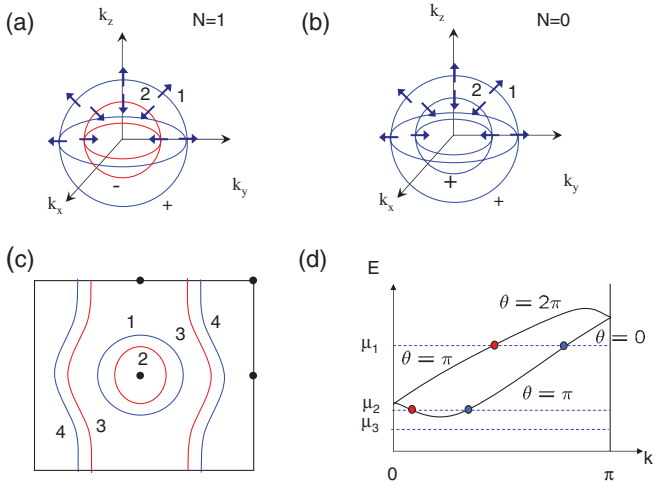

FIG. 43 (color). (a), (b) Superconducting pairing on two Fermi surfaces of a 3D superconductor. (c) An example of 2D TR invariant topological superconductor. (d) 1D TR invariant topological superconductor. Adapted from Qi, Hughes, and Zhang, 2010b.

where s is summed over all the Fermi points between 0 and π. In geometrical terms, a 1D TR invariant superconductor is nontrivial (trivial) if there is an odd number of Fermi points between 0 and π with negative pairing. We illustrate this formula in Fig. 43(d), where the sign of pairing on the red (blue) Fermi point is -1 ($+1$), so that the number of Fermi points with negative pairing is 1 if the chemical potential $\mu = \mu_1$ or $\mu = \mu_2$, and 0 if $\mu = \mu_3$. The superconducting states with $\mu = \mu_1$ and $\mu = \mu_2$ can be adiabatically deformed to each other without closing the gap. However, the superconductor with $\mu = \mu_3$ can be obtained only from that with μ_2 through a topological phase transition, where the pairing-order parameter changes sign on one of the Fermi points. It is easy to see from this example that there are two classes of 1D TR invariant superconductors.

Alternative formulas for the topological invariant of TR invariant topological superconductors have been proposed for inversion-symmetric systems (Sato, 2009; Fu and Berg, 2010; Sato, 2010).

C. Majorana zero modes in topological superconductors

1. Majorana zero modes in $p + ip$ superconductors

Besides the new TR invariant topological superconductors, the TR breaking topological superconductors have attracted a lot of interest because of their relevance to non-Abelian statistics and topological quantum computation. In a $p + ip$ superconductor described by Eq. (88), it can be shown that the core of a superconducting vortex contains a localized quasiparticle with exactly zero energy (Volovik, 1999). The corresponding quasiparticle operator γ is a Majorana fermion obeying $[\gamma, H] = 0$ and $\gamma^\dagger = \gamma$. When two vortices wind around each other, the two Majorana fermions γ_1 and γ_2 in their cores transform nontrivially. Because the phase of the charge-$2e$ order parameter winds by 2π around each vortex, an electron acquires a Berry phase of π when winding once around a vortex. Since the Majorana fermion operator is a superposition of electron creation and annihilation operators, it also acquires a π phase shift, i.e., a minus sign when winding around another vortex. Consequently, when two vortices are exchanged, the Majorana operators γ_1 and γ_2 must transform as $\gamma_1 \to \gamma_2$ and $\gamma_2 \to -\gamma_1$. The additional minus sign may be associated with γ_1 or γ_2, but not both, so that after a full winding we have $\gamma_{1(2)} \to -\gamma_{1(2)}$. Since two Majorana fermions γ_1 and γ_2 define one complex fermion operator $\gamma_1 + i\gamma_2$, the two vortices actually share two internal states labeled by $i\gamma_1\gamma_2 = \pm 1$. When there are $2N$ vortices in the system, the core states span a 2^N-dimensional Hilbert space. The braiding of vortices leads to non-Abelian unitary transformations in this Hilbert space, implying that the vortices in this system obey non-Abelian statistics (Read and Green, 2000; Ivanov, 2001). Because the internal states of the vortices are not localized on each vortex but shared in a nonlocal fashion between the vortices, the coupling of the internal state to the environment is exponentially small. As a result, the superposition of different internal states is immune to decoherence, which is ideal for the purpose of quantum computation. Quantum computation with topologically protected qubits is generally known as a topological quantum computation and is currently an active field of research (Nayak *et al.*, 2008).

Several experimental candidates for p-wave superconductivity have been proposed, among them Sr_2RuO_4, which is considered as the most promising candidate for 2D chiral superconductivity (Mackenzie and Maeno, 2003). However, many properties of this system remain unclear, such as whether this superconducting phase is gapped and whether there are gapless edge states.

Fortunately, there is an alternate route toward topological superconductivity without p-wave pairing. Jackiw and Rossi (1981) showed that adding a Majorana mass term to a single flavor of massless Dirac fermions in $(2 + 1)$D would lead to a Majorana zero mode in the vortex core. Such a Majorana mass term can be naturally interpreted as the pairing field due to the proximity coupling to a conventional s-wave superconductor. There are now three different proposals to realize this route toward topological superconductivity: the superconducting proximity effect on the 2D surface state of the 3D topological insulator (Fu and Kane, 2008), on the 2D TR breaking topological insulator (Qi, Hughes, and Zhang, 2010a), and on cold atom systems (Sato *et al.*, 2009) or semiconductors (Sau *et al.*, 2010) with strong Rashba SOC. We review these three proposals in the following.

2. Majorana fermions in surface states of the topological insulator

Fu and Kane (2008) proposed a way to realize the Majorana zero mode in a superconducting vortex core by making use of the surface states of 3D topological insulators. Consider a topological insulator such as Bi_2Se_3, which has a single Dirac cone on the surface with Hamiltonian from Eq. (34)

$$H = \sum_{\mathbf{p}} \psi_{\mathbf{p}}^\dagger [v(\boldsymbol{\sigma} \times \mathbf{p}) \cdot \hat{\mathbf{z}} - \mu] \psi_{\mathbf{p}}, \tag{101}$$

where $\psi_{\mathbf{p}} = (\psi_{\mathbf{p}\uparrow}, \psi_{\mathbf{p}\downarrow})^T$ and we have taken into account a finite chemical potential μ. Consider now the superconducting proximity effect of a conventional s-wave superconductor on the 2D surface states, which leads to the pairing term $H_\Delta = \Delta \psi_{\mathbf{p}}^\dagger \psi_{-\mathbf{p}}^\dagger + \text{H.c.}$ The BdG Hamiltonian is given by $H_{\text{BdG}} = \frac{1}{2}\sum_{\mathbf{p}} \Psi_{\mathbf{p}}^\dagger H_{\mathbf{p}} \Psi_{\mathbf{p}}$, where

$$\Psi_{\mathbf{p}}^\dagger \equiv \begin{pmatrix} \psi_{\mathbf{p}}^\dagger & i\sigma_y \psi_{-\mathbf{p}} \end{pmatrix}$$

and

$$H_{\mathbf{p}} \equiv \begin{pmatrix} v(\boldsymbol{\sigma} \times \mathbf{p}) \cdot \hat{\mathbf{z}} - \mu & \Delta \\ \Delta^* & -v(\boldsymbol{\sigma} \times \mathbf{p}) \cdot \hat{\mathbf{z}} + \mu \end{pmatrix}.$$

The vortex core of such a superconductor has been shown to have a single Majorana zero mode, similar to a $p + ip$ superconductor (Jackiw and Rossi, 1981; Fu and Kane, 2008). To understand this phenomenon, one can consider the case of finite μ, and introduce a TR breaking mass term $m\sigma^z$ in the surface-state Hamiltonian (101). As discussed in Sec. III.B, this opens a gap of magnitude $|m|$ on the surface. Considering the case $0 < \Delta \ll \mu - m \ll m$, the Fermi level in the normal state lies near the bottom of the parabolic dispersion, and we can consider a "nonrelativistic approximation" to the massive Dirac Hamiltonian

$$H = \sum_{\mathbf{p}} \psi^\dagger [v(\boldsymbol{\sigma} \times \mathbf{p}) \cdot \hat{\mathbf{z}} + m\sigma^z - \mu]\psi$$
$$\simeq \int d^2x \psi_+^\dagger \left(\frac{\mathbf{p}^2}{2m} + m - \mu\right)\psi_+, \quad (102)$$

where ψ_+ is the positive energy branch of the surface states. In momentum space, $\psi_{+\mathbf{p}} = u_{\mathbf{p}}\psi_\uparrow + v_{\mathbf{p}}\psi_\downarrow$ with

$$u_{\mathbf{p}} = \sqrt{\frac{1}{2} + \frac{m}{2\sqrt{\mathbf{p}^2 + m^2}}}$$

and

$$v_{\mathbf{p}} = \frac{ip_-}{|\mathbf{p}|}\sqrt{\frac{1}{2} - \frac{m}{2\sqrt{\mathbf{p}^2 + m^2}}},$$

with $p_- = p_x - ip_y$. Considering the projection of the pairing term H_Δ onto the ψ_+ band, we obtain

$$H_\Delta \simeq \sum_{\mathbf{p}} \psi^\dagger_{+,\mathbf{p}} \psi^\dagger_{+,-\mathbf{p}} \Delta u_{\mathbf{p}} v_{\mathbf{p}} + \text{H.c.}$$
$$\simeq \sum_{\mathbf{p}} \frac{ip_-\Delta}{2m} \psi^\dagger_{+,\mathbf{p}} \psi^\dagger_{+,-\mathbf{p}} + \text{H.c.} \quad (103)$$

We see that in this limit the surface Hamiltonian is the same as that of a spinless $p + ip$ superconductor [Eq. (88)]. When the mass m is turned on from zero to a finite value, it can be shown that as long as $\Delta \ll \mu - m$, $m < \mu$ the superconducting gap near the Fermi surface remains finite, so that the Majorana zero mode we obtained in the limit $0 < \Delta \ll \mu - m \ll m$ must remain at zero energy for the original $m = 0$ system. Once we have shown the existence of a Majorana zero mode at finite μ, taking the $\mu \to 0$ limit for a finite Δ also leaves the superconducting gap open, so that the Majorana zero mode is still present at $\mu = 0$.

From the analogy with the $p + ip$ superconductor shown above, we also see that the non-Abelian statistics of vortices with Majorana zero modes apply to this new system as well. A key difference between this system and a chiral $p + ip$ superconductor is that the latter necessarily breaks TR symmetry while the former can be TR invariant. Only a conventional s-wave superconductor is required to generate the Majorana zero modes in this proposal and in the other proposals discussed in the following section. This is an important advantage compared to previous proposals requiring an unconventional $p + ip$ pairing mechanism.

There is also a lower-dimensional analog of this nontrivial surface-state superconductivity. When the edge states of the 2D QSH insulator are in proximity with an s-wave superconductor and a ferromagnetic insulator, one Majorana fermion appears at each domain wall between the ferromagnetic region and the superconducting region (Fu and Kane, 2009a). The Majorana fermion in this system can move only along the 1D QSH edge, so that non-Abelian statistics is not well defined. Because an electron cannot be backscattered on the QSH edge, the scattering of the edge electron by a superconducting region induced by the proximity effect is always perfect Andreev reflection (Adroguer *et al.*, 2010; Guigou and Cayssol, 2010; Sato, Loss, and Tserkovnyak, 2010).

3. Majorana fermions in semiconductors with Rashba spin-orbit coupling

From the above analysis, we see that conventional s pairing in the surface Hamiltonian (101) induces topologically nontrivial superconductivity with Majorana fermions. There is a 2D system which is described by a Hamiltonian very similar to Eq. (101), i.e., a 2D electron gas with Rashba SOC. The Hamiltonian is $H = \int d^2x \psi^\dagger [\mathbf{p}^2/2m + \alpha(\boldsymbol{\sigma} \times \mathbf{p}) \cdot \hat{\mathbf{z}} - \mu]\psi$, which differs from the surface-state Hamiltonian only by the spin-independent term $\mathbf{p}^2/2m$. Consequently, when conventional s-wave pairing is introduced, each of the two spin-split Fermi surfaces forms a nontrivial superconductor. However, the Majorana fermions from these two Fermi surfaces annihilate each other so that the s-wave superconductor in the Rashba system is trivial. It was pointed out recently (Sato *et al.*, 2009; Sau *et al.*, 2010; Sato, Takahashi, and Fujimoto, 2010) that a nontrivial superconducting phase can be obtained by introducing a TR breaking term $M\sigma^z$ into the Hamiltonian, which splits the degeneracy near $\mathbf{k} = 0$. If the chemical potential is tuned to $|\mu| < |M|$, the inner Fermi surface disappears. Therefore, superconductivity is induced only by pairing on the outer Fermi surface and becomes topologically nontrivial. Physically, one cannot induce a TR breaking mass term by applying a magnetic field in the perpendicular direction, because the magnetic field may destroy superconductivity. Two ways to realize a TR breaking mass term have been proposed: by applying an in-plane magnetic field and making use of the Dresselhaus SOC (Alicea, 2010), or by exchange coupling to a ferromagnetic insulating layer (Sau *et al.*, 2010). The latter proposal requires a heterostructure consisting of a superconductor, a 2D electron gas with Rashba SOC, and a magnetic insulator.

This mechanism can also be generalized to the 1D semiconductor wires with Rashba SOC coupling in proximity with a superconductor (Lutchyn *et al.*, 2010, 2011; Oreg *et al.*, 2010; Potter and Lee, 2010). Despite the 1D nature of the wires, non-Abelian statistics is still possible by making use of wire networks (Alicea *et al.*, 2011).

4. Majorana fermions in quantum Hall and quantum anomalous Hall insulators

More recently, a new approach to realize a topological superconductor phase has been proposed (Qi, Hughes, and Zhang, 2010a), which is based on the proximity effect to a 2D QH or QAH insulator. Integer QH states are classified by an integer N corresponding to the first Chern number in momentum space and equal to the Hall conductance in units of e^2/h. Consider a QH insulator with Hall conductance Ne^2/h in close proximity to a superconductor. Even if the pairing strength induced by the superconducting proximity effect is infinitesimally small, the resulting state is topologically equivalent to a chiral topological superconductor with $\mathbb{Z}$ topological quantum number $\mathcal{N} = 2N$. An intuitive way to understand such a relation between QH and topological superconducting phases is through the evolution of the edge states. The edge state of a QH state with Chern number $N = 1$ is described by the effective 1D Hamiltonian $H_{\text{edge}} = \sum_{p_y} v p_y \eta^\dagger_{p_y} \eta_{p_y}$, where $\eta^\dagger_{p_y}$ and η_{p_y} are creation and

annihilation operators for a complex spinless fermion. We can decompose η_{p_y} into its real and imaginary parts, $\eta_{p_y} = (1/\sqrt{2})(\gamma_{p_y 1} + i\gamma_{p_y 2})$ and $\eta^\dagger_{p_y} = (1/\sqrt{2})(\gamma_{-p_y 1} - i\gamma_{-p_y 2})$, where $\gamma_{p_y a}$ are Majorana fermion operators satisfying $\gamma^\dagger_{p_y a} = \gamma_{-p_y a}$ and $\{\gamma_{-p_y a}, \gamma_{p'_y b}\} = \delta_{ab}\delta_{p_y p'_y}$. The edge Hamiltonian becomes

$$H_{\text{edge}} = \sum_{p_y \geq 0} p_y(\gamma_{-p_y 1}\gamma_{p_y 1} + \gamma_{-p_y 2}\gamma_{p_y 2}), \tag{104}$$

up to a trivial shift of the energy. In comparison with the edge theory of the chiral topological superconducting state, the QH edge state can be considered as two identical copies of chiral Majorana fermions, so that the QH phase with Chern number $N = 1$ can be considered as a chiral topological superconducting state with Chern number $\mathcal{N} = 2$, even for infinitesimal pairing amplitudes.

An important consequence of such a relation between QH and topological superconducting phases is that the QH plateau transition from $N = 1$ to $N = 0$ will generically split into two transitions when superconducting pairing is introduced. Between the two transitions, there will be a new topological superconducting phase with odd winding number $\mathcal{N} = 1$ (Fig. 44). Compared to other approaches, the emergence of the topological superconducting phase at a QH plateau transition is determined topologically, so that this approach does not depend on any fine-tuning or details of the theory.

A natural concern raised by this approach is that the strong magnetic field usually required for QH states can suppress superconductivity. The solution to this problem can be found in a special type of QH state, the QAH state, which is a TR breaking gapped state with nonzero Hall conductance in the absence of an external orbital magnetic field (see Sec. II.E). There exist now two proposals for realizing the QAH state experimentally, both of which make use of the TR invariant topological insulator materials Mn-doped HgTe QWs (Liu, Hughes *et al.*, 2008) and Cr- or Fe-doped Bi_2Se_3 thin films (Yu *et al.*, 2010). The latter material is proposed to be ferromagnetic and can thus exhibit a quantized Hall conductance at zero magnetic field. The former material is known to be paramagnetic for low Mn concentrations, but only a small magnetic field is needed to polarize the Mn spins and drive the system into a QAH phase. This requirement is not so prohibitive, because a nonzero magnetic field is already necessary to generate superconducting vortices and the associated Majorana zero modes.

Besides the proposals reviewed above, some other proposals on the realization of Majorana fermions in nonconventional superconductors have also been studied (Sato and Fujimoto, 2009, 2010; Wimmer *et al.*, 2010; Mao *et al.*, 2011).

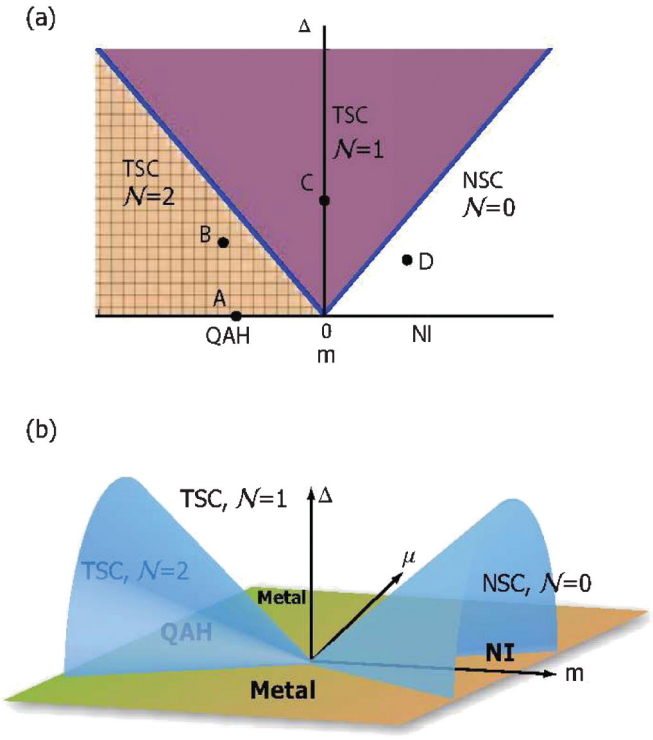

FIG. 44 (color). (a) Phase diagram of the QAH-superconductor hybrid system for $\mu = 0$. m is the mass parameter, Δ is the magnitude of the superconducting gap, and $\mathcal{N}$ is the Chern number of the superconductor, which is equal to the number of chiral Majorana edge modes. (b) Phase diagram for finite μ, shown only for $\Delta \geq 0$. The QAH, normal insulator (NI), and metallic (metal) phases are well defined only for $\Delta = 0$. From Qi, Hughes, and Zhang, 2010a.

5. Detection of Majorana fermions

The next obvious question is how to detect the Majorana fermion if such a proposal is experimentally realized. Two similar theoretical proposals of electrical transport measurements exist to detect these Majorana fermions (Akhmerov, Nilsson, and Beenakker, 2009; Fu and Kane, 2009b). Consider the geometry shown in Fig. 45. This device is a combination of the inhomogeneous structures on the surface of a topological insulator discussed in the previous sections. The input and output of the circuit consist of a chiral fermion coming from a domain wall between two ferromagnets. This chiral fermion is incident on a superconducting region where it splits into two chiral Majorana fermions. The chiral Majorana fermions then recombine into an outgoing electron or hole after traveling around the superconducting island. More explicitly, an electron incident from the source can be transmitted to the drain as an electron, or converted to a hole by an Andreev process in which charge $2e$ is absorbed into the superconducting condensate. To illustrate the idea we discuss the behavior for a $E = 0$ quasiparticle (Fu and Kane, 2009b). A chiral fermion incident at point a meets the superconductor and evolves from an electron $c^\dagger_a$ into a fermion ψ built from the Majorana operators γ_1 and γ_2. The arbitrariness in the sign of $\gamma_{1,2}$ allows us to choose $\psi = \gamma_1 + i\gamma_2$. After the quasiparticle winds around the superconducting region, ψ recombines into a complex fermion at point d. This fermion must be either $c^\dagger_d$ or c_d, since a superposition of the two is not a fermion operator and is thus forbidden. To determine the correct operator we can use adiabatic continuity. When the size of the superconductor shrinks continuously to zero, points a and d continuously tend to each other. Adiabatic continuity implies that an

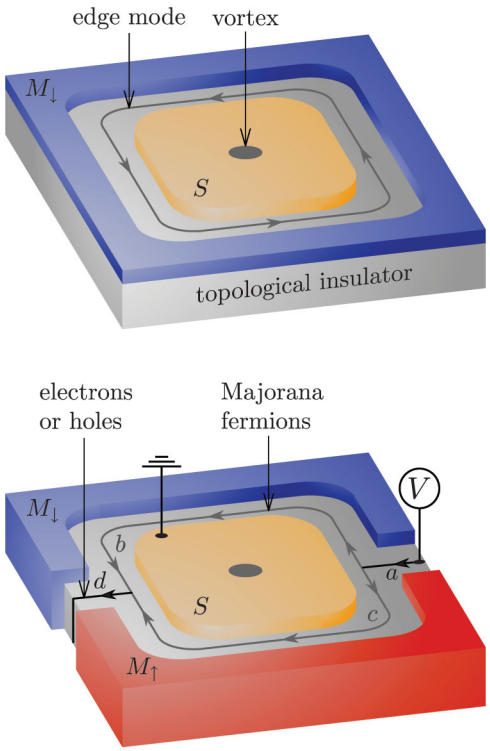

FIG. 45 (color). 3D topological insulator in proximity to ferromagnets with opposite polarization ($M_\uparrow$ and $M_\downarrow$) and to a superconductor (S). The top panel shows a single chiral Majorana mode along the edge between superconductor and ferromagnet. This mode is electrically neutral and therefore cannot be detected electrically. The Mach-Zehnder interferometer in the bottom panel converts a charged current along the domain wall into a neutral current along the superconductor (and vice versa). This allows electrical detection of the parity of the number of enclosed vortices per flux quanta. From Akhmerov, Nilsson, and Beenakker, 2009.

incident $E = 0$ electron is transmitted as an electron, $c_a^\dagger \rightarrow c_d^\dagger$. However, if the ring encloses a quantized flux $\Phi = nhc/2e$, this adiabatic argument must be reconsidered. When n is an odd integer, the two Majorana fermions acquire an additional relative phase of π, since each flux quantum $hc/2e$ is a π flux for an electron, and thus π for a Majorana fermion. Up to an overall sign, one can take $\gamma_1 \rightarrow -\gamma_1$ and $\gamma_2 \rightarrow \gamma_2$. Thus, when the ring encloses an odd number of flux quanta, $c_a^\dagger \rightarrow c_d$, and an incident $E = 0$ electron is converted to a hole. The general consequences of this were calculated in detail (Akhmerov, Nilsson, and Beenakker, 2009; Fu and Kane, 2009b), and it was shown that the output current (through arm d in the lower panel of Fig. 45) changes sign when the number of flux quanta in the ring jumps between odd and even. This unique behavior of the current provides a way to electrically detect Majorana fermions.

Besides these two proposals reviewed above, several other theoretical proposals have also been made recently to observe the Majorana fermion state, which make use of the Coulomb charging energy (Fu, 2010), interference (Benjamin and Pachos, 2010), or a flux qubit (Hassler *et al.*, 2010). More indirectly, Majorana fermions can also be detected through their contribution to Josephson coupling (Fu and Kane, 2008, 2009a; Tanaka *et al.*, 2009; Linder and Sudbo, 2010; Lutchyn *et al.*, 2010; Linder *et al.*, 2010a, 2010b). For a topological superconductor ring with Majorana fermions at both ends, the period of Josephson current is doubled, independent from the physical realization (Kitaev, 2001; Fu and Kane, 2009a; Lutchyn *et al.*, 2010).

VI. OUTLOOK

The subject of topological insulators and superconductors is now one of the most active fields of research in condensed matter physics, developing at a rapid pace. Theorists have systematically classified topological states in all dimensions. Qi, Hughes, and Zhang (2008b) initiated the classification program of all topological insulators according to discrete particle-hole symmetry and the TR symmetry and noticed a periodic structure with period eight, which is known in mathematics as the Bott periodicity. More extended and systematic classification of all topological insulator and superconductor states is obtained according to TR, particle-hole, and bipartite symmetries (Schnyder *et al.*, 2008; Qi, Hughes, and Zhang, 2008b; Kitaev, 2009; Ryu, Schnyder *et al.*, 2010; Stone *et al.*, 2011). Such a classification scheme gives a "periodic table" of topological states, which may play a similar role as the familiar periodic table of elements. For future progress on the theoretical side, important outstanding problems include interaction and disorder effects, realistic predictions for topological Mott insulator materials, a deeper understanding of fractional topological insulators and realistic predictions for material realizations of such states, the effective field theory description of the topological superconducting state, and realistic material predictions for topological superconductors. On the experimental side, the most important task is to grow materials with sufficient purity so that the bulk insulating behavior can be reached, and to tune the Fermi level close to the Dirac point of the surface state. Hybrid structures between topological insulators and magnetic and superconducting states will be intensively investigated, with a focus on detecting exotic emergent particles such as the image magnetic monopole, the axion, and the Majorana fermion. The theoretical prediction of the QAH state is sufficiently realistic and its experimental discovery appears to be imminent. The topological quantization of the TME effect in 3D and the spin-charge separation effect in 2D could experimentally determine the topological order parameter of this novel state of matter.

Because of space limitations, we did not discuss in detail the potential for applications of topological insulators and superconductors. It would be interesting to explore the possibility of electronic devices with low power consumption based on the dissipationless edge channels of the QSH state, spintronics devices based on the unique current-spin relationship in the topological surface states, infrared detectors, and thermoelectric applications. Topological quantum computers based on Majorana fermions remain an inspiration in the field.

Topological insulators and superconductors offer a platform to test many novel ideas in particle physics, a "baby universe" where the mysterious θ vacuum is realized, where exotic particles roam freely, and where compactified extra dimensions can be tested experimentally. In the Introduction

we drew an analogy between the search for new states of matter and the discovery of elementary particles. Up to now, the most important states of quantum matter were first discovered empirically and often serendipitously. On the other hand, the Einstein-Dirac approach has been successful in searching for the fundamental laws of nature: logical reasoning and mathematical equations guided and predicted subsequent experimental discoveries. The success of theoretical predictions in the field of topological insulators shows that this powerful approach works equally well in condensed matter physics, inspiring many more examples to come.

ACKNOWLEDGMENTS

We are grateful to Taylor L. Hughes, Chao-Xing Liu, Joseph Maciejko, Jing Wang, and Zhong Wang for their invaluable input which made the current manuscript possible. We thank Andrei Bernevig, Hartmut Buhmann, Yulin Chen, Suk Bum Chung, Yi Cui, Xi Dai, Dennis Drew, Zhong Fang, Aharon Kapitulnik, Andreas Karch, Laurens Molenkamp, Naoto Nagaosa, S. Raghu, Zhi-Xun Shen, Cenke Xu, Qikun Xue, and Haijun Zhang for their close collaboration and for their important contributions reviewed in this paper. We benefitted greatly from the discussions with colleagues Leon Balents, Mac Beasley, Carlo Beenakker, Marcel Franz, Liang Fu, David Goldhaber-Gordon, Zahid Hasan, Charlie Kane, Alexei Kitaev, Steve Kivelson, Andreas Ludwig, Joel Moore, Phuan Ong, Rahul Roy, Shinsei Ryu, Ali Yazdani, and Jan Zaanen. This work is supported by the Department of Energy, Office of Basic Energy Sciences, Division of Materials Sciences and Engineering, under Contract No. DE-AC02-76SF00515, the NSF under Grant No. DMR-0904264, the ARO under Grant No. W911NF-09-1-0508, and the Keck Foundation.

REFERENCES

Abrahams, E., P. W. Anderson, D. C. Licciardello, and T. V. Ramakrishnan, 1979, Phys. Rev. Lett. **42**, 673.
Adroguer, P., C. Grenier, D. Carpentier, J. Cayssol, P. Degiovanni, and E. Orignac, 2010, Phys. Rev. B **82**, 081303.
Akhmerov, A. R., C. W. Groth, J. Tworzydło, and C. W. J. Beenakker, 2009, Phys. Rev. B **80**, 195320.
Akhmerov, A. R., J. Nilsson, and C. W. J. Beenakker, 2009, Phys. Rev. Lett. **102**, 216404.
Alicea, J., 2010, Phys. Rev. B **81**, 125318.
Alicea, J., Y. Oreg, G. Refael, F. von Oppen, and M. P. A. Fisher, 2011, Nature Phys. **7**, 412.
Alpichshev, Z., J. G. Analytis, J. H. Chu, I. R. Fisher, Y. L. Chen, Z. X. Shen, A. Fang, and A. Kapitulnik, 2010, Phys. Rev. Lett. **104**, 016401.
Alpichshev, Z., J. G. Analytis, J. H. Chu, I. R. Fisher, and A. Kapitulnik, 2010, arXiv:1003.2233.
Analytis, J. G., J. H. Chu, Y. L. Chen, F. Corredor, R. D. McDonald, Z. X. Shen, and I. R. Fisher, 2010, Phys. Rev. B **81**, 205407.
Analytis, J. G., R. D. McDonald, S. C. Riggs, J. H. Chu, G. S. Boebinger, and I. R. Fisher, 2010, Nature Phys. **6**, 960.
Anderson, P. W., 1997, *Basic Notions of Condensed Matter Physics* (Westview Press, Boulder, CO).
Asano, Y., Y. Tanaka, and N. Nagaosa, 2010, Phys. Rev. Lett. **105**, 056402.
Ayala-Valenzuela, O. E., J. G. Analytis, J. H. Chu, M. M. Altarawneh, I. R. Fisher, and R. D. McDonald, 2010, arXiv:1004.2311.
Bardarson, J. H., P. W. Brouwer, and J. E. Moore, 2010, Phys. Rev. Lett. **105**, 156803.
Beenakker, C. W. J., and H. van Houten, 1991, Solid State Phys. **44**, 1.
Benjamin, C., and J. K. Pachos, 2010, Phys. Rev. B **81**, 085101.
Bercioux, D., N. Goldman, and D. Urban, 2011, Phys. Rev. A **83**, 023609.
Béri, B., 2010, Phys. Rev. B **81**, 134515.
Bermudez, A., N. Goldman, A. Kubasiak, M. Lewenstein, and M. Martin-Delgado, 2010, New J. Phys. **12**, 033041.
Bermudez, A., L. Mazza, M. Rizzi, N. Goldman, M. Lewenstein, and M. A. Martin-Delgado, 2010, Phys. Rev. Lett. **105**, 190404.
Bermudez, A., D. Patane, L. Amico, and M. A. Martin-Delgado, 2009, Phys. Rev. Lett. **102**, 135702.
Bernevig, B. A., C. H. Chern, J. P. Hu, N. Toumbas, and S. C. Zhang, 2002, Ann. Phys. (N.Y.) **300**, 185.
Bernevig, B. A., T. L. Hughes, and S. C. Zhang, 2006, Science **314**, 1757.
Bernevig, B. A., and S. C. Zhang, 2006, Phys. Rev. Lett. **96**, 106802.
Biswas, R. R., and A. V. Balatsky, 2010, arXiv:1005.4780.
Burkov, A. A., and D. G. Hawthorn, 2010, Phys. Rev. Lett. **105**, 066802.
Butch, N. P., K. Kirshenbaum, P. Syers, A. B. Sushkov, G. S. Jenkins, H. D. Drew, and J. Paglione, 2010, Phys. Rev. B **81**, 241301.
Büttiker, M., 1986, Phys. Rev. Lett. **57**, 1761.
Büttiker, M., 1988, Phys. Rev. B **38**, 9375.
Büttiker, M., 2009, Science **325**, 278.
Castro Neto, A. H., F. Guinea, N. M. R. Peres, K. S. Novoselov, and A. K. Geim, 2009, Rev. Mod. Phys. **81**, 109.
Cha, J. J., J. R. Williams, D. Kong, S. Meister, H. Peng, A. J. Bestwick, P. Gallagher, D. Goldhaber-Gordon, and Y. Cui, 2010, Nano Lett. **10**, 1076.
Chadov, S., X. L. Qi, J. Kübler, G. H. Fecher, C. Felser, and S. C. Zhang, 2010, Nature Mater. **9**, 541.
Checkelsky, J. G., Y. S. Hor, R. J. Cava, and N. P. Ong, 2011, Phys. Rev. Lett. **106**, 196801.
Checkelsky, J. G., Y. S. Hor, M.-H. Liu, D.-X. Qu, R. J. Cava, and N. P. Ong, 2009, Phys. Rev. Lett. **103**, 246601.
Chen, J., *et al.*, 2010, Phys. Rev. Lett. **105**, 176602.
Chen, L., and S. Wan, 2010, arXiv:1005.4143.
Chen, Y. L., *et al.*, 2009, Science **325**, 178.
Chen, Y. L., *et al.*, 2010a, Science **329**, 659.
Chen, Y. L., *et al.*, 2010b, Phys. Rev. Lett. **105**, 266401.
Cheng, P., *et al.*, 2010, Phys. Rev. Lett. **105**, 076801.
Chu, R. L., J. Li, J. K. Jain, and S. Q. Shen, 2009, Phys. Rev. B **80**, 081102(R).
Chung, S. B., and S. C. Zhang, 2009, Phys. Rev. Lett. **103**, 235301.
Dai, X., T. L. Hughes, X.-L. Qi, Z. Fang, and S.-C. Zhang, 2008, Phys. Rev. B **77**, 125319.
Daumer, V., I. Golombek, M. Gbordzoe, E. G. Novik, V. Hock, C. R. Becker, H. Buhmann, and L. W. Molenkamp, 2003, Appl. Phys. Lett. **83**, 1376.
Day, C., 2008, Phys. Today **61**, 19.
Dubrovin, B. A., A. T. Fomenko, and S. P. Novikov, 1985, *Modern Geometry—Methods and Applications, Part 2: The Geometry and Topology of Manifolds* (Springer, New York).
Dzero, M., K. Sun, V. Galitski, and P. Coleman, 2010, Phys. Rev. Lett. **104**, 106408.
Essin, A. M., and J. E. Moore, 2007, Phys. Rev. B **76**, 165307.

Essin, A. M., J. E. Moore, and D. Vanderbilt, 2009, Phys. Rev. Lett. **102**, 146805.
Essin, A. M., A. M. Turner, J. E. Moore, and D. Vanderbilt, 2010, Phys. Rev. B **81**, 205104.
Eto, K., Z. Ren, A. A. Taskin, K. Segawa, and Y. Ando, 2010, Phys. Rev. B **81**, 195309.
Evers, F., and A. D. Mirlin, 2008, Rev. Mod. Phys. **80**, 1355.
Feng, X.-Y., W.-Q. Chen, J.-H. Gao, Q.-H. Wang, and F.-C. Zhang, 2010, Phys. Rev. B **81**, 235411.
Fradkin, E., E. Dagotto, and D. Boyanovsky, 1986, Phys. Rev. Lett. **57**, 2967.
Franz, M., 2010, Nature Mater. **9**, 536.
Freedman, M., M. B. Hastings, C. Nayak, X.-L. Qi, K. Walker, and Z. Wang, 2011, Phys. Rev. B **83**, 115132.
Fröhlich, J., and B. Pedrini, 2000, hep-th/0002195.
Fu, L., 2009, Phys. Rev. Lett. **103**, 266801.
Fu, L., 2010, Phys. Rev. Lett. **104**, 056402.
Fu, L., and E. Berg, 2010, Phys. Rev. Lett. **105**, 097001.
Fu, L., and C. L. Kane, 2006, Phys. Rev. B **74**, 195312.
Fu, L., and C. L. Kane, 2007, Phys. Rev. B **76**, 045302.
Fu, L., and C. L. Kane, 2008, Phys. Rev. Lett. **100**, 096407.
Fu, L., and C. L. Kane, 2009a, Phys. Rev. B **79**, 161408.
Fu, L., and C. L. Kane, 2009b, Phys. Rev. Lett. **102**, 216403.
Fu, L., C. L. Kane, and E. J. Mele, 2007, Phys. Rev. Lett. **98**, 106803.
Fukui, T., and Y. Hatsugai, 2007, Phys. Rev. B **75**, 121403(R).
Gao, J., W. Chen, X. C. Xie, and F. C. Zhang, 2009, Phys. Rev. B **80**, 241302.
Garate, I., and M. Franz, 2010, Phys. Rev. Lett. **104**, 146802.
Giamarchi, T., 2003, *Quantum Physics in One Dimension* (Clarendon Press, Oxford).
Giamarchi, T., and H. J. Schulz, 1988, Phys. Rev. B **37**, 325.
Goldman, N., A. Kubasiak, A. Bermudez, P. Gaspard, M. Lewenstein, and M. A. Martin-Delgado, 2009, Phys. Rev. Lett. **103**, 035301.
Goldman, N., I. Satija, P. Nikolic, A. Bermudez, M. A. Martin-Delgado, M. Lewenstein, and I. B. Spielman, 2010, Phys. Rev. Lett. **105**, 255302.
Goldstone, J., and F. Wilczek, 1981, Phys. Rev. Lett. **47**, 986.
Golterman, M. F. L., K. Jansen, and D. B. Kaplan, 1993, Phys. Lett. B **301**, 219.
Gomes, K. K., W. Ko, W. Mar, Y. Chen, Z.-X. Shen, and H. C. Manoharan, 2009, arXiv:0909.0921.
Groth, C. W., M. Wimmer, A. R. Akhmerov, J. Tworzydło, and C. W. J. Beenakker, 2009, Phys. Rev. Lett. **103**, 196805.
Grushin, A. G., and A. Cortijo, 2011, Phys. Rev. Lett. **106**, 020403.
Guigou, M., and J. Cayssol, 2010, Phys. Rev. B **82**, 115312.
Guo, H. M., 2010, Phys. Rev. B **82**, 115122.
Guo, H. M., and M. Franz, 2009, Phys. Rev. Lett. **103**, 206805.
Guo, H.-M., and M. Franz, 2010, Phys. Rev. B **81**, 041102(R).
Guo, H. M., G. Rosenberg, G. Refael, and M. Franz, 2010, Phys. Rev. Lett. **105**, 216601.
Gurarie, V., 2011, Phys. Rev. B **83**, 085426.
Haldane, F. D. M., 1988, Phys. Rev. Lett. **61**, 2015.
Haldane, F. D. M., and L. Chen, 1984, Phys. Rev. Lett. **53**, 2591.
Hanaguri, T., K. Igarashi, M. Kawamura, H. Takagi, and T. Sasagawa, 2010, Phys. Rev. B **82**, 081305.
Hasan, M. Z., and C. L. Kane, 2010, Rev. Mod. Phys. **82**, 3045.
Hassler, F., A. R. Akhmerov, C.-Y. Hou, and C. W. J. Beenakker, 2010, New J. Phys. **12**, 125002.
He, H.-T., G. Wang, T. Zhang, I.-K. Sou, J.-N. Wang, H.-Z. Lu, S.-Q. Shen, and F.-C. Zhang, 2011, Phys. Rev. Lett. **106**, 166805.
Hikami, S., A. I. Larkin, and Y. Nagaoka, 1980, Prog. Theor. Phys. **63**, 707.
Hong, S. S., W. Kundhikanjana, J. J. Cha, K. Lai, D. Kong, S. Meister, M. A. Kelly, Z. Shen, and Y. Cui, 2010, Nano Lett. **10**, 3118.
Hor, Y. S., J. G. Checkelsky, D. Qu, N. P. Ong, and R. J. Cava, 2011, J. Phys. Chem. Solids **72**, 572.
Hor, Y. S., A. Richardella, P. Roushan, Y. Xia, J. G. Checkelsky, A. Yazdani, M. Z. Hasan, N. P. Ong, and R. J. Cava, 2009, Phys. Rev. B **79**, 195208.
Hor, Y. S., A. J. Williams, J. G. Checkelsky, P. Roushan, J. Seo, Q. Xu, H. W. Zandbergen, A. Yazdani, N. P. Ong, and R. J. Cava, 2010b, Phys. Rev. Lett. **104**, 057001.
Hor, Y. S., *et al.*, 2010a, Phys. Rev. B **81**, 195203.
Hou, C. Y., E. A. Kim, and C. Chamon, 2009, Phys. Rev. Lett. **102**, 076602.
Hsieh, D., D. Qian, L. Wray, Y. Xia, Y. S. Hor, R. J. Cava, and M. Z. Hasan, 2008, Nature (London) **452**, 970.
Hsieh, D., *et al.*, 2009a, Nature (London) **460**, 1101.
Hsieh, D., *et al.*, 2009b, Phys. Rev. Lett. **103**, 146401.
Hsieh, D., *et al.*, 2009c, Science **323**, 919.
Imura, K.-I., Y. Kuramoto, and K. Nomura, 2009, Phys. Rev. B **80**, 085119.
Ivanov, D. A., 2001, Phys. Rev. Lett. **86**, 268.
Jackiw, R., and C. Rebbi, 1976, Phys. Rev. D **13**, 3398.
Jackiw, R., and P. Rossi, 1981, Nucl. Phys. **B190**, 681.
Jenkins, G. S., A. B. Sushkov, D. C. Schmadel, N. P. Butch, P. Syers, J. Paglione, and H. D. Drew, 2010, Phys. Rev. B **82**, 125120.
Jiang, H., L. Wang, Q.-F. Sun, and X. C. Xie, 2009, Phys. Rev. B **80**, 165316.
Kane, C. L., 2008, Nature Phys. **4**, 348.
Kane, C. L., and E. J. Mele, 2005a, Phys. Rev. Lett. **95**, 226801.
Kane, C. L., and E. J. Mele, 2005b, Phys. Rev. Lett. **95**, 146802.
Kaplan, D. B., 1992, Phys. Lett. B **288**, 342.
Karch, A., 2009, Phys. Rev. Lett. **103**, 171601.
Kharitonov, M., 2010, arXiv:1004.0194.
King-Smith, R. D., and D. Vanderbilt, 1993, Phys. Rev. B **47**, 1651.
Kitaev, A., 2009, AIP Conf. Proc. **1134**, 22.
Kitaev, A. Y., 2001, Phys. Usp. **44**, 131.
Kivelson, S., and J. R. Schrieffer, 1982, Phys. Rev. B **25**, 6447.
Knez, I., R. R. Du, and G. Sullivan, 2010, Phys. Rev. B **81**, 201301 (R).
Kong, D., W. Dang, J. J. Cha, H. Li, S. Meister, H. Peng, Z. Liu, and Y. Cui, 2010, Nano Lett. **10**, 2245.
Kong, D., J. C. Randel, H. Peng, J. J. Cha, S. Meister, K. Lai, Y. Chen, Z.-X. Shen, H. C. Manoharan, and Y. Cui, 2010, Nano Lett. **10**, 329.
König, M., 2007, Ph.D. thesis (Universität Würzburg).
König, M., H. Buhmann, L. W. Molenkamp, T. L. Hughes, C.-X. Liu, X. L. Qi, and S. C. Zhang, 2008, J. Phys. Soc. Jpn. **77**, 031007.
König, M., S. Wiedmann, C. Brüne, A. Roth, H. Buhmann, L. Molenkamp, X.-L. Qi, and S.-C. Zhang, 2007, Science **318**, 766.
LaForge, A. D., A. Frenzel, B. C. Pursley, T. Lin, X. Liu, J. Shi, and D. N. Basov, 2010, Phys. Rev. B **81**, 125120.
Landau, L. D., and E. M. Lifshitz, 1980, *Statistical Physics* (Pergamon Press, Oxford).
Landau, L. D., and E. M. Lifshitz, 1984, *Electrodynamics of Continuous Media* (Pergamon Press, Oxford), 2nd ed.
Laughlin, R. B., 1981, Phys. Rev. B **23**, 5632.
Law, K. T., C. Y. Seng, P. A. Lee, and T. K. Ng, 2010, Phys. Rev. B **81**, 041305.
Lee, P., 2009, arXiv:0907.2681.
Lee, D.-H., 2009, Phys. Rev. Lett. **103**, 196804.
Leggett, A. J., 1975, Rev. Mod. Phys. **47**, 331.
Levin, M., and A. Stern, 2009, Phys. Rev. Lett. **103**, 196803.

Li, H. D., Z. Y. Wang, X. Kan, X. Guo, H. T. He, Z. Wang, J. N. Wang, T. L. Wong, N. Wang, and M. H. Xie, 2010, New J. Phys. **12**, 103038.
Li, J., R.-L. Chu, J. K. Jain, and S.-Q. Shen, 2009, Phys. Rev. Lett. **102**, 136806.
Li, R., J. Wang, X. L. Qi, and S. C. Zhang, 2010, Nature Phys. **6**, 284.
Li, Y.-Y., *et al.*, 2010, Adv. Mater. **22**, 4002.
Lin, H., R. S. Markiewicz, L. A. Wray, L. Fu, M. Z. Hasan, and A. Bansil, 2010, arXiv:1003.2615.
Lin, H., L. A. Wray, Y. Xia, S. Xu, S. Jia, R. J. Cava, A. Bansil, and M. Z. Hasan, 2010, Nature Mater. **9**, 546.
Linder, J., and A. Sudbo, 2010, Phys. Rev. B **82**, 041409(R).
Linder, J., Y. Tanaka, T. Yokoyama, A. Sudbo, and N. Nagaosa, 2010a, Phys. Rev. Lett. **104**, 067001.
Linder, J., Y. Tanaka, T. Yokoyama, A. Sudbø, and N. Nagaosa, 2010b, Phys. Rev. B **81**, 184525.
Linder, J., T. Yokoyama, and A. Sudbø, 2009, Phys. Rev. B **80**, 205401.
Liu, C.-X., T. L. Hughes, X.-L. Qi, K. Wang, and S.-C. Zhang, 2008, Phys. Rev. Lett. **100**, 236601.
Liu, C.-X., X.-L. Qi, X. Dai, Z. Fang, and S.-C. Zhang, 2008, Phys. Rev. Lett. **101**, 146802.
Liu, C.-X., X.-L. Qi, H. Zhang, X. Dai, Z. Fang, and S.-C. Zhang, 2010, Phys. Rev. B **82**, 045122.
Liu, C.-X., H. Zhang, B. Yan, X.-L. Qi, T. Frauenheim, X. Dai, Z. Fang, and S.-C. Zhang, 2010, Phys. Rev. B **81**, 041307.
Liu, Q., C.-X. Liu, C. Xu, X.-L. Qi, and S.-C. Zhang, 2009, Phys. Rev. Lett. **102**, 156603.
Loring, T. A., and M. B. Hastings, 2010, Europhys. Lett. **92**, 67004.
Lu, H. Z., W. Y. Shan, W. Yao, Q. Niu, and S. Q. Shen, 2010, Phys. Rev. B **81**, 115407.
Lutchyn, R. M., J. D. Sau, and S. Das Sarma, 2010, Phys. Rev. Lett. **105**, 077001.
Lutchyn, R. M., T. Stanescu, and S. D. Sarma, 2011, Phys. Rev. Lett. **106**, 127001.
Maciejko, J., C.-X. Liu, Y. Oreg, X. L. Qi, C. Wu, and S. C. Zhang, 2009, Phys. Rev. Lett. **102**, 256803.
Maciejko, J., X.-L. Qi, H. D. Drew, and S.-C. Zhang, 2010, Phys. Rev. Lett. **105**, 166803.
Maciejko, J., X. L. Qi, A. Karch, and S. C. Zhang, 2010, Phys. Rev. Lett. **105**, 246809.
Maciejko, J., X.-L. Qi, and S.-C. Zhang, 2010, Phys. Rev. B **82**, 155310.
Mackenzie, A. P., and Y. Maeno, 2003, Rev. Mod. Phys. **75**, 657.
Malashevich, A., I. Souza, S. Coh, and D. Vanderbilt, 2010, New J. Phys. **12**, 053032.
Mao, L., J. Shi, Q. Niu, and C. Zhang, 2011, Phys. Rev. Lett. **106**, 157003.
Meidan, D., and Y. Oreg, 2005, Phys. Rev. B **72**, 121312(R).
Mills, D. L., and E. Burstein, 1974, Rep. Prog. Phys. **37**, 817.
Min, H., J. Hill, N. Sinitsyn, B. Sahu, L. Kleinman, and A. MacDonald, 2006, Phys. Rev. B **74**, 165310.
Mondal, S., D. Sen, K. Sengupta, and R. Shankar, 2010a, Phys. Rev. B **82**, 045120.
Mondal, S., D. Sen, K. Sengupta, and R. Shankar, 2010b, Phys. Rev. Lett. **104**, 046403.
Moore, J. E., 2010, Nature (London) **464**, 194.
Moore, J. E., and L. Balents, 2007, Phys. Rev. B **75**, 121306.
Murakami, S., 2006, Phys. Rev. Lett. **97**, 236805.
Murakami, S., S. Iso, Y. Avishai, M. Onoda, and N. Nagaosa, 2007, Phys. Rev. B **76**, 205304.
Murakami, S., N. Nagaosa, and S. C. Zhang, 2003, Science **301**, 1348.
Murakami, S., N. Nagaosa, and S. C. Zhang, 2004, Phys. Rev. Lett. **93**, 156804.
Nakahara, M., 1990, *Geometry, Topology, and Physics* (A. Hilger, London).
Nayak, C., S. H. Simon, A. Stern, M. Freedman, and S. D. Sarma, 2008, Rev. Mod. Phys. **80**, 1083.
Nielsen, H. B., and M. Ninomiya, 1981, Nucl. Phys. **B185**, 20.
Niemi, A. J., and G. W. Semenoff, 1983, Phys. Rev. Lett. **51**, 2077.
Nishide, A., Y. Takeichi, T. Okuda, A. A. Taskin, T. Hirahara, K. Nakatsuji, F. Komori, A. Kakizaki, Y. Ando, and I. Matsuda, 2010, New J. Phys. **12**, 065011.
Nomura, K., M. Koshino, and S. Ryu, 2007, Phys. Rev. Lett. **99**, 146806.
Nomura, K., and N. Nagaosa, 2010, Phys. Rev. B **82**, 161401(R).
Nomura, K., S. Ryu, M. Koshino, C. Mudry, and A. Furusaki, 2008, Phys. Rev. Lett. **100**, 246806.
Novik, E. G., A. Pfeuffer-Jeschke, T. Jungwirth, V. Latussek, C. R. Becker, G. Landwehr, H. Buhmann, and L. W. Molenkamp, 2005, Phys. Rev. B **72**, 035321.
Novik, E. G., P. Recher, E. M. Hankiewicz, and B. Trauzettel, 2010, Phys. Rev. B **81**, 241303.
Obuse, H., A. Furusaki, S. Ryu, and C. Mudry, 2007, Phys. Rev. B **76**, 075301.
Obuse, H., A. Furusaki, S. Ryu, and C. Mudry, 2008, Phys. Rev. B **78**, 115301.
Olshanetsky, E., Z. Kvon, G. Gusev, N. Mikhailov, S. Dvoretsky, and J. Portal, 2010, JETP Lett. **91**, 347.
Oreg, Y., G. Refael, and F. von Oppen, 2010, Phys. Rev. Lett. **105**, 177002.
Ostrovsky, P. M., I. V. Gornyi, and A. D. Mirlin, 2010, Phys. Rev. Lett. **105**, 036803.
Pankratov, O. A., 1990, Semicond. Sci. Technol. **5**, S204.
Pankratov, O. A., S. V. Pakhomov, and B. A. Volkov, 1987, Solid State Commun. **61**, 93.
Peccei, R. D., and H. R. Quinn, 1977, Phys. Rev. Lett. **38**, 1440.
Peng, H., K. Lai, D. Kong, S. Meister, Y. Chen, X. L. Qi, S. C. Zhang, Z. X. Shen, and Y. Cui, 2010, Nature Mater. **9**, 225.
Pesin, D. A., and L. Balents, 2010, Nature Phys. **6**, 376.
Potter, A. C., and P. A. Lee, 2010, Phys. Rev. Lett. **105**, 227003.
Prodan, E., 2009, Phys. Rev. B **80**, 125327.
Qi, X.-L., T. L. Hughes, S. Raghu, and S.-C. Zhang, 2009a, Phys. Rev. Lett. **102**, 187001.
Qi, X.-L., T. Hughes, and S.-C. Zhang, 2008a, Nature Phys. **4**, 273.
Qi, X.-L., T. Hughes, and S.-C. Zhang, 2008b, Phys. Rev. B **78**, 195424.
Qi, X.-L., T. L. Hughes, and S.-C. Zhang, 2010a, Phys. Rev. B **82**, 184516.
Qi, X.-L., T. L. Hughes, and S.-C. Zhang, 2010b, Phys. Rev. B **81**, 134508.
Qi, X.-L., R. Li, J. Zang, and S.-C. Zhang, 2009, Science **323**, 1184.
Qi, X. L., Y. S. Wu, and S. C. Zhang, 2006, Phys. Rev. B **74**, 085308.
Qi, X.-L., and S.-C. Zhang, 2008, Phys. Rev. Lett. **101**, 086802.
Qi, X. L., and S. C. Zhang, 2010, Phys. Today **63**, 33.
Rachel, S., and K. L. Hur, 2010, Phys. Rev. B **82**, 075106.
Raghu, S., S. B. Chung, X. L. Qi, and S. C. Zhang, 2010, Phys. Rev. Lett. **104**, 116401.
Raghu, S., X.-L. Qi, C. Honerkamp, and S.-C. Zhang, 2008, Phys. Rev. Lett. **100**, 156401.
Ran, Y., A. Vishwanath, and D.-H. Lee, 2008, Phys. Rev. Lett. **101**, 086801.
Ran, Y., Y. Zhang, and A. Vishwanath, 2009, Nature Phys. **5**, 298.
Read, N., and D. Green, 2000, Phys. Rev. B **61**, 10 267.
Redlich, A. N., 1984a, Phys. Rev. Lett. **52**, 18.
Redlich, A. N., 1984b, Phys. Rev. D **29**, 2366.

Resta, R., 1994, Rev. Mod. Phys. **66**, 899.
Rosenberg, G., and M. Franz, 2010, Phys. Rev. B **82**, 035105.
Rosenberg, G., H. M. Guo, and M. Franz, 2010, Phys. Rev. B **82**, 041104.
Roth, A., C. Brüne, H. Buhmann, L. W. Molenkamp, J. Maciejko, X.-L. Qi, and S.-C. Zhang, 2009, Science **325**, 294.
Rothe, D. G., R. W. Reinthaler, C.-X. Liu, L. W. Molenkamp, S. C. Zhang, and E. M. Hankiewicz, 2010, New J. Phys. **12**, 065012.
Roushan, P., J. Seo, C. V. Parker, Y. S. Hor, D. Hsieh, D. Qian, A. Richardella, M. Z. Hasan, R. J. Cava, and A. Yazdani, 2009, Nature (London) **460**, 1106.
Roy, R., 2008, arXiv:0803.2868.
Roy, R., 2009a, Phys. Rev. B **79**, 195322.
Roy, R., 2009b, Phys. Rev. B **79**, 195321.
Ryu, S., C. Mudry, H. Obuse, and A. Furusaki, 2007, Phys. Rev. Lett. **99**, 116601.
Ryu, S., C. Mudry, H. Obuse, and A. Furusaki, 2010, New J. Phys. **12**, 065005.
Ryu, S., A. P. Schnyder, A. Furusaki, and A. W. W. Ludwig, 2010, New J. Phys. **12**, 065010.
Sakamoto, Y., T. Hirahara, H. Miyazaki, S.-I. Kimura, and S. Hasegawa, 2010, Phys. Rev. B **81**, 165432.
Santos, L., T. Neupert, C. Chamon, and C. Mudry, 2010, Phys. Rev. B **81**, 184502.
Sato, K., D. Loss, and Y. Tserkovnyak, 2010, Phys. Rev. Lett. **105**, 226401.
Sato, M., 2009, Phys. Rev. B **79**, 214526.
Sato, M., 2010, Phys. Rev. B **81**, 220504(R).
Sato, M., and S. Fujimoto, 2009, Phys. Rev. B **79**, 094504.
Sato, M., and S. Fujimoto, 2010, Phys. Rev. Lett. **105**, 217001.
Sato, M., Y. Takahashi, and S. Fujimoto, 2009, Phys. Rev. Lett. **103**, 020401.
Sato, M., Y. Takahashi, and S. Fujimoto, 2010, Phys. Rev. B **82**, 134521.
Sato, T., K. Segawa, H. Guo, K. Sugawara, S. Souma, T. Takahashi, and Y. Ando, 2010, Phys. Rev. Lett. **105**, 136802.
Sau, J. D., R. M. Lutchyn, S. Tewari, and S. Das Sarma, 2010, Phys. Rev. Lett. **104**, 040502.
Schmidt, M. J., E. G. Novik, M. Kindermann, and B. Trauzettel, 2009, Phys. Rev. B **79**, 241306.
Schnyder, A. P., S. Ryu, A. Furusaki, and A. W. W. Ludwig, 2008, Phys. Rev. B **78**, 195125.
Semenoff, G. W., 1984, Phys. Rev. Lett. **53**, 2449.
Seo, J., P. Roushan, H. Beidenkopf, Y. S. Hor, R. J. Cava, and A. Yazdani, 2010, Nature (London) **466**, 343.
Seradjeh, B., J. E. Moore, and M. Franz, 2009, Phys. Rev. Lett. **103**, 066402.
Shahil, K. M. F., M. Z. Hossain, D. Teweldebrhan, and A. A. Balandin, 2010, Appl. Phys. Lett. **96**, 153103.
Shan, W.-Y., H.-Z. Lu, and S.-Q. Shen, 2010, New J. Phys. **12**, 043048.
Sheng, D. N., Z. Y. Weng, L. Sheng, and F. D. M. Haldane, 2006, Phys. Rev. Lett. **97**, 036808.
Shindou, R., A. Furusaki, and N. Nagaosa, 2010, Phys. Rev. B **82**, 180505.
Shindou, R., and S. Murakami, 2009, Phys. Rev. B **79**, 045321.
Shitade, A., H. Katsura, J. Kuneš, X.-L. Qi, S.-C. Zhang, and N. Nagaosa, 2009, Phys. Rev. Lett. **102**, 256403.
Sinova, J., D. Culcer, Q. Niu, N. A. Sinitsyn, T. Jungwirth, and A. H. MacDonald, 2004, Phys. Rev. Lett. **92**, 126603.
Stanescu, T. D., V. Galitski, and S. Das Sarma, 2010, Phys. Rev. A **82**, 013608.
Steinberg, H., D. R. Gardner, Y. S. Lee, and P. Jarillo-Herrero, 2010, Nano Lett. **10**, 5032.
Stone, M., C.-K. Chiu, and A. Roy, 2011, J. Phys. A **44**, 045001.
Ström, A., and H. Johannesson, 2009, Phys. Rev. Lett. **102**, 096806.
Ström, A., H. Johannesson, and G. I. Japaridze, 2010, Phys. Rev. Lett. **104**, 256804.
Su, W. P., J. R. Schrieffer, and A. J. Heeger, 1979, Phys. Rev. Lett. **42**, 1698.
Sushkov, A. B., G. S. Jenkins, D. C. Schmadel, N. P. Butch, J. Paglione, and H. D. Drew, 2010, Phys. Rev. B **82**, 125110.
Swingle, B., M. Barkeshli, J. McGreevy, and T. Senthil, 2010, arXiv:1005.1076.
Tanaka, Y., and N. Nagaosa, 2009, Phys. Rev. Lett. **103**, 166403.
Tanaka, Y., T. Yokoyama, and N. Nagaosa, 2009, Phys. Rev. Lett. **103**, 107002.
Tang, H., D. Liang, R. L. J. Qiu, and X. P. A. Gao, 2010, arXiv:1003.6099.
Taskin, A. A., and Y. Ando, 2009, Phys. Rev. B **80**, 085303.
Teo, J. C., and C. Kane, 2010, Phys. Rev. B **82**, 115120.
Teo, J. C. Y., L. Fu, and C. L. Kane, 2008, Phys. Rev. B **78**, 045426.
Teo, J. C. Y., and C. L. Kane, 2009, Phys. Rev. B **79**, 235321.
Teweldebrhan, D., V. Goyal, and A. A. Balandin, 2010a, Nano Lett. **10**, 1209.
Teweldebrhan, D., V. Goyal, M. Rahman, and A. A. Balandin, 2010b, Appl. Phys. Lett. **96**, 053107.
Thouless, D. J., 1983, Phys. Rev. B **27**, 6083.
Thouless, D. J., 1998, *Topological Quantum Numbers in Nonrelativistic Physics* (World Scientific, Singapore).
Thouless, D. J., M. Kohmoto, M. P. Nightingale, and M. den Nijs, 1982, Phys. Rev. Lett. **49**, 405.
Tkachov, G., and E. M. Hankiewicz, 2010, Phys. Rev. Lett. **104**, 166803.
Tran, M.-T., and K.-S. Kim, 2010, Phys. Rev. B **82**, 155142.
Volkov, B. A., and O. A. Pankratov, 1985, JETP Lett. **42**, 178.
Vollhardt, D., and P. Wölfle, 1990, *The Superfluid Phases of Helium 3* (Taylor & Francis, London).
Volovik, G. E., 1988a, Phys. Lett. **128A**, 277.
Volovik, G. E., 1988b, Zh. Eksp. Teor. Fiz. **94**, 123 [Sov. Phys. JETP **67**, 1804 (1988b)].
Volovik, G. E., 1999, Pis'ma Zh. Eksp. Teor. Fiz. **70**, 601 [JETP Lett. **70**, 609 (1999)].
Volovik, G. E., 2002, JETP Lett. **75**, 63.
Volovik, G. E., 2003, *The Universe in a Helium Droplet* (Oxford University Press, Oxford).
von Klitzing, K., G. Dorda, and M. Pepper, 1980, Phys. Rev. Lett. **45**, 494.
Wan, X., A. Turner, A. Vishwanath, and S. Y. Savrasov, 2011, Phys. Rev. B **83**, 205101.
Wang, Z., T. Lin, P. Wei, X. Liu, R. Dumas, K. Liu, and J. Shi, 2010, Appl. Phys. Lett. **97**, 042112.
Wang, Z., X.-L. Qi, and S.-C. Zhang, 2010a, New J. Phys. **12**, 065007.
Wang, Z., X.-L. Qi, and S.-C. Zhang, 2010b, Phys. Rev. Lett. **105**, 256803.
Wang-Kong Tse, A. H. M., 2010, Phys. Rev. Lett. **105**, 057401.
Weeks, C., and M. Franz, 2010, Phys. Rev. B **81**, 085105.
Werner, P., 2000, Diplom thesis (ETH Zurich).
Wilczek, F., 1987, Phys. Rev. Lett. **58**, 1799.
Wilczek, F., 2009, Nature (London) **458**, 129.
Wimmer, M., A. R. Akhmerov, M. V. Medvedyeva, J. Tworzydło, and C. W. J. Beenakker, 2010, Phys. Rev. Lett. **105**, 046803.
Winkler, R., 2003, *Spin-Orbit Coupling Effects in Two-Dimensional Electron and Hole Systems* (Springer, New York).
Wittel, K., and R. Manne, 1974, Theor. Chim. Acta **33**, 347.
Witten, E., 1979, Phys. Lett. **86B**, 283.
Witten, E., 1983, Nucl. Phys. **B223**, 422.

Wray, L. A., S.-Y. Xu, Y. Xia, Y. S. Hor, D. Qian, A. V. Fedorov, H. Lin, A. Bansil, R. J. Cava, and M. Z. Hasan, 2010, Nature Phys. **6**, 855.
Wu, C., 2008, Phys. Rev. Lett. **101**, 186807.
Wu, C., B. A. Bernevig, and S. C. Zhang, 2006, Phys. Rev. Lett. **96**, 106401.
Wu, C., K. Sun, E. Fradkin, and S.-C. Zhang, 2007, Phys. Rev. B **75**, 115103.
Wu, C., and S.-C. Zhang, 2004, Phys. Rev. Lett. **93**, 036403.
Xia, Y., *et al.*, 2008, arXiv:0812.2078.
Xia, Y., *et al.*, 2009, Nature Phys. **5**, 398.
Xu, C., and J. Moore, 2006, Phys. Rev. B **73**, 045322.
Yan, B., C.-X. Liu, H. Zhang, C. Y. Yam, X. L. Qi, T. Frauenheim, and S. C. Zhang, 2010, Europhys. Lett. **90**, 37002.
Yang, B.-J., and Y. B. Kim, 2010, Phys. Rev. B **82**, 085111.
Yao, Y., F. Ye, X.-L. Qi, S.-C. Zhang, and Z. Fang, 2007, Phys. Rev. B **75**, 041401(R).
Yazyev, O. V., J. E. Moore, and S. G. Louie, 2010, Phys. Rev. Lett. **105**, 266806.
Ye, F., G. H. Ding, H. Zhai, and Z. B. Su, 2010, Europhys. Lett. **90**, 47 001.
Yokoyama, T., Y. Tanaka, and N. Nagaosa, 2009, Phys. Rev. Lett. **102**, 166801.
Yokoyama, T., Y. Tanaka, and N. Nagaosa, 2010, Phys. Rev. B **81**, 121401.
Yokoyama, T., J. Zang, and N. Nagaosa, 2010, Phys. Rev. B **81**, 241410.
Young, M. W., S. S. Lee, and C. Kallin, 2008, Phys. Rev. B **78**, 125316.
Yu, R., W. Zhang, H. J. Zhang, S. C. Zhang, X. Dai, and Z. Fang, 2010, Science **329**, 61.
Zak, J., 1989, Phys. Rev. Lett. **62**, 2747.
Zang, J., and N. Nagaosa, 2010, Phys. Rev. B **81**, 245125.
Zhang, C., S. Tewari, R. M. Lutchyn, and S. Das Sarma, 2008, Phys. Rev. Lett. **101**, 160401.
Zhang, G., H. Qin, J. Teng, J. Guo, Q. Guo, X. Dai, Z. Fang, and K. Wu, 2009, Appl. Phys. Lett. **95**, 053114.
Zhang, H., C.-X. Liu, X.-L. Qi, X. Dai, Z. Fang, and S.-C. Zhang, 2009, Nature Phys. **5**, 438.
Zhang, H., C.-X. Liu, X.-L. Qi, X.-Y. Deng, X. Dai, S.-C. Zhang, and Z. Fang, 2009, Phys. Rev. B **80**, 085307.
Zhang, L. B., K. Chang, X. C. Xie, H. Buhmann, and L. W. Molenkamp, 2010, New J. Phys. **12**, 083058.
Zhang, S. C., 1992, Int. J. Mod. Phys. B **6**, 25.
Zhang, S. C., 2008, Physics **1**, 6.
Zhang, S. C., and J. P. Hu, 2001, Science **294**, 823.
Zhang, T., *et al.*, 2009, Phys. Rev. Lett. **103**, 266803.
Zhang, W., R. Yu, H. Zhang, X. Dai, and Z. Fang, 2010, New J. Phys. **12**, 065013.
Zhang, Y., Y. Ran, and A. Vishwanath, 2009, Phys. Rev. B **79**, 245331.
Zhang, Y., and A. Vishwanath, 2010, Phys. Rev. Lett. **105**, 206601.
Zhang, Y., *et al.*, 2010, Nature Phys. **6**, 584.
Zhou, B., H.-Z. Lu, R.-L. Chu, S.-Q. Shen, and Q. Niu, 2008, Phys. Rev. Lett. **101**, 246807.
Zhou, X., C. Fang, W.-F. Tsai, and J. Hu, 2009, Phys. Rev. B **80**, 245317.
Zhu, S. L., H. Fu, C. J. Wu, S. C. Zhang, and L. M. Duan, 2006, Phys. Rev. Lett. **97**, 240401.
Žitko, R., 2010, Phys. Rev. B **81**, 241414.
Zyuzin, V. A., and G. A. Fiete, 2010, Phys. Rev. B **82**, 113305.